WL-TR-97-3019

Development of Preliminary Design Models for Active Aeroelastic Wing Application

Frank Eastep

CSA ENGINEERING
2850 W. BAYSHORE ROAD
PALO ALTO CA 94303-3843

January 1997

FINAL REPORT FOR PERIOD October 1994 - December 1996

Approved for public release; distribution is unlimited.

FLIGHT DYNAMICS DIRECTORATE
WRIGHT LABORATORY
AIR FORCE MATERIEL COMMAND
WRIGHT PATTERSON AFB OH 45433-7542

NOTICE

USING GOVERNMENT DRAWINGS, SPECIFICATIONS, OR OTHER DATA INCLUDED IN THIS DOCUMENT FOR ANY PURPOSE OTHER THAN GOVERNMENT PROCUREMENT DOES NOT IN ANY WAY OBLIGATE THE US GOVERNMENT. THE FACT THAT THE GOVERNMENT FORMULATED OR SUPPLIED THE DRAWINGS, SPECIFICATIONS, OR OTHER DATA DOES NOT LICENSE THE HOLDER OR ANY OTHER PERSON OR CORPORATION; OR CONVEY ANY RIGHTS OR PERMISSION TO MANUFACTURE, USE, OR SELL ANY PATENTED INVENTION THAT MAY RELATE TO THEM.

THIS REPORT IS RELEASABLE TO THE NATIONAL TECHNICAL INFORMATION SERVICE (NTIS). AT NTIS, IT WILL BE AVAILABLE TO THE GENERAL PUBLIC, INCLUDING FOREIGN NATIONS.

THIS TECHNICAL REPORT HAS BEEN REVIEWED AND IS APPROVED FOR PUBLICATION.

BILL LAU, Capt, USAF
Project Engineer
Design & Analysis Branch

NELSON D. WOLF
Acting Chief
Design & Analysis Branch

JAMES L. RUDD
Chief
Structures Division

IF YOUR ADDRESS HAS CHANGED, IF YOU WISH TO BE REMOVED FROM OUR MAILING LIST, OR IF THE ADDRESSEE IS NO LONGER EMPLOYED BY YOUR ORGANIZATION PLEASE NOTIFY WL/FIBD WRIGHT-PATTERSON AFB OH 45433-7542 TO HELP MAINTAIN A CURRENT MAILING LIST.

Do not return copies of this report unless contractual obligations or notice on a specific document requires its return.

REPORT DOCUMENTATION PAGE

Form Approved
OMB No. 0704-0188

1. AGENCY USE ONLY *(Leave blank)*	2. REPORT DATE	3. REPORT TYPE AND DATES COVERED
	January 1997	Final Report 10/31/94--12/31/96

4. TITLE AND SUBTITLE
Development of Preliminary Design Models for Active Aeroelastic Wing Application

5. FUNDING NUMBERS
C F33615-94-C-3200
PE 62201
PR 2401
TA 02
WU 99

6. AUTHOR(S)
Frank Eastep

7. PERFORMING ORGANIZATION NAME(S) AND ADDRESS(ES)
CSA ENGINEERING
2850 W BAYSHORE RD
PALO ALTO CA 94303-3843

8. PERFORMING ORGANIZATION REPORT NUMBER

9. SPONSORING/MONITORING AGENCY NAME(S) AND ADDRESS(ES)
FLIGHT DYNAMICS DIRECTORATE
WRIGHT LABORATORY
AIR FORCE MATERIEL COMMAND
WRIGHT-PATTERSON AFB OH 45433-7542
POC: CPT BILL LAU, WL/FIBD, 937-255-7191

10. SPONSORING/MONITORING AGENCY REPORT NUMBER
WL-TR-97-3019

11. SUPPLEMENTARY NOTES

12a. DISTRIBUTION/AVAILABILITY STATEMENT
APPROVED FOR PUBLIC RELEASE: DISTRIBUTION IS UNLIMITED

12b. DISTRIBUTION CODE

13. ABSTRACT *(Maximum 200 words)*
An investigation of active aeroelastic wing (AAW) technology was initially conducted on a "beam rod" model of an F/A-18 aircraft for demonstration of an acceptable roll performance. The beam rod model was verified by comparing the natural frequencies to the results obtained by McDonnell-Douglas during a ground vibration test. Further verification of the beam-rod model and selected aerodynamic representation of the F/A-18 were obtained in flutter studies. The beam-rod model was further developed for active aeroelastic wing technology through a study of control surface blending for the roll performance enhancement of the F/A-18 with a reduction of wing stiffening. It is demonstrated that the roll performance of the F/A-18 could be enhanced by incorporating AAW concepts in the design stage of aircraft development. It was determined that a finite-element representation of the built-up wing was necessary for the accurate prediction of aeroelastic deformation. A generic built-up fighter wing was considered to demonstrate preliminary design methods incorporating aeroelastic wing technology. Optimization studies of this aircraft wing were conducted utilizing multiple blended control surfaces to effect roll trim. The results demonstrate that active aeroelastic wing technology is a viable design methodology when compared to the traditional design methodology of increasing stiffness to avoid problems associated with aeroelastic deformation. The incorporation of AAW technology in the preliminary design stage produces substantial structural weight savings.

14. SUBJECT TERMS	15. NUMBER OF PAGES
Active Aeroelastic Wing, Preliminary Design, Optimization, Finite Element Models, F/A-18	135
	16. PRICE CODE

17. SECURITY CLASSIFICATION OF REPORT	18. SECURITY CLASSIFICATION OF THIS PAGE	19. SECURITY CLASSIFICATION OF ABSTRACT	20. LIMITATION OF ABSTRACT
Unclassified	Unclassified	Unclassified	SAR

Table of Contents

Section		Page
I	Introduction	1
II	Documentation of F/A-18 Aircraft	4
III	Beam/Rod Model	6
IV	Dynamic Analysis	9
	Beam/Rod Model Dynamic Analysis	9
V	Dynamic Aeroelastic Analysis	38
	p-k Flutter Solution	38
	Beam/Rod Model Flutter Analysis	39
VI	Control Surface Blending for Roll Performance Enhancement	70
	Analytical Tools	70
	Theoretical Background	71
	Example: Fighter Aircraft	74
VII	F/A-18 A Built-up Finite Elment Model	80
VIII	Optimization of a Generic Fighter Wing Incorporating Active Aeroelastic Wing Technology	103
	Introduction	103
	Analytical Tools	103
	Theoretical Background	104
	Example: Generic Fighter Aircraft Wing	108
IX	Conclusions and Recommendations	120
References		122

List of Tables

Table	Title	Page
1	Eigen Analysis of F/A-18 Aircraft with a Tip Missile for Symmetric Boundary Conditions	11
2	Eigen Analysis of F/A-18 Aircraft with a Tip Missile for Anti-Symmetric Boundary Conditions	12
3	Eigen Analysis of F/A-18 Aircraft without a Tip Missile for Symmetric Boundary Conditions	13
4	Eigen Analysis of F/A-18 Aircraft without a Tip Missile for Anti-Symmetric Boundary Conditions	14
5	Eigen Analysis of F/A-18 Aircraft without a Missile Launcher for Symmetric Boundary Conditons	15
6	Eigen Analysis of F/A-18 Aircraft without a Missile Launcher for Anti-Symmetric Boundary Conditions	16
7	Comparison of Theoretical and Experimental Results for the F/A-18 Aircraft with a Tip Missile for Symmetric Boundary Conditions	17
8	Comparison of Theoretical and Experimental Results for the F/A-18 Aircraft with a Tip Missile for Anti-Symmetric Boundary Conditions	18
9	Comparison of Theoretical and Experimental Results for the F/A-18 Aircraft without a Tip Missile for Symmetric Boundary Conditions	18
10	Comparison of Theoretical and Experimental Results for the F/A-18 Aircraft without a Tip Missile for Anti-Symmetric Boundary Conditions	18
11	Comparison of Natural Frequencies for the Beam-Rod Model of F/A-18	82
12	Wing Sectional Mass Properties	90
13	Comparison of Beam/Rod and Built-Up Model Natural Frequencies	91
14	Comparison of Category I Optimization Results	113
15	Comparison of Constraints for Nominal and Final Wing Configurations	119

List of Figures

Figure	Title	Page
1	Assembly Drawing of F/A-18 Wing with Detailed Wing Box Structural Elements, Control Surfaces and Tip Missile Launcher	3
2	Diagram of Fighter Aircraft Finite Element and Aerodynamic Model	6
3	Missile Launcher Structural Finite Element Model of the F/A-18 Aircraft	10
4	Mode Shapes and Frequencies of the F/A-18 Aircraft with a Tip Missile for Symmetric Boundary Conditions	20
5	Mode Shapes and Frequencies of F/A-18 Aircraft with a Tip Missile for Anti-Symmetric Boundary Conditions	23
6	Mode Shapes and Frequencies of F/A-18 Aircraft without a Tip Missile for Symmetric Boundary Conditions	26
7	Mode Shapes and Frequencies of F/A-18 Aircraft without a Tip Missile for Anti-Symmetric Mode Shapes	29
8	Mode Shapes and Frequencies of F/A-18 Aircraft without a Missile Launcher for Symmetric Mode Shapes	32
9	Mode Shapes and Frequencies of F/A-18 Aircraft without a Missile Launcher for Anti-Symmetric Mode Shapes	35
10	Aerodynamic Panel Representation for Wing and Launcher	40
11	Division of Aerodynamic Panels for the Wing, Leading Edge In-board and Out-board Flap, Trailing Edge Out-board Flap, Aileron and Missile Launcher	41
12	Splined Aerodynamic Mode Shapes and Frequencies of the F/A-18 Wing with a Tip Missile for Symmetric Boundary Conditions	42
13	Splined Aerodynamic Mode Shapes and Frequencies of F/A-18 Aircraft without a Tip Missile for Symmetric Boundary Conditions	44
14	V-g-w Plot of F/A-18 Aircraft with a Tip Missile for Symmetric Boundary Conditions, Mach 0.7, Alt = Sea Level	46

List of Figures (Cont'd)

Figure	Title	Page
15	V-g-w Plot of F/A-18 Aircraft with a Tip Missile for Symmetric Boundary Conditions, Mach 0.75, Alt = Sea Level	47
16	V-g-w Plot of F/A-18 Aircraft with a Tip Missile for Symmetric Boundary Conditions, Mach 0.8, Alt = Sea Level	48
17	V-g-w Plot of F/A-18 Aircraft with a Tip Missile for Symmetric Boundary Conditions, Mach 0.85, Alt = Sea Level	49
18	V-g-w Plot of F/A-18 Aircraft with a Tip Missile for Symmetric Boundary Conditions, Mach 0.9, Alt = Sea Level	50
19	V-g-w Plot of F/A-18 Aircraft with a Tip Missile for Symmetric Boundary Conditions, Mach 0.9, Alt = -10K ft.	51
20	V-g-w Plot of F/A-18 Aircraft with a Tip Missile for Symmetric Boundary Conditions, Mach 0.9, Alt = -20K ft.	52
21	V-g-w Plot of F/A-18 Aircraft with a Tip Missile for Symmetric Boundary Conditions, Mach 0.95, Alt = Sea Level	53
22	V-g-w Plot of F/A-18 Aircraft with a Tip Missile for Symmetric Boundary Conditions, Mach 1.1, Alt = Sea Level	54
23	V-g-w Plot of F/A-18 Aircraft with a Tip Missile for Symmetric Boundary Conditions, Mach 1.15, Alt = Sea Level	55
24	V-g-w Plot of F/A-18 Aircraft with a Tip Missile for Symmetric Boundary Conditions, Mach 1.2, Alt = Sea Level	56
25	V-g-w Plot of F/A-18 Aircraft with a Tip Missile for Symmetric Boundary Conditions, Mach 1.25, Alt = Sea Level	57
26	V-g-w Plot of F/A-18 Aircraft without a Tip Missile for Symmetric Boundary Conditions, Mach 0.7	58
27	V-g-w Plot of F/A-18 Aircraft without a Tip Missile for Symmetric Boundary Conditions, Mach 0.75	59

List of Figures (Cont'd)

Figure	Title	Page
28	V-g-w Plot of F/A-18 Aircraft without a Tip Missile for Symmetric Boundary Conditions, Mach 0.8	60
29	V-g-w Plot of F/A-18 Aircraft without a Tip Missile for Symmetric Boundary Conditions, Mach 0.85, Alt = Sea Level	61
30	V-g-w Plot of F/A-18 Aircraft without a Tip Missile for Symmetric Boundary Conditions, Mach 0.9, Alt = Sea Level	62
31	V-g-w Plot of F/A-18 Aircraft without a Tip Missile for Symmetric Boundary Conditions, Mach 0.9, Alt = -10K ft.	63
32	V-g-w Plot of F/A-18 Aircraft without a Tip Missile for Symmetric Boundary Conditions, Mach 0.9, Alt = -20K ft.	64
33	V-g-w Plot of F/A-18 Aircraft without a Tip Missile for Symmetric Boundary Conditions, Mach 0.95	65
34	V-g-w Plot of F/A-18 Aircraft without a Tip Missile for Symmetric Boundary Conditions, Mach 1.1, Alt = Sea Level	66
35	V-g-w Plot of F/A-18 Aircraft without a Tip Missile for Symmetric Boundary Conditions, Mach 1.15, Alt = Sea Level	67
36	V-g-w Plot of F/A-18 Aircraft without a Tip Missile for Symmetric Boundary Conditions, Mach 1.2, Alt = Sea Level	68
37	V-g-w Plot of F/A-18 Aircraft without a Tip Missile for Symmetric Boundary Conditions, Mach 1.25, Alt = Sea Level	69
38	Comparison of Flexible and Rigid Roll Rates for Trim, Given Aileron Deflection	73
39	Comparison of Flexible and Rigid Aileron Deflections for Trim, Given Constant Roll Rate	73
40	Diagram of Fighter Aircraft Finite Element and Aerodynamic Model	74
41	Control Surface Effectiveness for Fighter Aircraft Wing, Mach 0.9	75

List of Figures (Cont'd)

Figure	Title	Page
42	Roll Trim for Fighter Aircraft Wing, 90 deg/sec Roll Rate, Mach 0.9	76
43	Control Surface Effectiveness for Reduced Stiffness Fighter Aircraft Wing, Mach 0.9	77
44	Roll Trim for Reduced Stiffness Fighter Aircraft Wing, 90 deg/sec Roll Rate, Mach 0.9	77
45	Control Surface Effectiveness for Reduced Stiffness Fighter Aircraft Wing, Mach 1.2	78
46	Roll Trim for Reduced Stiffness Fighter Aircraft Wing, 90 deg/sec Roll Rate, Mach 1.2	79
47	Initial Finite Element Model F/A-18	81
48	Mode 1	83
49	Mode 2	83
50	Mode 3	84
51	Mode 4	84
52	Mode 5	85
53	Mode 6	85
54	S/A-18 Finite Element Model	87
55	McDonnell Douglas Finite Element Model of F/A-18	89
56	F/A-18 Wing	92
57	Mode 1: Wing First Bending	93
58	Mode 2: Wing First Torsion	94
59	Mode 3: Wing Second Bending	95

List of Figures (Cont'd)

Figure	Title	Page
60	Mode 4: Launcher Lateral	96
61	Mode 5: Trailing Edge Flap Rotation	97
62	Mode 6: Aileron Rotation	98
63	Mode 7: Wing Fore/Aft Bending	99
64	Mode 8: Tip Missile Bending	100
65	Mode 9: Leading Edge Flap Rotation	101
66	Mode 10: Trailing Edge Flap Bending	102
67	Comparison of Flexible and Rigid Roll Rates for Trim, Given Aileron Deflection	107
68	Comparison of Flexible and Rigid Aileron Deflections for Trim, Given Constant Roll Rate	107
69	Finite Element Model of the Generic Fighter Aircraft Wing	109
70	Diagram of Generic Fighter Wing Structural and Aerodynamic Model	109
71	Control Surface Effectiveness, Initial Design Variable Configuration, Mach 0.9	111
72	Control Surface Effectiveness, Initial Design Variable Configuration, Mach 1.2	111
73	Trim for 90 deg/sec Roll Rate, Initial Design Variable Configuration, Mach 0.9	111
74	Trim for 90 deg/sec Roll Rate, Initial Design Variable Configuration, Mach 1.2	112
75	Control Surface Effectiveness, Category I Optimized (9g load) Configuration, Mach 0.9	113

List of Figures (Cont'd)

Figure	Title	Page
76	Control Surface Effectiveness, Category I Optimized (9g load) Configuration, Mach 1.2	114
77	Trim for 90 deg/sec Roll Rate, Category I Optimized (9g load) Configuration, Mach 0.9	114
78	Trim for 90 deg/sec Roll Rate, Category I Optimized (9g load) Configuration, Mach 1.2	115
79	Trim for 90 deg/sec Roll Rate, Category II Optimized (Single Surface) Configuration, Mach 1.2	116
80	Trim for 90 deg/sec Roll Rate, Category II Optimized (Multiple Surfaces) Configuration, Mach 0.9	116
81	Trim for 90 deg/sec Roll Rate, Category III Optimized (Single Surface) Configuration, Mach 1.2	118
82	Trim for 90 deg/sec Roll Rate, Category III Optimized (Multiple Surfaces) Configuration, Mach 0.9	119

Foreword

This report was prepared by Dr. Frank Eastep, Dayton, Ohio for CSA Engineering, Inc., Palo Alto, California. It describes the work performed under CSA Prime Contract No. F33615-94-C-3200 in response to subcontract 3413.06 and 3413.21 entitled "Development of Preliminary Design Models for F/A-18 Active Aeroelastic Wing Application". The contractual period was from October 6, 1994 through December 15, 1995. Mr. Gordon Negaard of ASIAC was the technical monitor.

The work was conducted under the Structural Technology Integration Core Area for the Active Aeroelastic Wing Integrated Product Team with Mr. Ed Pendleton as chairman. Mr. Pendleton set the goals and directions for the AAWIPT specifically for the In-flight Demonstrator Program of AAW technology. Appreciation is given the structural members of the AAWIPT, in particular, Mr. Ray Kolonay who guided the direction of the analysis task, Mr. Ed Forster and Lt Gerald Andersen who provided the numerical computations. A special thanks is given to Mr. Ed Forster who provided most of the graphics for this report. Mr. Rudy Yurkovich and Mr. Eric Reichanbach of McDonnell Douglas Aircraft Company are acknowledged for the information they provided on F/A-18 aircraft.

DEVELOPMENT OF PRELIMINARY DESIGN METHODS FOR F/A-18 ACTIVE AEROELASTIC WING APPLICATION

SECTION I

INTRODUCTION

In the mid 1980's G. Miller of Rockwell International Corporation advanced a design concept, which was called the Active Flexible Wing[1]. This design concept used, rather than avoided, wing flexibility to provide weight savings and improved aerodynamics for high performance fighter aircraft. In the Active Flexible Wing design concept, weight savings were to be obtained from two primary sources 1) a flexible wing with lower structural weight than a corresponding stiff wing and 2) no horizontal tail required. At the present time this design concept is referred to as Active Aeroelastic Wing (AAW) technology.

In conventional wing design aeroelastic twist is permitted in different Mach regimes (subsonic, transonic and supersonic). However, a direct result of this twist is the degradation of roll performance (in the form of aileron efficiency) over much of the flight envelope. Traditional design techniques would require a "rolling tail" added to the aircraft to provide acceptable roll performance. However, in the AAW design concept, multiple leading and trailing edge control surfaces are used in various combinations to provide acceptable roll performance. For an AAW design an active roll control system is required to efficiently manage the rolling of the vehicle.

To demonstrate the proof of the concept of AAW designs, Pendleton, et al[2] conducted a wind tunnel test of a 1/5 scale model of the F-16 Agile Falcon. The concept exploited wing flexibility and active leading and trailing edge control surfaces, up to and beyond reversal, to provide high-performance roll rates without the use of all-movable horizontal tails. Further wind tunnel tests conducted by Rockwell, the Air Force and NASA were highly successful, thus providing further proof of the AAW concept and are presented in a special issue of the Journal Aircraft[3].

Active Aeroelastic Wing Technology has been demonstrated through analysis and wind tunnel testing. It is additionally necessary to conduct an in-flight demonstration of AAW utilizing a current light-weight high performance fighter to convince aircraft designers of the use of AAW in future designs. The F/A-18 has been selected as the appropriate aircraft for the in-flight demonstration of AAW. The initial wing of the F/A-18 used during early flight testing exhibited outboard aileron reversal at approximately Mach 0.6 at sea level severely limiting the vehicle roll performance. The desire to improve the roll performance deficiency dictated both structural modifications, the traditional stiffening of wing to avoid reversal, and control surface modifications, with the rudiments of active aeroelastic wing technology. The in-flight demonstration program will eliminate the additional stiffening returning the wing to the initial wing but will use AAW technology to provide acceptable roll performance.

Active Aeroelastic Wing (AAW) technology is among recent endeavors, including a flight research program initiative[4], to address the way in which rolling maneuvers are executed. The AAW concept integrates aerodynamics, controls, and structures disciplines to maximize aircraft performance. Using traditional design methods, the reduction of control surface effectiveness due

to flexibility is viewed undesirable. Wing aeroelastic flexibility is utilized by AAW technology by employing multiple leading and trailing edge control surfaces as "tabs" which twist the wing. In AAW technology, little control surface deflection is required for aircraft maneuvers and the flexible wing actually twists less than a conventional stiff wing. The potential benefits of the technology include maximization of maneuver control power for rolling and pitching, minimization of structural loads, and minimization of drag[5]. These benefits can be realized on a wing that is more flexible than a conventional stiff design, which indicates the possibility of weight savings and/or a more efficient aerodynamic wing.

The purpose of this effort has been to explore the development of a preliminary design finite element model of the F/A-18 aircraft for the Active Aeroelastic Wing Integrated Product Team (AAWIPT). This task has been split into several stages in order to assemble the model. The first stage was to document the static, dynamic, and aeroelastic responses of the F/A-18 aircraft. The second stage was to gather all geometric information regarding the assembly of the wing, and create a preliminary model with initial component sizing and mass data. The third stage will integrate the results of the first two stages to create a model in which the sizes of the wing components (skins, spar caps, spar webs, rib caps, and rib webs) will accurately represent the static, dynamic, and aeroelastic responses of the F/A-18 aircraft. The built-up finite element model of the wing will be used to explore the benefits of AAW technology on the F/A-18 aircraft testbed in order to develop design guidance on future aircraft.

The lack of in-house experience with the F/A-18 aircraft required the acquisition of a finite element model for aeroelastic studies. The acquired beam/rod representation of the F/A-18 aircraft, although well suited for analytic studies, could not be used for optimization studies due to the limiting nature of the simplified finite element model. The analytical studies performed using the beam/rod model of the F/A-18 aircraft were classified into dynamic, dynamic aeroelastic, static, and static aeroelastic disciplines. The beam/rod model has been primarily analyzed using the Automated Structural Optimization System (ASTROS)[6], and the results have been compared with The MacNeil-Schwendler Corporation version of the NASA Structural Analysis code (MSC/NASTRAN)[7] results as well as experimental data. The history of this effort, along with the results are documented to enable future studies of a more refined model. This document fulfills the requirements of the first stage of this effort.

The creation of a preliminary design model required detailed geometric and structural information on the F/A-18 wing. A geometric model of the wing surface was assembled utilizing acquired information on the aerodynamic planform, airfoil sections, wing twist, and wing launcher rail. The structural layout of spar and rib locations, including initial component sizing was determined from assembly drawings of the F/A-18 wing, as shown in Figure 1. This preliminary model defines the level of structural detail necessary for the future design studies which will incorporate AAW technology. The completed preliminary design model of the F/A-18 wing concludes the

second stage of this effort.

The final stage requires the correlation of the static, dynamic, and aeroelastic responses of the preliminary design finite element model with actual F/A-18 aircraft data. The result of this stage will be the final sizing of the components of the wing box structure: the thicknesses of the skins, spar webs, and rib webs, as well as the areas of the spar caps and rib caps. The third stage of this effort will be completed by McDonnell Douglas Aircraft Company, the manufacturer of the F/A-18 aircraft.

The built-up finite element model of the F/A-18 wing will be used in future studies incorporating Active Aeroelastic Wing Technology. Design studies will focus on the minimization of aircraft weight with strength, buckling, flutter, and roll performance constraints. Possible further studies would include maximization of control power, minimization of maneuver loads, and minimization of drag. The preliminary design model of the F/A-18 wing is the first crucial step for proof of benefits to utilizing AAW technology in the design stage of future aircraft.

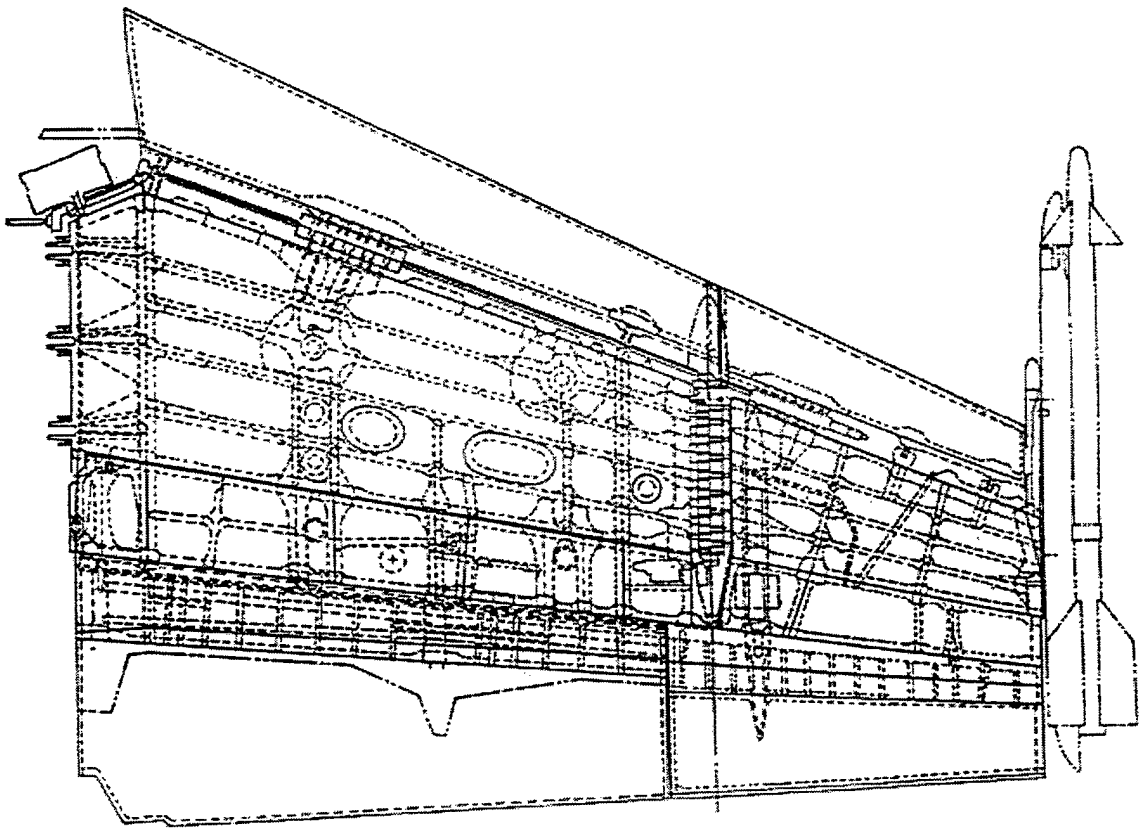

Figure 1: Assembly Drawing of the F/A-18 Wing with Detailed Wing Box Structural Elements, Control Surfaces, and Tip Missile Launcher

SECTION II

DOCUMENTATION OF THE F/A-18 AIRCRAFT

The information received on the F/A-18 aircraft was essential for the initiation and the completion of this effort. Since the F/A-18 aircraft is an operational weapon system of the United States Navy, it was imperative to gather information that would lead to accurate analytical studies; however, it was essential not to gather or utilize any confidential or classified information. The acquisition of information was accomplished by contacting the STARS Team of Analytical Services & Materials, Inc. (AS&M) and the Structural Dynamics Group of McDonnell Douglas Aircraft Company (MDA). The STARS Team of AS&M have extensive data on the F/A-18 aircraft due to their involvement in the NASA Dryden flight test programs with the F/A-18 High Alpha Research Vehicle (HARV) and F/A-18 Systems Research Aircraft (SRA). The Structural Dynamics Group of MDA has been responsible for the static, dynamic, and aeroelastic analyses of the F/A-18 production aircraft, and therefore is considered to be the fundamental experts on that weapon system. Other information has been acquired through publications in journals and conference proceedings. The documentation acquired is outlined to accurately portray the level of detailed information which has been made available to this effort.

Information was first received from AS&M STARS Team for the F/A-18 SRA dynamic and aeroelastic characteristics, along with a finite element input deck for analysis. The materials received included descriptive diagrams of the beam/rod model, with views depicting the left half of the aircraft, the wing, and the vertical tail. An assembly diagram of the F/A-18 wing illustrated the structural layout of spar and rib locations. A weight generation report of the F/A-18 SRA indicated the aircraft weight and center of gravity location for the configuration noted as 'clean wing, no stores, heavy fuel'. An unsteady aerodynamic paneling diagram depicted modeling for all major aircraft components including the fuselage, wing, horizontal stabilator, vertical tail, strake, and tip missile launcher. The documented results of the F/A-18 SRA included free vibration frequencies, mode shape descriptions, and generalized masses along with dynamic aeroelastic flutter speeds and frequencies for both symmetric and anti-symmetric boundary conditions for the configuration noted as 'baseline, heavy fuel'. The input deck and modal analysis results launched the dynamic behavior study of the F/A-18 SRA.

Concurrent to the finite element model received from the NASA Dryden STARS Team, a generic built-up model resembling the F/A-18 wing was received as part of the Adaptive Multi-Dimensional Integrated Control (AMICS) contract with Northrop Grumman Corporation. This finite element model did not represent the structural layout of spars and ribs in the F/A-18 wing; however, the wing aerodynamics were accurately modeled through input cards which detailed the planform, airfoil sections, wing twist, and wing anhedral. The diagram of the wing box substructure and the detailed aerodynamic model initiated the development of the preliminary design model geometry.

More information was provided by the AS&M STARS Team during a fact finding visit. Renderings of the top, side, and front view of the F/A-18 aircraft with accompanying dimensions

were provided for planform reference. An input deck from the Structural Analysis Research System (STARS) of the F/A-18 SRA indicated the coordinates of the fuselage, wing, horizontal stabilator, vertical tail, strake and missile launcher aerodynamic panels. Electronic data files of the F/A-18 SRA mode shape deflections were provided for future comparisons of the free vibration analyses. Assembly drawings of the inner and outer wing box structures were acquired for initial sizing of the preliminary design model elements. The provided mode shapes established the comparison of free vibration results of ASTROS with those reported by the STARS Team. The aerodynamic planform information generated the modeling of the unsteady aerodynamic surfaces for flutter analysis. The sizing information commenced the study of the static behavior of the preliminary design model.

In order to compare in-house flutter analyses with previous results, a final package of information was provided by the AS&M STARS Team. Included were velocity damping (V-g) diagrams which originated from McDonnell Douglas for the F/A-18 A/B production aircraft for symmetric and anti-symmetric boundary conditions at Mach 0.9, sea level flight conditions. V-g diagrams from the STARS analyses were also provided for the F/A-18 SRA for symmetric and anti-symmetric boundary conditions at Mach 0.9, sea level flight conditions. The flutter results established the comparison of ASTROS results with previous analyses.

Discrepancies between the AAWIPT free vibration results and the results reported by the AS&M STARS Team prompted contact with MDA to resolve this essential issue. An F/A-18 finite element input deck was provided for comparison with the deck obtained from the AS&M STARS Team. Also, MDA provided the reports titled: "F/A-18 Airframe Compliance and Ground Vibration Data Report", and "F/A-18 Airframe Compliance and Ground Vibration Data Report, Addendum B". These reports contained detailed information on the free vibration frequencies and mode shapes of the aircraft and its components obtained theoretically and experimentally. A report titled "Actual Weight and Balance Report for Model F-18A Airplane" which accurately reports the mass and inertia characteristics of the components of the F/A-18 aircraft was used in the comparison. The input deck and ground vibration test reports established a second comparison for free vibration results. The weight and balance report commenced the dynamic behavior study of the preliminary design model.

The most important document which affected the flutter analysis was a paper[8] provided by MDA which identified the flutter velocity, frequency, and modal interaction of the F/A-18 aircraft. Through a meeting with Rudy Yurkovich, the author of the paper[8], it was possible to determine the important aspects of the flutter analysis which could be later incorporated in this effort.

The static aeroelastic information was solely provided by MDA in the form of aileron reversal speeds. The flight envelope of the F/A-18 aircraft is defined by the aileron reversal line showing Mach number verses altitude of this performance limitation. The aileron reversal dynamic pressure was utilized to check the capability of the beam/rod finite element model to predict the static aeroelastic behavior of the actual aircraft.

SECTION III

BEAM/ROD MODEL

The beam/rod model utilizes a half model of the F/A-18 fighter aircraft where the fuselage, wing, horizontal tail, and vertical stabilator are modeled as beams. The control surfaces are also modeled as beams, with rigid bars connecting to the hinge line and springs modeling actuators. Aerodynamic surfaces are modeled for the wing and horizontal stabilator. The structural and aerodynamic model is illustrated in figure 2.

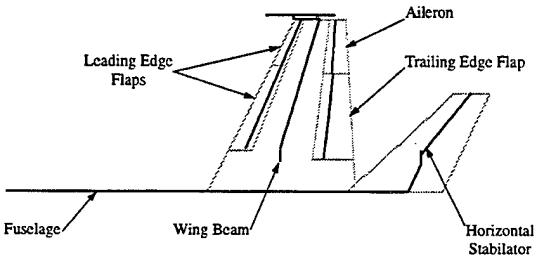

Figure 2: Diagram of Fighter Aircraft Finite Element and Aerodynamic Model

The structural element properties simulate those of a generic F/A-18 aircraft[9]. The fuselage beam runs along the centerline from the cockpit to the horizontal tail. The wing, stabilator, and control surface beams are located along their respective elastic axes. The wing and stabilator beams both run approximately along the 40% chord of their respective aerodynamic surfaces.

The wing and stabilator aerodynamic surfaces are modeled such that they extend to the aircraft centerline. The wing has a semi-span of 225 in., with a root chord of 190 in. and a tip chord of 65 in., which indicates a 3.5 aspect ratio. The wing leading edge is swept at 27 deg. The stabilator has a semi-span of 130 in., with a root chord of 120 in. and a tip chord of 45 in., which indicates a 3.2 aspect ratio. The stabilator leading edge is swept at 47 deg. The leading edge hinge line is at the 19% chord. The leading edge inboard flap starts at a span location of 54 in. and extends to the 165 in. span station. The leading edge outboard flap continues from the 165 in. span station to the wing tip. The trailing edge hinge line is at the 68% chord. The trailing edge flap starts at a span location of 42 in. and extends to the 154 in. span station. The aileron continues from the 154 in. span station to the wing tip.

Analysis began with a check of the structural model. Dynamic analyses provided validation of behavioral responses of a typical fighter aircraft[9]. The spline was checked by observing the 'rigid' and 'rigid splined' stability and control derivatives. Near equality of these two quantities indicates

a good spline. The wing and tail are modeled with flat plate aerodynamics for antisymmetric trim analyses.

Documentation of the changes made to the finite element model input deck was essential to trace the differences between the original and the current version utilized for analysis. The analyses performed prompted some of the necessary changes. A combined history of the changes made to the model and the analyses performed has provided a review of the process to meet the analytical requirements and documentation of the limitations of the beam/rod model.

MSC/NASTRAN input decks for the F/A-18 Systems Research Aircraft (SRA) and F/A-18 High Angle-of-attack Research Vehicle (HARV) were acquired from the AS&M STARS Team. The files required cosmetic changes in order to yield a running input deck. These changes consisted mostly of adjusting the columns of the input card fields. The most extensive changes were made due to an A-set/M-set duplication error, which required several grid points to be removed from ASET1 cards. A functional input deck was verified when reasonable free vibration analysis results were obtained from MSC/NASTRAN. The results were correlated with those reported by the AS&M STARS Team for the F/A-18 SRA. All of the symmetric frequencies and mode shapes, most of the anti-symmetric frequencies and mode shapes, and the total mass and center of gravity location matched; however, the generalized masses did not match those reported by the AS&M STARS Team. The F/A-18 SRA finite element beam/rod model would be the only model considered in further studies.

The input deck for the F/A-18 SRA was then converted so that ASTROS could be used for all future analyses. The changes required the addition of an identity field on SPC1 and ASET1 cards due to the multiple boundary condition capability of ASTROS. RSPLINE cards were removed because they are not supported by ASTROS. A functional input deck was verified when the free vibration analysis results from ASTROS matched the MSC/NASTRAN results.

The beam/rod model of the F/A-18 SRA was changed from a left hand model to a right hand model so that aeroelastic studies could be performed. The ASTROS input deck was changed so that the x-axis pointed in the free stream direction, the y-axis pointed out the wing, and the z-axis completed the right hand coordinate system. Coordinates of GRID and CONM2 cards were adjusted; mass moments of inertia of CONM2 cards were changed; and the degrees of freedom for RBAR and CELAS2 cards were switched to complete the transformation. A functional right hand model was verified when the free vibration analysis results from ASTROS were matched to those results from the left hand model.

In order to perform dynamic aeroelastic analysis on the F/A-18 SRA beam/rod model, an aerodynamic planform was defined for the aircraft. The unsteady model from the Structural Analysis Routines (STARS) input deck was extracted, transformed, and included in the ASTROS input deck. The input deck was functional for flutter analysis; however, the results did not match those reported by the AS&M STARS Team. The lack of flutter velocity and frequency correlation was attributed to the differences in the generalized masses in the free vibration results.

An MSC/NASTRAN input deck for the production F/A-18 C/D aircraft was provided by MDA. The dynamic analysis of the F/A-18 C/D model correlated almost completely with the AAWIPT

results with the exception of the vertical tail modal frequencies. The frequencies, mode shapes, as well as the generalized mass and stiffness matched for all the other modes not explicitly involving motion of the vertical tail. A comparison of the production C/D input deck with the SRA input deck revealed that the only differences were in the modeling of the vertical tail. This discrepancy was attributed to the fact that the SRA is based on the production A/B aircraft. This correlation of free vibration results completed the dynamic analysis of the F/A-18 SRA beam/rod model.

Without correlation of the AAWIPT dynamic analysis of the F/A-18 SRA beam/rod model to the AS&M STARS Team results, the comparison of flutter velocity, frequency, and modal interaction was not considered essential for the completion of flutter analysis. The splined aerodynamic mode shapes were compared to their structural counterparts to ensure proper modeling of the unsteady aerodynamics panels of the aircraft components. The flutter analysis was completed by removing any unnecessary aerodynamic panels and omitting any nonessential mode shapes in order to reduce the complexity while maintaining the same flutter characteristics: velocity, frequency, and modal interaction. The unsteady aerodynamic panels modeling the fuselage, strake, horizontal stabilator, and vertical tail were removed, and all mode shapes involving empennage motion were omitted. The wing aerodynamics were extended from the wing root to the aircraft centerline. Flutter analyses were performed for multiple Mach numbers, at multiple altitudes (through the use of density ratios), for the wing configuration without a tip missile. Documentation of the flutter velocities, frequencies, and modal interactions completed the flutter analysis of the F/A-18 SRA beam/rod model.

Although the F/A-18 beam/rod model was constructed and correlated only with the dynamic behavior of the actual aircraft, it was utilized in static analyses. A point load and a moment were applied to the tip of the wing beam to characterize the stiffness of the F/A-18 wing in terms of the resultant displacement and rotation. Since there was no available data on the stiffness of the actual F/A-18 wing, this static analysis provided the stiffness characteristics for beam-rod model.

The unsteady aerodynamic model used for flutter analysis was converted for steady aerodynamic analyses. The tip missile launcher aerodynamic panel was discarded as it would have relatively little effect on the anti-symmetric roll characteristics of the aircraft. The wing aerodynamic panel resolution was increased by adding chordwise and spanwise divisions near the control surface hinge lines. The pressure distributions corresponding to symmetric and anti-symmetric aerodynamic loading for all flap deflections were checked. The control surface effectiveness values were determined for a range of dynamic pressures in order to determine the point of roll reversal. The roll reversal dynamic pressures could not be correlated with the actual aircraft data. This deficiency was attributed to the modeling of the wing beam material properties as well as the insufficiencies of the steady aerodynamic code, Unified Subsonic and Supersonic Aerodynamics (USSAERO), in ASTROS. Control surface trim deflections were determined for a range of dynamic pressures in order to examine the benefits of using multiple blended control surfaces to meet roll performance requirements of the F/A-18 aircraft. This study was accomplished using the AMICS enhanced version of ASTROS. Documentation of the roll reversal dynamic pressures as well as the control surface deflections for roll performance requirements completed the static aeroelastic analysis of the F/A-18 SRA beam/rod model.

SECTION IV

DYNAMIC ANALYSIS

The equations of motion for the system are:

$$[M]\{\ddot{x}\} + [K]\{x\} = \{f(t)\} \tag{1}$$

where $[M]$ is the mass matrix, $[K]$ is the stiffness matrix, $\{\ddot{x}\}$ is the vector of nodal accelerations, and $\{x\}$ is the vector of nodal displacements. The vector of forcing functions, $\{f(t)\}$, is assumed to be $\{0\}$ for the case of free vibration. The equation is reduced to an eigenvalue problem by substituting $\{x\} = \{u\}e^{i\omega t}$:

$$\left[[K] - \omega^2[M]\right]\{u\} = \{0\} \tag{2}$$

where ω is the natural frequency, and $\{u\}$ is the mode shape. The generalized mass and stiffness matrices are the diagonal matrices defined by multiplying the respective mass and stiffness matrices by the mode shape vector, and pre-multiplying by its transpose:

$$[M_{GEN}] = \{u\}^T[M]\{u\} \tag{3}$$

$$[K_{GEN}] = \{u\}^T[K]\{u\} \tag{4}$$

The frequency, mode shape, generalized mass and stiffness are used to characterize the dynamic behavior of the F/A-18 aircraft models. The wing (and associated control surfaces and launcher configuration), fuselage, horizontal stabilator, and vertical tail are the major components which describe motion.

Beam/Rod Model Dynamic Analysis

The structural dynamics of the F/A-18 SRA aircraft have been analyzed under two boundary conditions, symmetric and anti-symmetric. The supported rigid body motions corresponding to symmetric boundary conditions are fore/aft, plunge, and pitch. The supported rigid body motions associated with anti-symmetric boundary conditions are side slip, roll, and yaw.

Three configurations of the tip missile assembly were utilized to explore the structural dynamics of the F/A-18 SRA beam/rod model. The finite element model of the tip missile and launcher rail can be seen in Figure 3. The first configuration, with a tip missile, is shown in the figure. The second configuration, without a tip missile, requires that the tip missile structure, masses, and

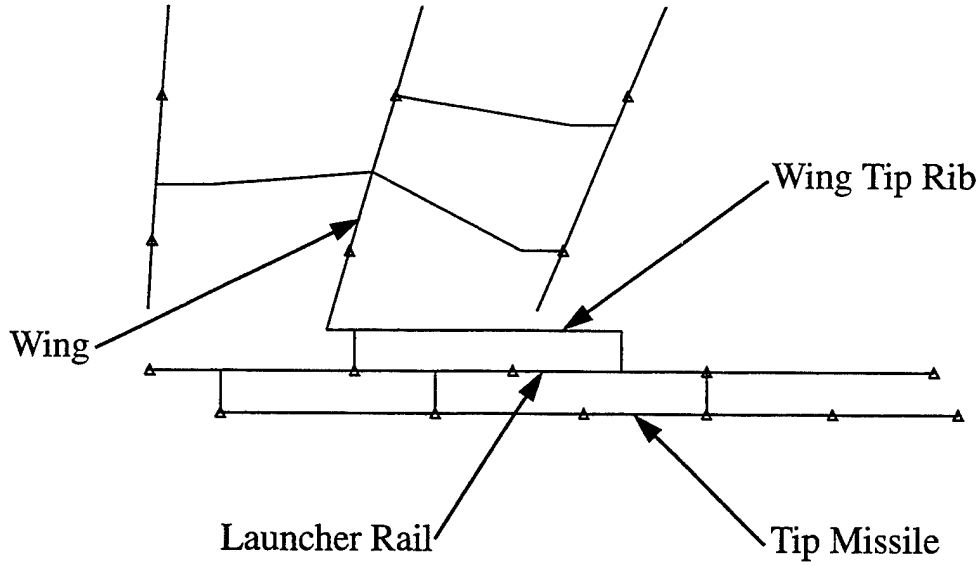

Figure 3: Missile Launcher Structural Finite Element Model of the F/A-18 Aircraft.

rigid attachments be omitted but the wing tip rib and missile launcher rail remain. The last configuration, without a missile launcher, requires the omission of both the tip missile and launcher rail.

The eigen analysis was performed in both ASTROS and MSC/NASTRAN, utilizing the Modified Givens Method such that the eigenvectors were normalized with respect to the maximum nodal displacement. The results of the eigenanalysis matched for both ASTROS and MSC/NASTRAN and are reported in Tables 1 through 6. A description of the mode shape, frequency, and generalized mass and stiffness corresponding to the first twenty-one modes for each missile configuration and boundary condition are indicated.

There are several consistent trends which can be observed from the results in Tables 1 through 6. These trends are identified by three classifications: trends which are related to the boundary conditions, trends which are related to the tip missile and launcher rail configuration, and trends which are independent of both the boundary condition and missile/launcher configuration.

Trends which are related to the boundary conditions are independent of the tip missile and launcher configuration. Allowing the overall aircraft to have rigid body motion in the symmetric or anti-symmetric degrees of freedom changes the aircraft component mode shapes, which are dependent on the relative rigid body moments of inertia of the aircraft. This difference in mode shape is quantified by the higher frequencies of the flexible modes under symmetric or anti-symmetric boundary conditions compared to the fully constrained case. The symmetric and anti-symmetric flexible frequencies converge to the fully constrained case as the aircraft moments of inertia tend towards infinity. The wing first and second bending modes have lower frequencies under boundary conditions of symmetry than those of anti-symmetry. The wing first and second torsion frequencies stay relatively the same between symmetric and anti-symmetric boundary conditions.

Table 1: Eigen Analysis of F/A-18 Aircraft with a Tip Missile for Symmetric Boundary Conditions

Mode	Shape	Frequency (Hz)	Generalized Mass ($lb_f\ s^2/in$)	Generalized Stiffness (lb_f/in)
1	RB Fore/Aft	0.00	---	---
2	RB Plunge	0.00	---	---
3	RB Pitch	0.00	---	---
4	W1B	4.20	0.80100	559.
5	W1T	8.54	0.31473	907.
6	F1B	9.23	1.31501	4419.
7	W2B	13.54	0.13548	981.
8	S1B	13.66	0.09613	708.
9	W1F/AB	14.44	2.18346	17985.
10	V1B	16.19	0.13393	1387.
11	F2B	19.44	1.13355	16913.
12	TEFR	23.02	0.37773	7900.
13	W2T	26.76	0.30410	8595.
14	S1F/AB	28.23	0.11592	3646.
15	TMB	32.77	2.27909	96597.
16	F3B	32.95	2.56792	110044.
17	LEFR	37.18	1.34934	73631.
18	W2F/AB	39.29	1.14361	69703.
19	S2B	44.57	0.15987	12540.
20	W3B	45.92	0.31147	25925.
21	V2B	47.03	0.65515	57206.

Table 2: Eigen Analysis of F/A-18 Aircraft with a Tip Missile for Anti-Symmetric Boundary Conditions

Mode	Shape	Frequency (Hz)	Generalized Mass ($lb_f\ s^2/in$)	Generalized Stiffness (lb_f/in)
1	RB Side Slip	0.00	---	---
2	RB Roll	0.00	---	---
3	RB Yaw	0.00	---	---
4	W1B	6.29	0.55872	872.
5	F1B	8.01	3.00313	7598.
6	W1T	9.00	0.42956	1373.
7	S1B	13.17	0.06411	439.
8	W1F/AB	14.05	1.47115	11471.
9	V1B	15.13	0.30254	2736.
10	W2B	17.66	0.57613	7095.
11	F2B	20.68	1.26969	21430.
12	F1T	22.02	1.56266	29914.
13	TEFR	23.15	0.40496	8565.
14	W2T	27.00	0.31312	9013.
15	S1F/AB	28.37	0.14892	4731.
16	TMB	32.62	1.36886	57512.
17	F3B	34.35	2.23201	103978.
18	W2F/AB	37.46	0.96418	53417.
19	LEFR	37.94	1.40782	80005.
20	W3B	42.93	0.82333	59894.
21	S2B	45.78	0.16749	13857.

Table 3: Eigen Analysis of F/A-18 Aircraft without a Tip Missile for Symmetric Boundary Conditions

Mode	Shape	Frequency (Hz)	Generalized Mass ($lb_f\ s^2/in$)	Generalized Stiffness (lb_f/in)
1	RB Fore/Aft	0.00	---	---
2	RB Plunge	0.00	---	---
3	RB Pitch	0.00	---	---
4	W1B	5.65	0.74217	935.
5	F1B	9.28	1.25524	4268.
6	S1B	13.55	0.06645	481.
7	W1T	13.98	0.32255	2491.
8	V1B	16.19	0.13410	1388.
9	W2B	17.07	0.45392	5224.
10	W1F/AB	17.71	1.54042	19067.
11	F2B	19.68	1.26247	19300.
12	TEFR	23.33	0.37416	8043.
13	S1F/AB	28.23	0.11597	3648.
14	W2T	29.41	0.34342	11724.
15	F3B	32.85	3.47345	148000.
16	LEFR	38.09	0.64715	37075.
17	W3B	43.49	0.78130	58327.
18	S2B	45.27	0.12068	9763.
19	V2B	46.95	0.69081	60127.
20	F4B	47.58	3.77301	337262.
21	S1T	48.90	0.18021	17009.

Table 4: Eigen Analysis of F/A-18 Aircraft without a Tip Missile for Anti-Symmetric Boundary Conditions

Mode	Shape	Frequency (Hz)	Generalized Mass ($lb_f\ s^2/in$)	Generalized Stiffness (lb_f/in)
1	RB Side Slip	0.00	---	---
2	RB Roll	0.00	---	---
3	RB Yaw	0.00	---	---
4	F1B	8.12	3.28653	8552.
5	W1B	8.61	0.80660	2363.
6	S1B	13.32	0.06439	451.
7	W1T	14.64	0.40733	3444.
8	V1B	15.57	0.35030	3352.
9	W1F/AB	16.68	0.61534	6757.
10	W2B	18.22	2.37891	31169.
11	F2B	21.64	2.73689	50618.
12	F1T	22.55	1.58368	31784.
13	TEFR	23.48	0.46721	10168.
14	S1F/AB	28.48	0.14284	4573.
15	W2T	29.44	0.33826	11575.
16	F3B	35.96	1.06672	54471.
17	LEFR	38.00	0.88036	50176.
18	W3B	40.08	1.33927	84925.
19	OBWT	45.20	0.62374	50298.
20	S2B	45.81	0.18020	14930.
21	S1T	48.24	0.16239	14920.

Table 5: Eigen Analysis of F/A-18 Aircraft without a Missile Launcher for Symmetric Boundary Conditions

Mode	Shape	Frequency (Hz)	Generalized Mass ($lb_f\ s^2/in$)	Generalized Stiffness (lb_f/in)
1	RB Fore/Aft	0.00	---	---
2	RB Plunge	0.00	---	---
3	RB Pitch	0.00	---	---
4	W1B	6.67	0.71487	1255.
5	F1B	9.35	1.29411	4464.
6	S1B	13.60	0.05639	412.
7	V1B	16.19	0.13402	1387.
8	W2B	18.20	0.78187	10228.
9	W1F/AB	19.69	1.36241	20845.
10	F2B	20.42	0.53969	8883.
11	W1T	22.05	0.47913	9201.
12	TEFR	26.25	0.44194	12026.
13	S1F/AB	28.23	0.11590	3647.
14	F3B	32.85	3.44510	146757.
15	LEFR	37.37	0.71085	39186.
16	W3B	43.81	0.83598	63359.
17	S2B	45.16	0.12081	9729.
18	V2B	46.90	0.78707	68333.
19	F4B	47.73	3.27146	290598.
20	S1T	48.92	0.17300	16346.
21	V1T	50.02	0.23861	23572.

Table 6: Eigen Analysis of F/A-18 Aircraft without a Missile Launcher for Anti-Symmetric Boundary Conditions

Mode	Shape	Frequency (Hz)	Generalized Mass ($lb_f\ s^2/in$)	Generalized Stiffness (lb_f/in)
1	RB Side Slip	0.00	---	---
2	RB Roll	0.00	---	---
3	RB Yaw	0.00	---	---
4	F1B	8.26	2.89143	7780.
5	W1B	10.12	0.59112	2392.
6	S1B	13.68	0.05871	434.
7	V1B	16.00	0.19675	1988.
8	W1F/AB	17.56	1.49574	18212.
9	W2B	18.68	1.50574	20748.
10	W1T	21.94	0.50350	9568.
11	F2B	22.14	2.45415	47495.
12	F1T	23.40	0.53600	11589.
13	TEFR	26.32	0.46402	12688.
14	S1F/AB	28.56	0.14265	4593.
15	F3B	36.27	1.10448	57375.
16	LEFR	37.34	1.23682	68067.
17	W3B	41.10	1.06692	71164.
18	W2T	45.27	0.32529	26314.
19	S2B	46.08	0.27317	22898.
20	S1T	48.14	0.20655	18894.
21		48.80	0.42569	40018.

Trends which are related to the tip missile and launcher rail configuration are independent of the boundary conditions. The wing bending mode frequencies are primarily affected by the inclusion of masses at the wing tip. The wing torsion modes are mainly affected by the inclusion of masses at the leading and trailing edges. The tip missile and launcher rail substantially affect both types of modes as the masses are attached both to the wing tip, and extend beyond the leading edge. The subsequent omission of tip missile and launcher rail raises the wing bending and torsional frequencies. The fuselage bending modes are not affected by the tip missile and launcher rail configuration due to the fact that the fuselage masses are large in comparison to the wing missile launcher.

Trends which correspond neither to the boundary condition, nor to the tip missile and launcher rail configuration are more likely to be described as model consistencies. The stabilator and vertical tail bending mode frequencies, and the leading and trailing edge flap rotation mode frequencies are unaffected by boundary conditions and missile configuration. The empennage masses are small relative to the fuselage masses, therefore the empennage bending modes have converged to the cantilever (fully constrained) frequencies.

The frequencies of the first eighteen flexible mode shapes are noted to lie between 4.0 and 50.0 Hz. The empennage bending frequencies are higher than the wing bending frequencies. The first and second bending frequencies are lower than the corresponding torsion frequencies which are lower than the fore/aft bending frequencies. The generalized mass and stiffness values of the wing mode shapes also follow this trend. The larger generalized mass and stiffness values are associated with fuselage modes, the smaller values with empennage modes.

The first and second wing bending and torsion mode shapes are the most fundamental mode shapes, particularly in flutter analysis. The frequencies of these wing component mode shapes are compared with Ground Vibration Test (GVT) data[8] in Tables 7 and 8 for the configuration with a tip missile, and in Tables 9 and 10 for the configuration without a tip missile. Comparisons are made for both symmetric and anti-symmetric boundary conditions. The results show good agreement between the theoretical frequencies discerned from the finite element method and the experimental frequencies from the GVT.

Table 7: Comparison of Theoretical and Experimental Results for the F/A-18 Aircraft with a Tip Missile for Symmetric Boundary Conditions

Mode	Frequency (Hz)		Difference
	ASTROS	GVT	%
Wing First Bending	4.20	4.37	1.98
Wing First Torsion	8.54	8.89	2.01
Wing Second Bending	13.54	13.48	0.22
Wing Second Torsion	26.76	26.62	0.26

Table 8: Comparison of Theoretical and Experimental Results for the F/A-18 Aircraft with a Tip Missile for Anti-Symmetric Boundary Conditions

Mode	Frequency (Hz)		Difference
	ASTROS	GVT	%
Wing First Bending	6.29	6.68	3.01
Wing First Torsion	9.00	9.22	1.21
Wing Second Bending	17.66	15.38	6.90
Wing Second Torsion	27.00	27.39	0.72

Table 9: Comparison of Theoretical and Experimental Results for the F/A-18 Aircraft without a Tip Missile for Symmetric Boundary Conditions

Mode	Frequency (Hz)		Difference
	ASTROS	GVT	%
Wing First Bending	5.65	5.68	0.27
Wing First Torsion	13.98	13.51	1.71
Wing Second Bending	17.07	16.62	1.34
Wing Second Torsion	29.41	29.26	0.26

Table 10: Comparison of Theoretical and Experimental Results for the F/A-18 Aircraft without a Tip Missile for Anti-Symmetric Boundary Conditions

Mode	Frequency (Hz)		Difference
	ASTROS	GVT	%
Wing First Bending	8.61	9.35	4.30
Wing First Torsion	14.64	14.65	0.03
Wing Second Bending	18.22	16.05	6.33
Wing Second Torsion	29.44	29.13	0.66

Corresponding to the eigen analysis reported in Tables 1 through 6, the mode shapes and frequencies of the flexible modes are plotted in Figures 4 through 9. The depiction of mode shapes helped to clearly describe the major component of motion and allow similarities to be identified regardless of the boundary condition or missile/launcher configuration. More importantly, component coupling in the mode shapes as well as subtle differences in the major component motion can be identified from these illustrations.

Bending and torsion are the most frequently used descriptions of mode shapes. For the case of a beam, the simplest distinction is in the nodal lines (lines of zero deflection) of the mode shape. Bending modes have nodal lines that are perpendicular to the span of the beam, while torsion modes have an additional nodal line which is parallel to the span of the beam. For a cantilever beam, the first mode has one perpendicular node line at the base, the second mode has an additional perpendicular node line located on the span of the beam, and so forth. For a free-free beam, the first mode has two node lines perpendicular to the span of the beam which act as simple supports, the second mode has three node lines, and so forth. The number of nodal lines for a specified motion of bending or torsion indicates the relative frequency of that mode shape, the more node lines indicates the larger frequency. However, this comparison cannot be made of the relative frequencies between bending and torsion frequencies.

The wing, stabilator, and vertical tail components act as cantilever beams, whereas the fuselage acts as a free-free beam. The first bending modes of the aircraft fuselage, wing, stabilator, and vertical tail are easily identifiable, as well as the first torsion mode of the wing, for all boundary conditions and missile/launcher configurations. The higher bending and torsion modes of the aircraft components are not as clear due to component coupling. Also in the higher frequency range are leading and trailing edge flap rotation modes which are hard to distinguish from the higher wing torsion modes.

Similarities in mode shape are readily apparent by the descriptions given in Tables 1 through 6. This can be easily observed in the wing first bending and torsion modes. The wing shows similar features of first bending in figures 4a, 5a, 6a, 7b, 8a, and 9b. Subtle differences are apparent in the coupled empennage displacements, and the modal displacements at the root of the wing. First torsion behavior is evident in figures 4b, 5c, 6d, 7d, 8h, and 9g. The wing displays coupled bending behavior in all the configurations, and empennage coupling in the cases with anti-symmetric boundary conditions. In general, the wing and empennage modes are quite similar.

The mode shapes which show the greatest variations involve the fuselage. The fuselage first bending modes in figures 4c, 5b, 6b, 7a, 8b, and 9a show the same basic cantilever action, but the plane of motion is different between symmetric and anti-symmetric boundary conditions. This affects the wing, stabilator, and vertical tail components as well.

The dynamic analysis was essential to establish the validity of the F/A-18 SRA beam/rod model as an accurate representation of the aircraft. The detailed information on mode shapes is fundamental for the flutter analysis in which the participating modes must be clearly identified.

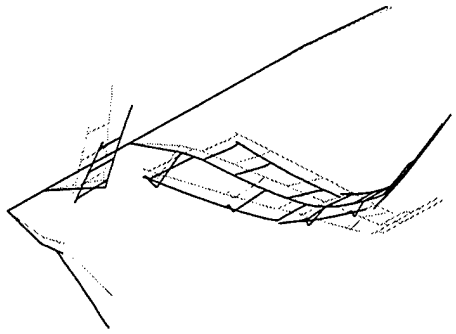

4.20 Hz

a.) Wing First Bending

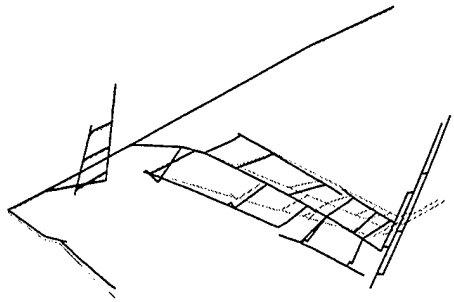

8.54 Hz

b.) Wing First Torsion

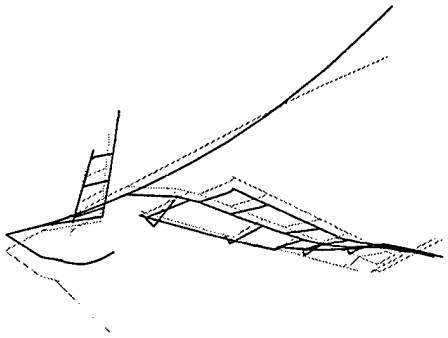

9.23 Hz

c.) Fuselage First Bending

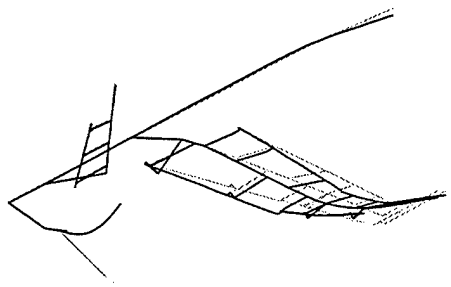

13.54 Hz

d.) Wing Second Bending

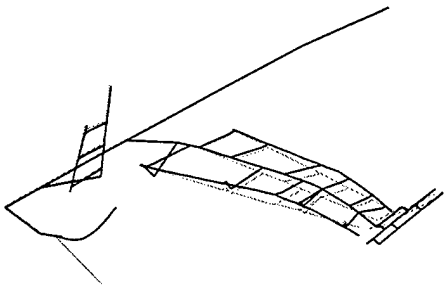

13.66 Hz

e.) Stabilator First Bending

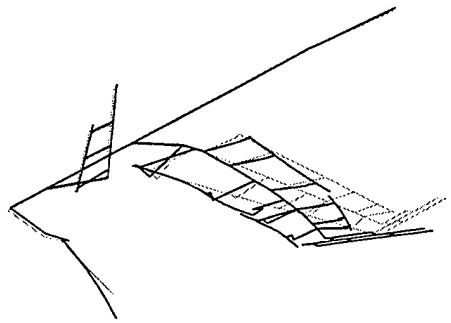

14.44 Hz

f.) Wing First Fore/Aft Bending

Figure 4: Mode Shapes and Frequencies of the F/A-18 Aircraft with a Tip Missile for Symmetric Boundary Conditions.

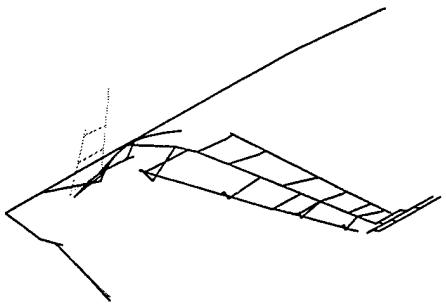

16.19 Hz

g.) Vertical Tail First Bending

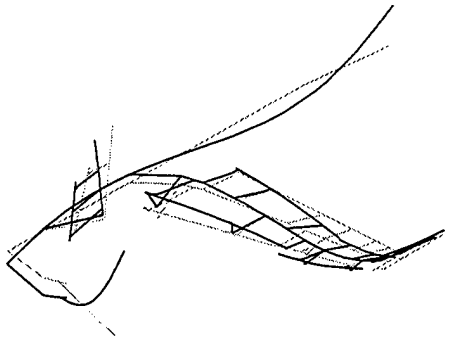

19.44 Hz

h.) Fuselage Second Bending

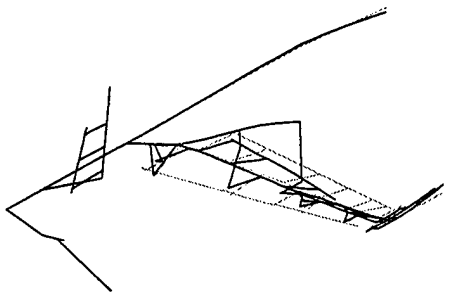

23.02 Hz

i.) Trailing Edge Flap Rotation

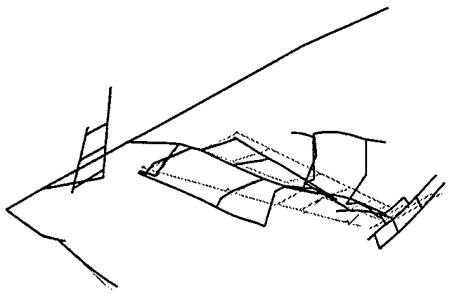

26.76 Hz

j.) Wing Second Torsion

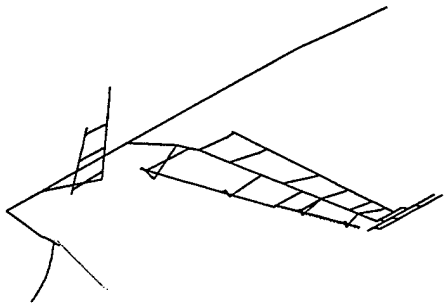

28.23 Hz

k.) Stabilator First Fore/Aft Bending

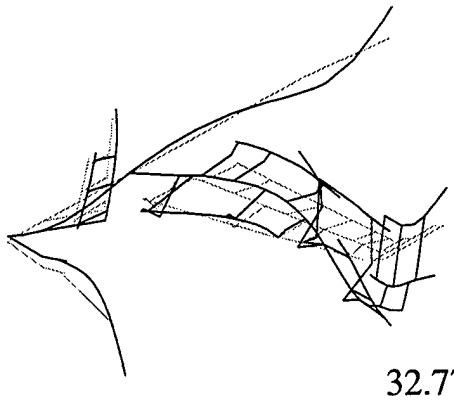

32.77 Hz

l.) Tip Missile Bending

Figure 4 (continued)

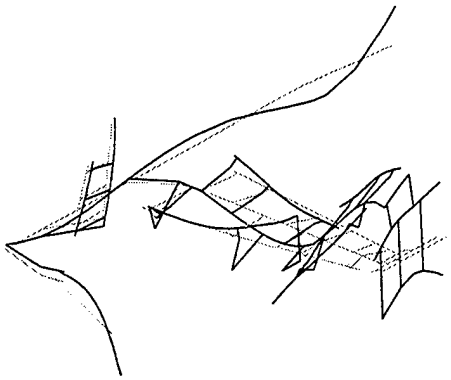

32.95 Hz

m.) Fuselage Third Bending

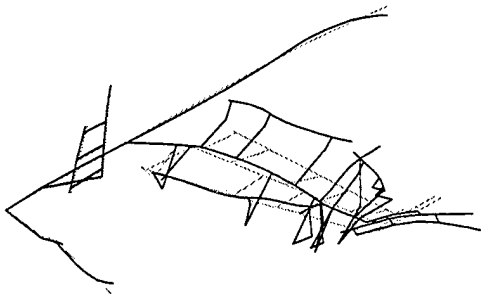

37.18 Hz

n.) Leading Edge Flap Rotation

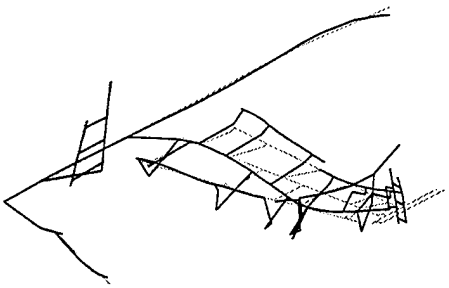

39.29 Hz

o.) Wing Second Fore/Aft Bending

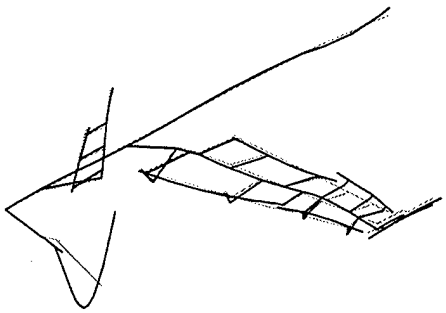

44.57 Hz

p.) Stabilator Second Bending

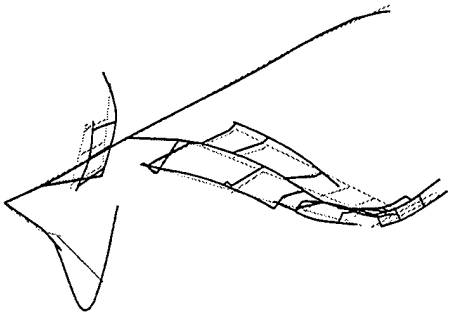

45.92 Hz

q.) Wing Third Bending

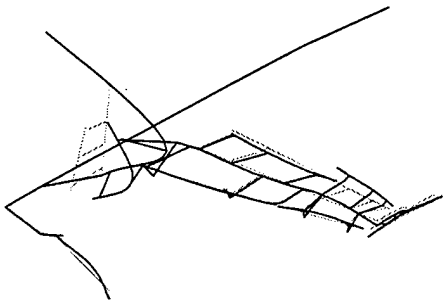

47.03 Hz

r.) Vertical Tail Second Bending

Figure 4 (continued)

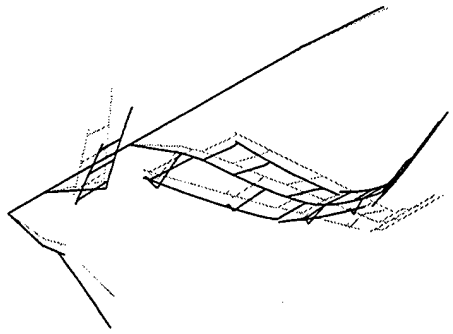

6.29 Hz

a.) Wing First Bending

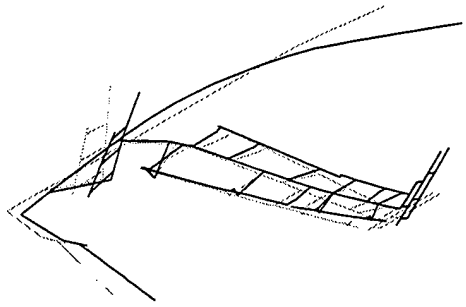

8.01 Hz

b.) Fuselage First Bending

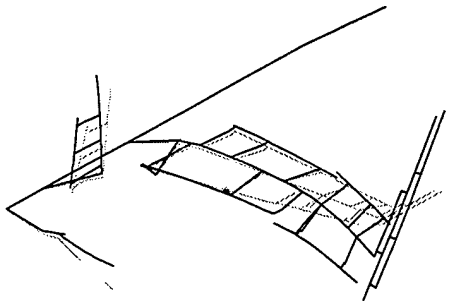

9.00 Hz

c.) Wing First Torsion

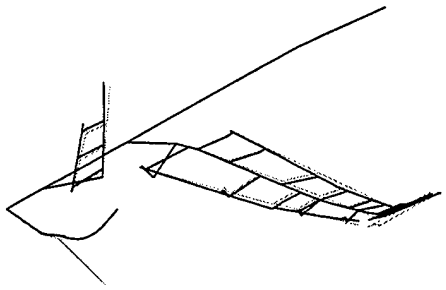

13.17 Hz

d.) Stabilator First Bending

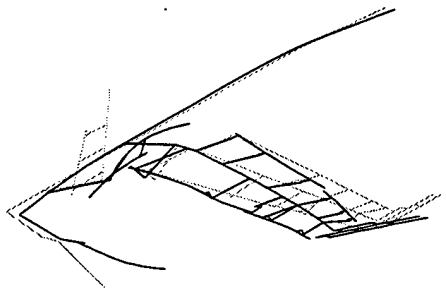

14.05 Hz

e.) Wing First Fore/Aft Bending

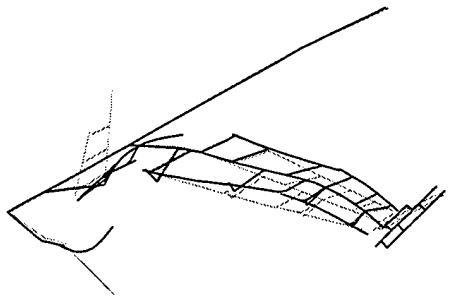

15.13 Hz

f.) Vertical Tail First Bending

Figure 5: Mode Shapes and Frequencies of F/A-18 Aircraft with a Tip Missile for Anti-Symmetric Boundary Conditions

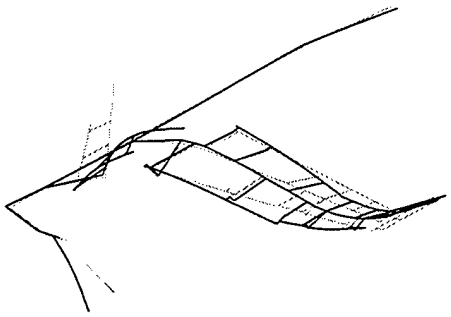

17.66 Hz

g.) Wing Second Bending

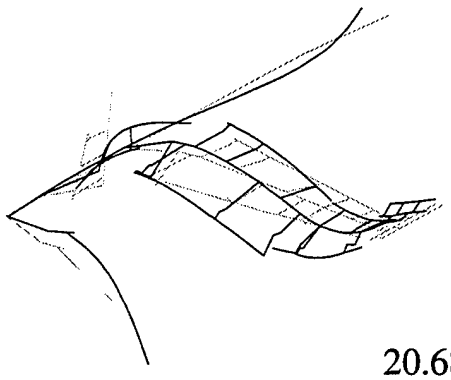

20.68 Hz

h.) Fuselage Second Bending

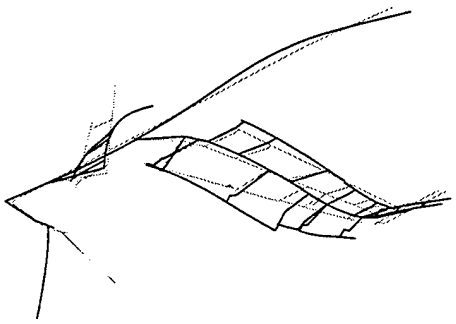

22.02 Hz

i.) Fuselage First Torsion

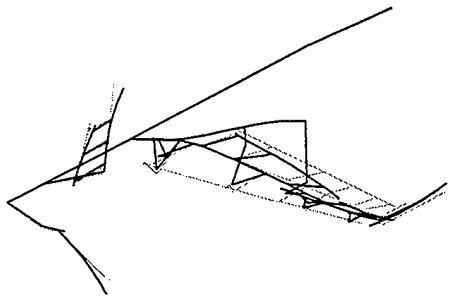

23.15 Hz

j.) Trailing Edge Flap Rotation

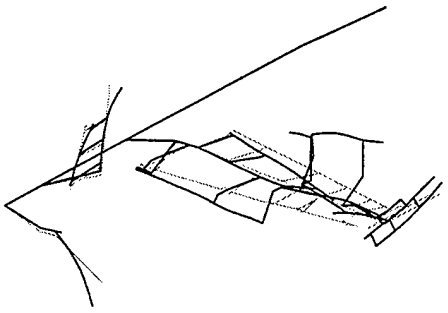

27.00 Hz

k.) Wing Second Torsion

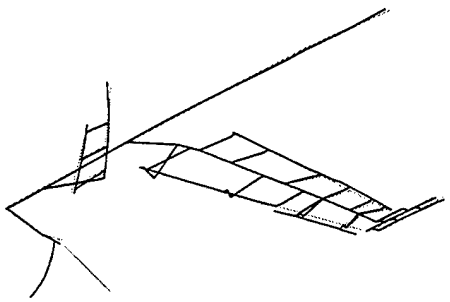

28.37 Hz

l.) Stabilator First Fore/Aft Bending

Figure 5 (continued)

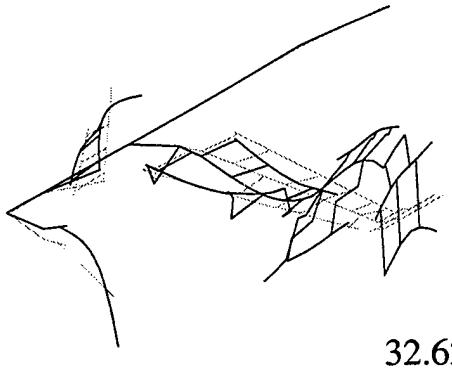

32.62 Hz

m.) Tip Missile Bending

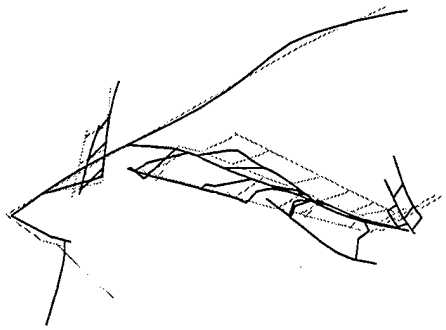

34.35 Hz

n.) Fuselage Third Bending

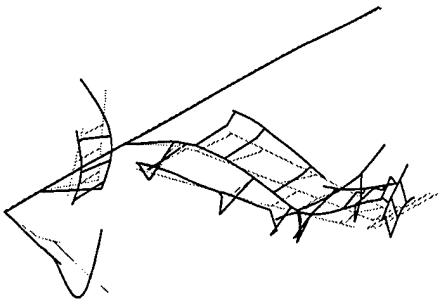

37.46 Hz

o.) Wing Second Fore/Aft Bending

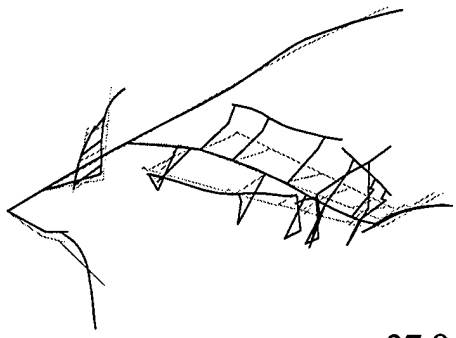

37.94 Hz

p.) Leading Edge Flap Rotation

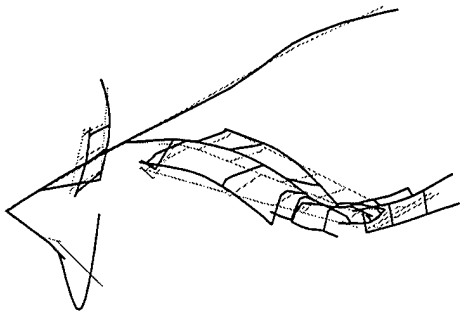

42.93 Hz

q.) Wing Third Bending

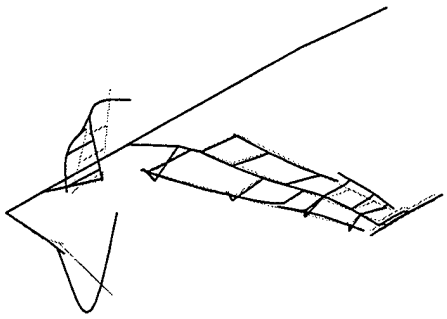

45.78 Hz

r.) Stabilator Second Bending

Figure 5 (continued)

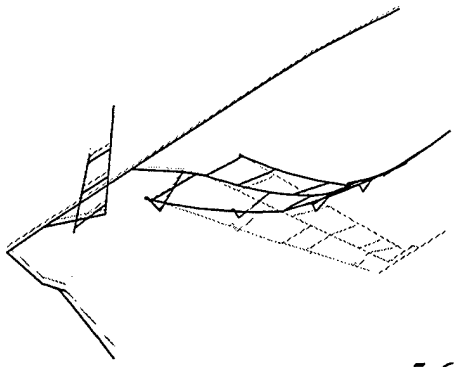

5.65 Hz

a.) Wing First Bending

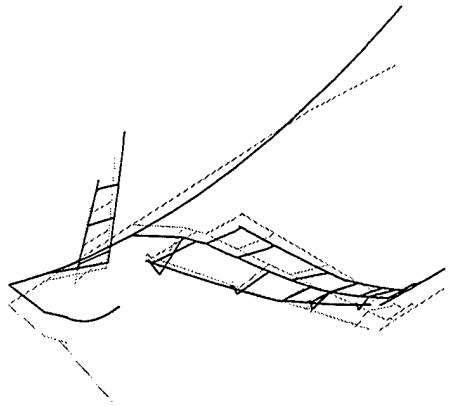

9.28 Hz

b.) Fuselage First Bending

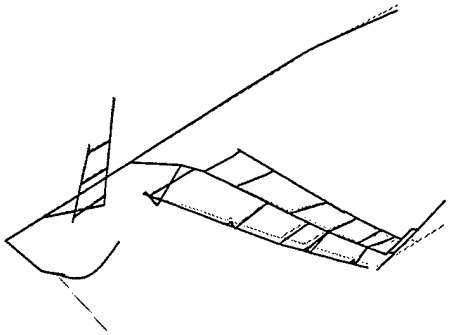

13.55 Hz

c.) Stabilator First Bending

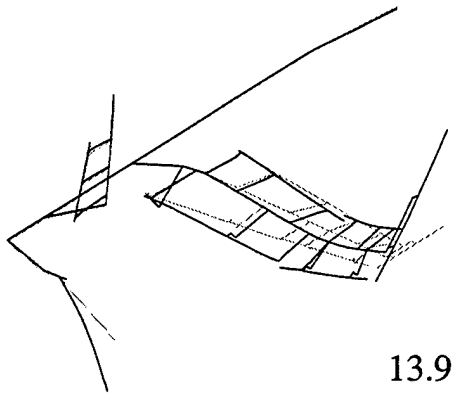

13.98 Hz

d.) Wing First Torsion

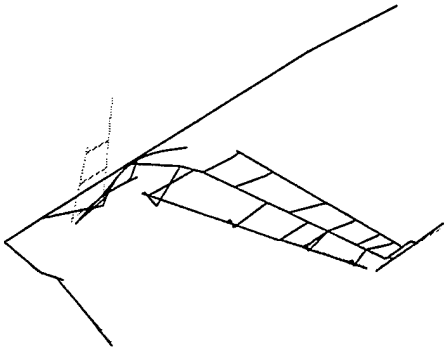

16.19 Hz

e.) Vertical Tail First Bending

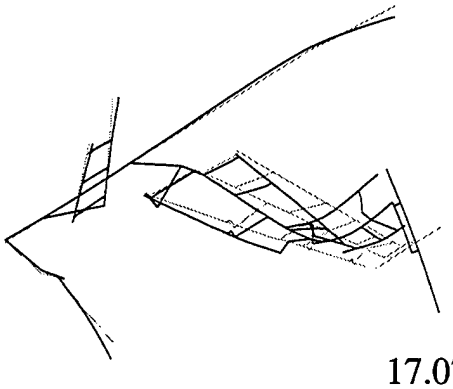

17.07 Hz

f.) Wing Second Bending

Figure 6: Mode Shapes and Frequencies of F/A-18 Aircraft without a Tip Missile for Symmetric Boundary Conditions

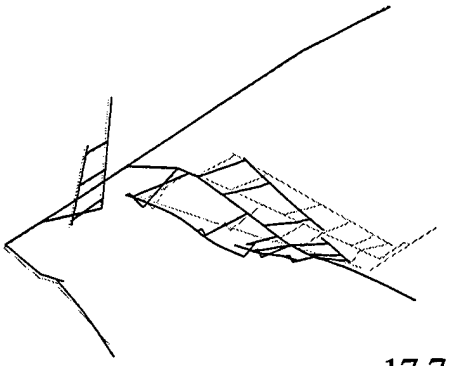

17.71 Hz

g.) Wing First Fore/Aft Bending

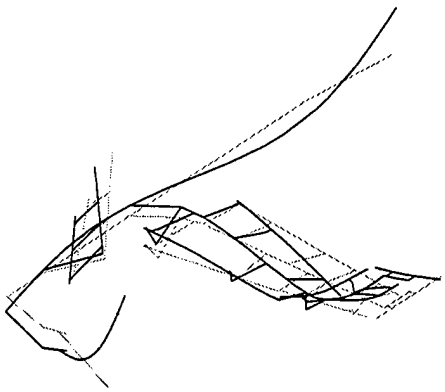

19.68 Hz

h.) Fuselage Second Bending

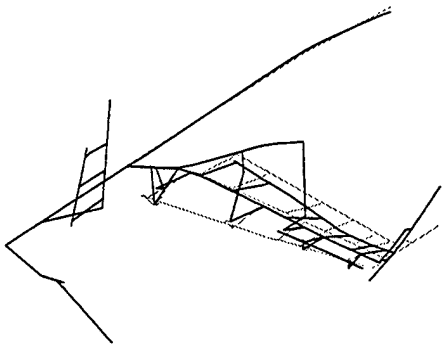

23.33 Hz

i.) Trailing Edge Flap Rotation

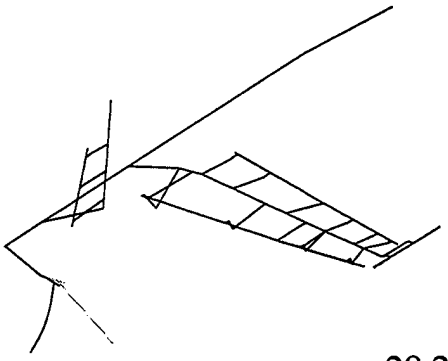

28.23 Hz

j.) Stabilator First Fore/Aft Bending

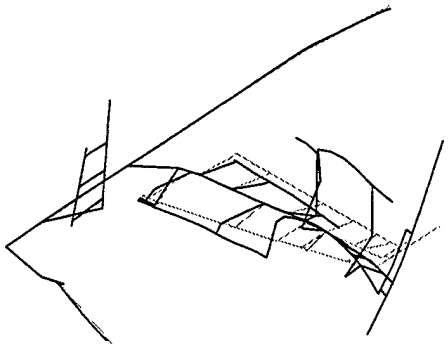

29.41 Hz

k.) Wing Second Torsion

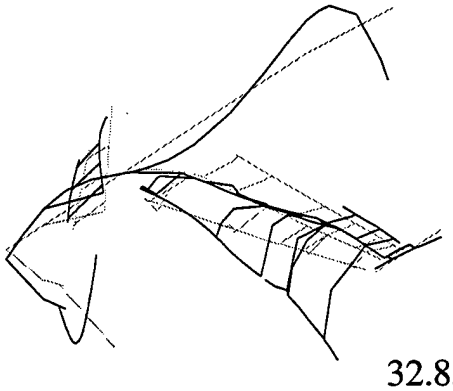

32.85 Hz

l.) Fuselage Third Bending

Figure 6 (Continued)

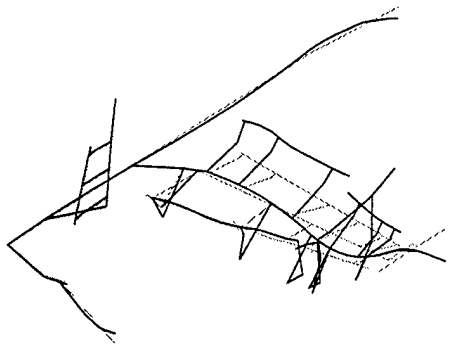

38.09 Hz

m.) Leading Edge Flap Rotation

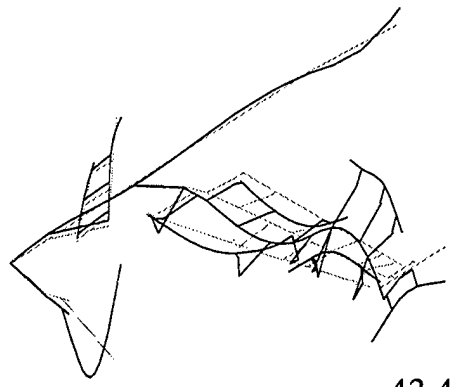

43.49 Hz

n.) Wing Third Bending

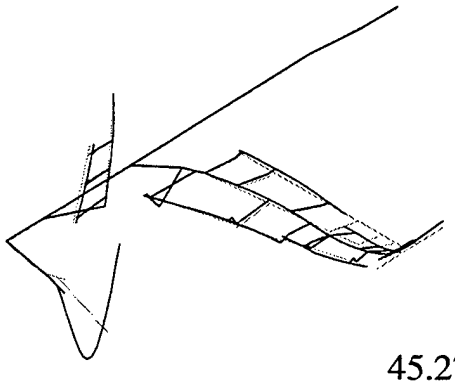

45.27 Hz

o.) Stabilator Second Bending

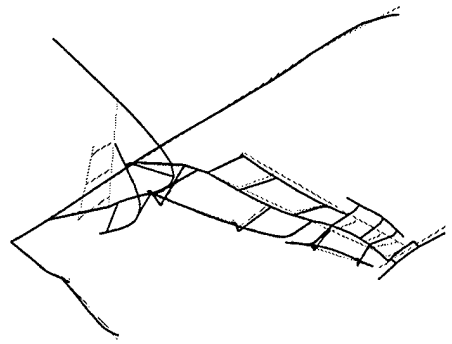

46.95 Hz

p.) Vertical Tail Second Bending

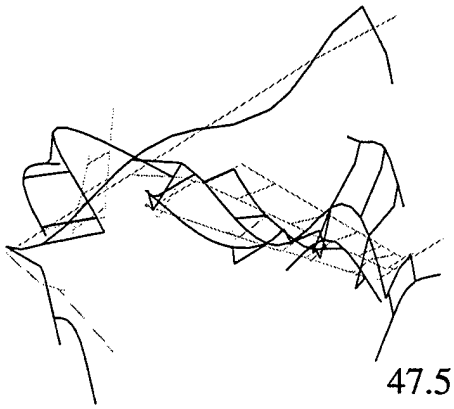

47.58 Hz

q.) Fuselage Fourth Bending

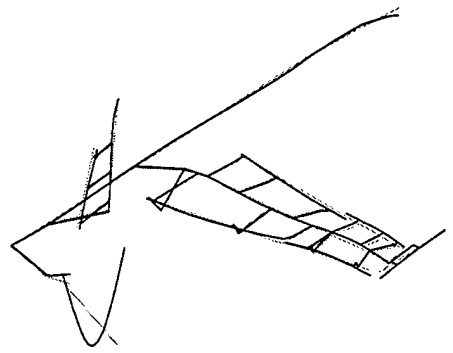

48.90 Hz

r.) Stabilator First Torsion

Figure 6 (Continued)

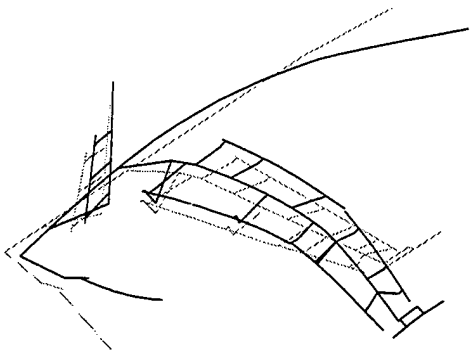

8.12 Hz

a.) Fuselage First Bending

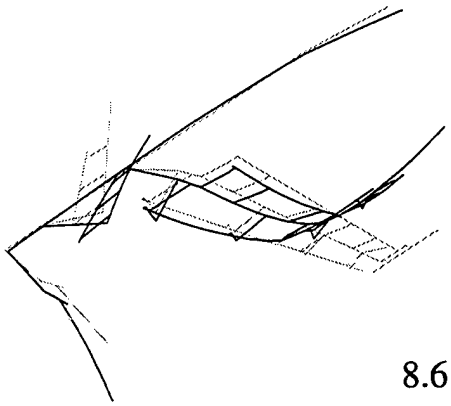

8.61 Hz

b.) Wing First Bending

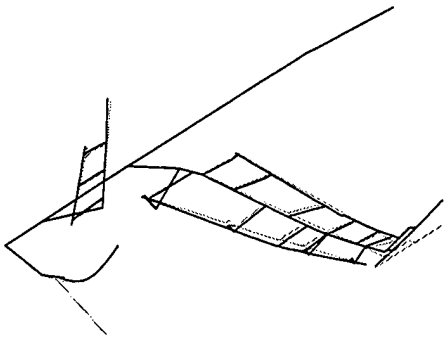

13.32 Hz

c.) Stabilator First Bending

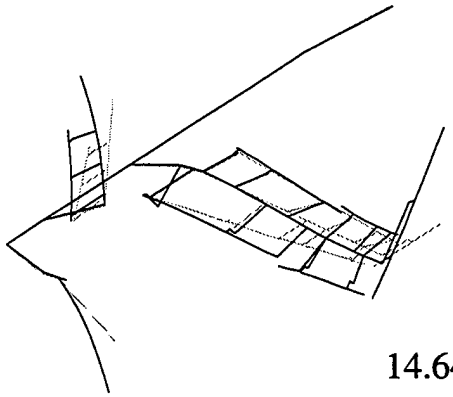

14.64 Hz

d.) Wing First Torsion

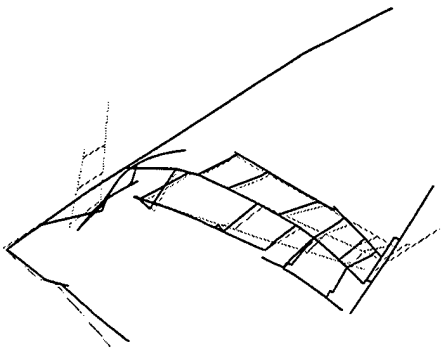

15.57 Hz

e.) Vertical Tail First Bending

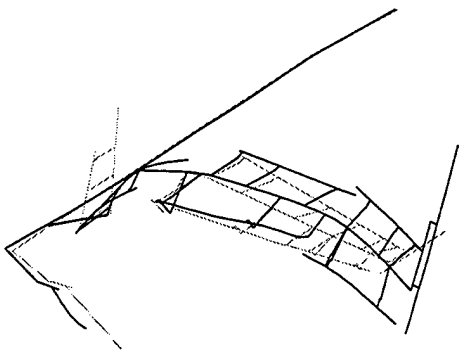

16.68 Hz

f.) Wing First Fore/Aft Bending

Figure 7: Mode Shapes and Frequencies of F/A-18 Aircraft without a Tip Missile for Anti-Symmetric Mode Shapes

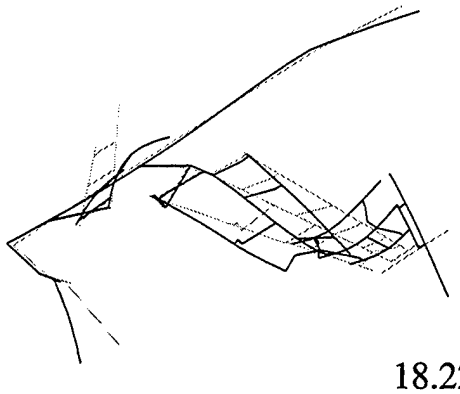

18.22 Hz

g.) Wing Second Bending

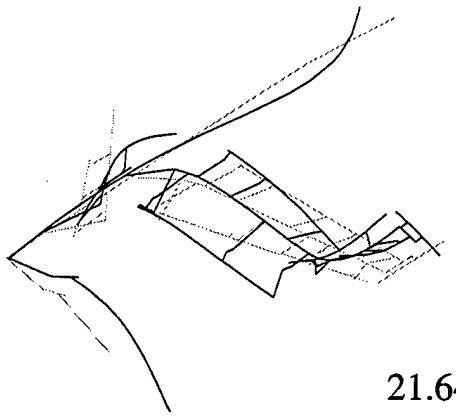

21.64 Hz

h.) Fuselage Second Bending

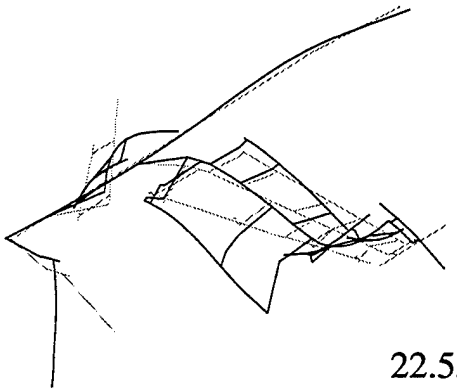

22.55 Hz

i.) Fuselage First Torsion

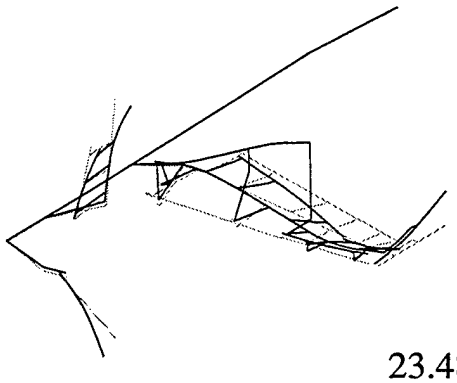

23.48 Hz

j.) Trailing Edge Flap Rotation

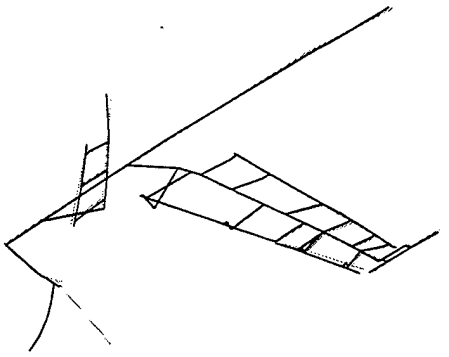

28.48 Hz

k.) Stabilator First Fore/Aft Bending

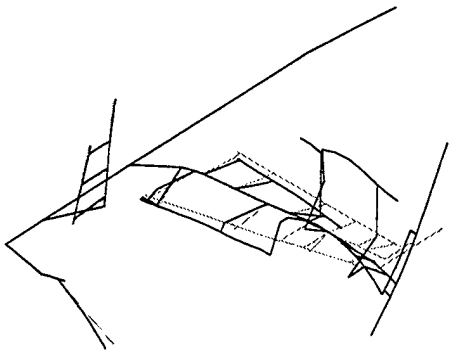

29.44 Hz

l.) Wing Second Torsion

Figure 7 (Continued)

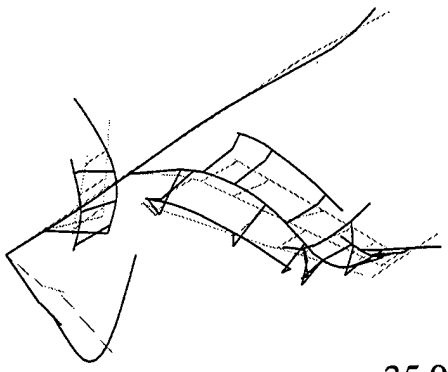

35.96 Hz

m.) Fuselage Third Bending

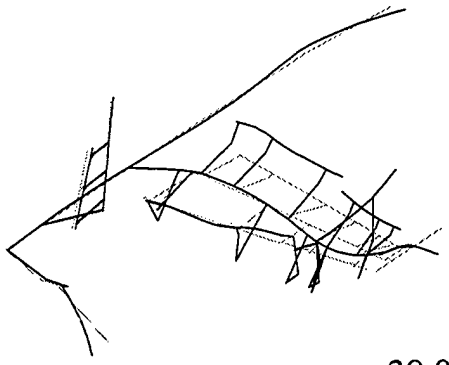

38.00 Hz

n.) Leading Edge Flap Rotation

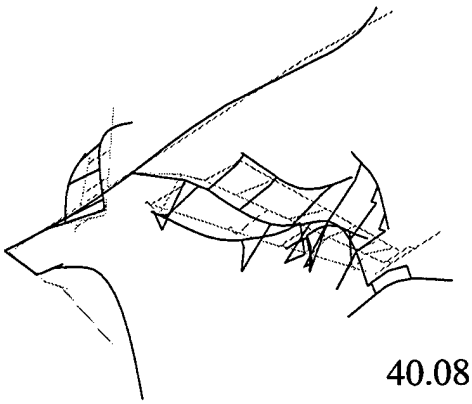

40.08 Hz

o.) Wing Third Bending

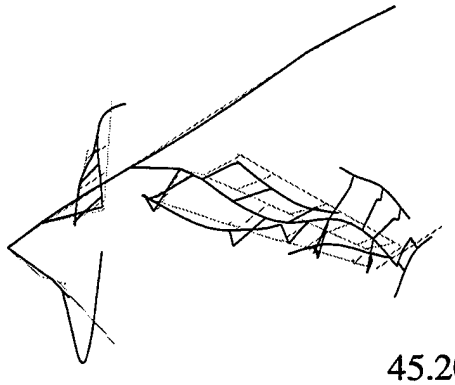

45.20 Hz

p.) Outboard Wing Torsion

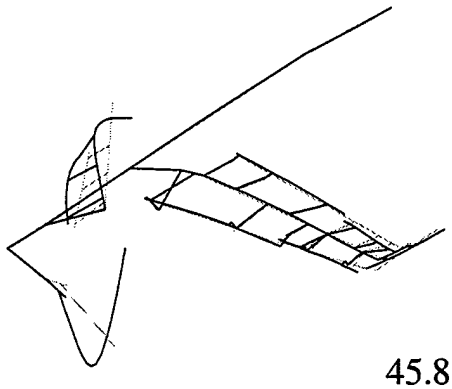

45.81 Hz

q.) Stabilator Second Bending

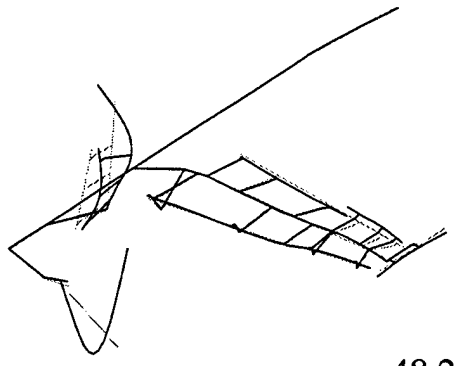

48.24 Hz

r.) Stabilator First Torsion

Figure 7 (Continued)

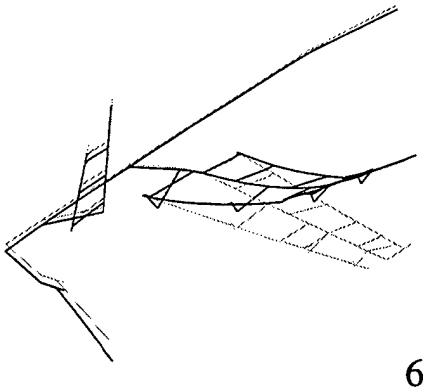

6.67 Hz

a.) Wing First Bending

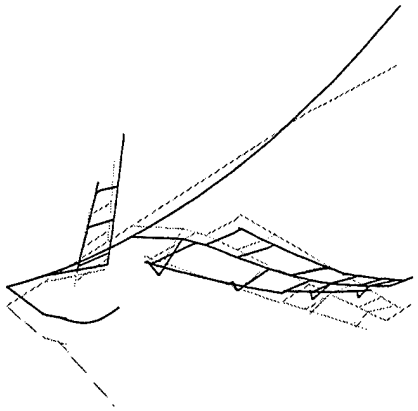

9.35 Hz

b.) Fuselage First Bending

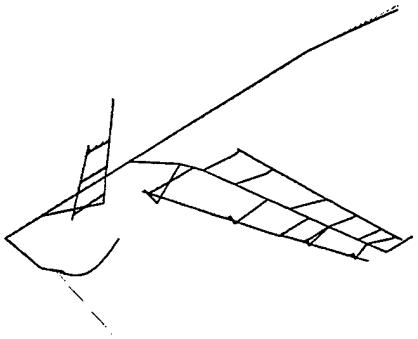

13.60 Hz

c.) Stabilator First Bending

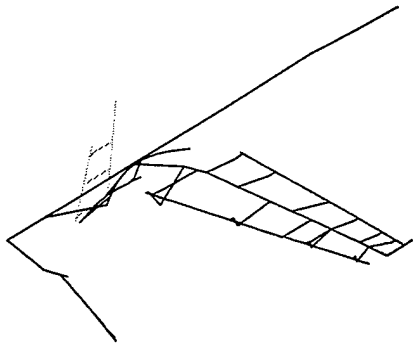

16.19 Hz

d.) Vertical Tail First Bending

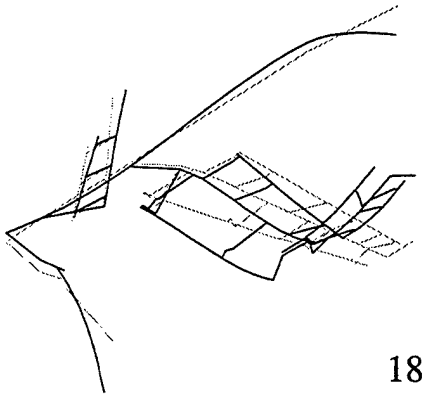

18.20 Hz

e.) Wing Second Bending

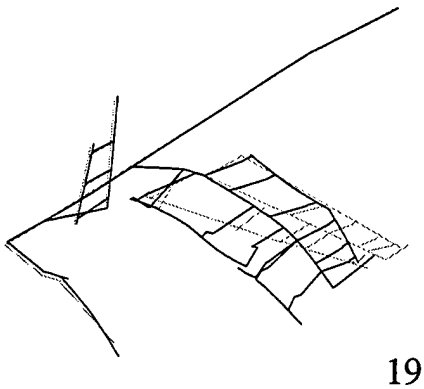

19.69 Hz

f.) Wing First Fore/Aft Bending

Figure 8: Mode Shapes and Frequencies of F/A-18 Aircraft without a Missile Launcher for Symmetric Mode Shapes

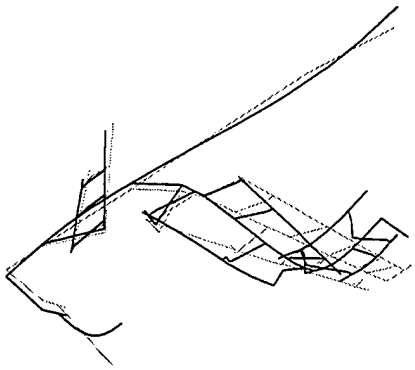

20.42 Hz

g.) Fuselage Second Bending

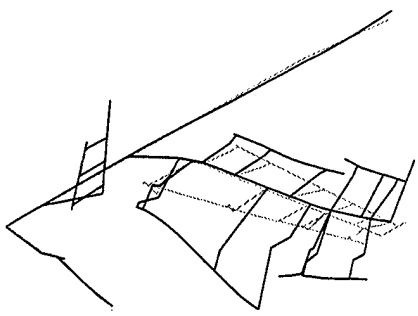

22.05 Hz

h.) Wing First Torsion

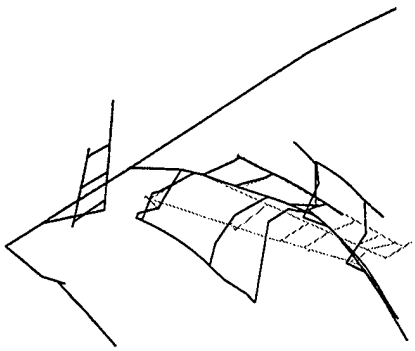

26.25 Hz

i.) Trailing Edge Flap Rotation

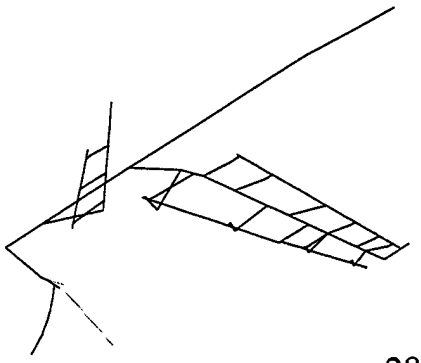

28.23 Hz

j.) Stabilator First Fore/Aft Bending

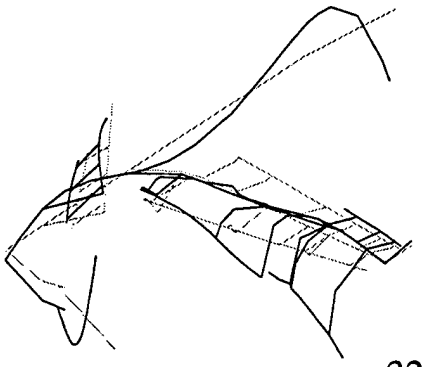

32.85 Hz

k.) Fuselage Third Bending

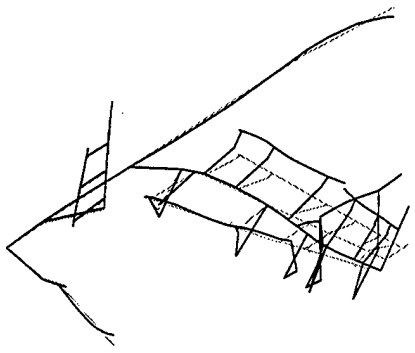

37.37 Hz

l.) Leading Edge Flap Rotation

Figure 8 (Continued)

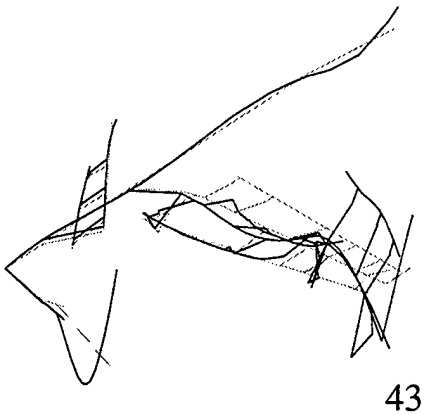

43.81 Hz

m.) Wing Third Bending

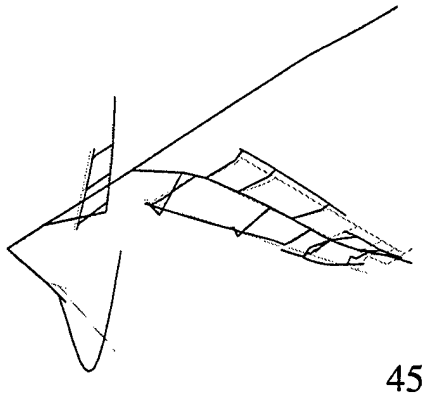

45.16 Hz

n.) Stabilator Second Bending

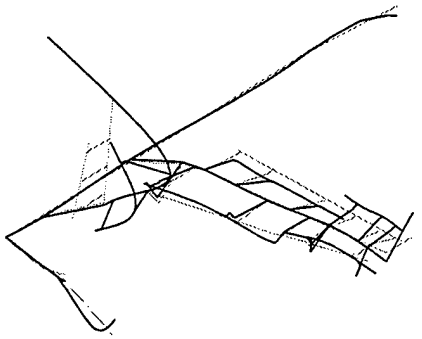

46.90 Hz

o.) Vertical Tail Second Bending

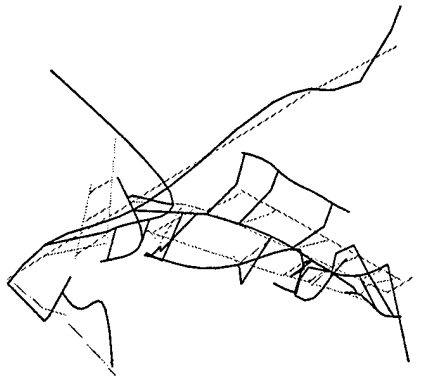

47.73 Hz

p.) Fuselage Fourth Bending

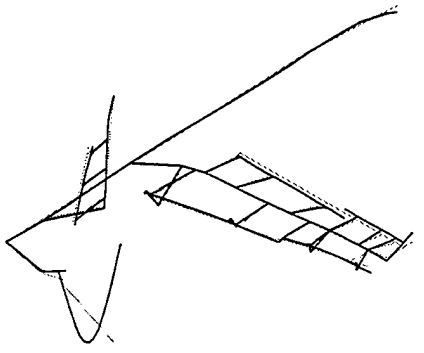

48.92 Hz

q.) Stabilator First Torsion

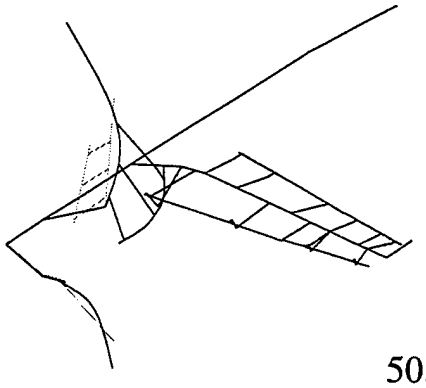

50.02 Hz

r.) Vertical Tail First Torsion

Figure 8 (Continued)

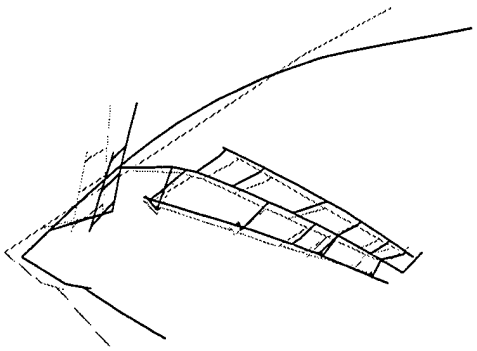

8.26 Hz

a.) Fuselage First Bending

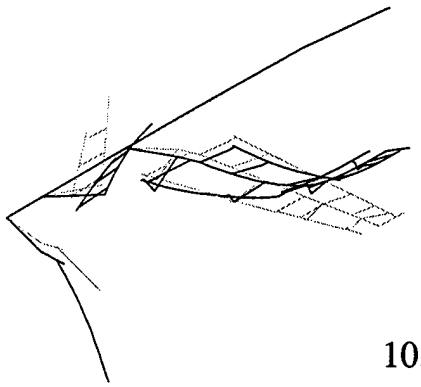

10.12 Hz

b.) Wing First Bending

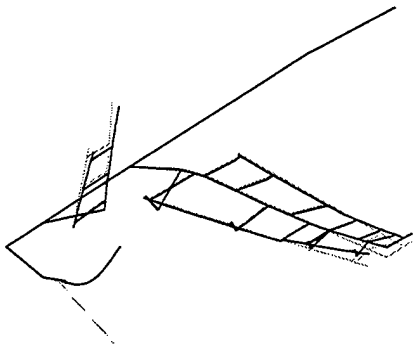

13.68 Hz

c.) Stabilator First Bending

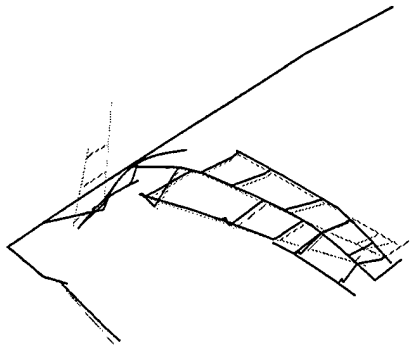

16.00 Hz

d.) Vertical Tail First Bending

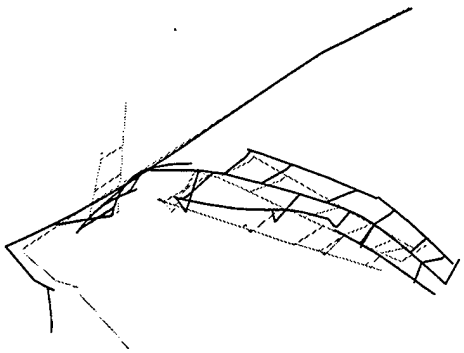

17.56 Hz

e.) Wing First Fore/Aft Bending

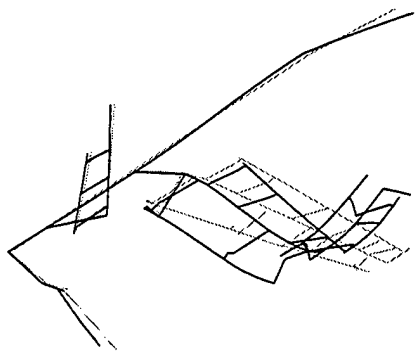

18.68 Hz

f.) Wing Second Bending

Figure 9: Mode Shapes and Frequencies of F/A-18 Aircraft without a Missile Launcher for Anti-Symmetric Mode Shapes

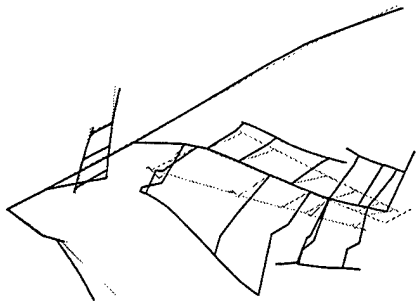

21.94 Hz

g.) Wing First Torsion

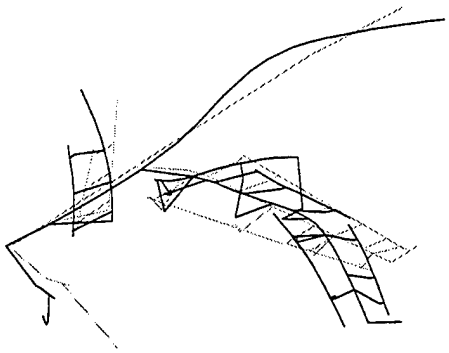

22.14 Hz

h.) Fuselage Second Bending

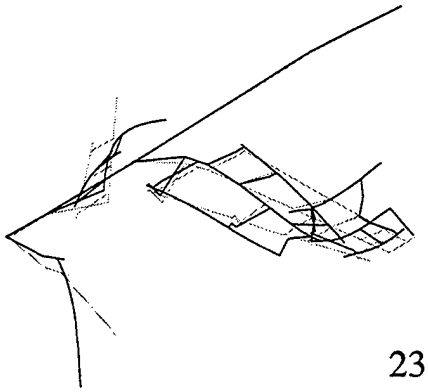

23.40 Hz

i.) Fuselage First Torsion

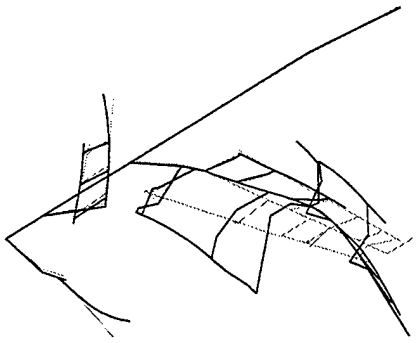

26.32 Hz

j.) Trailing Edge Flap Rotation

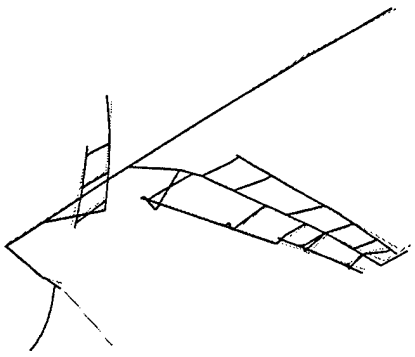

28.56 Hz

k.) Stabilator First Fore/Aft Bending

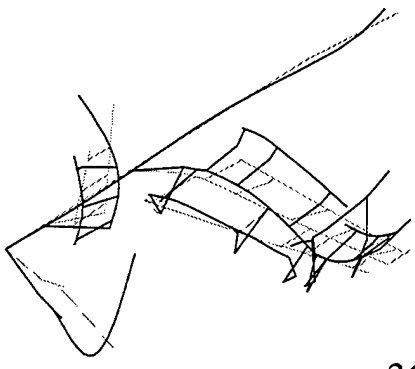

36.27 Hz

l.) Fuselage Third Bending

Figure 9 (Continued)

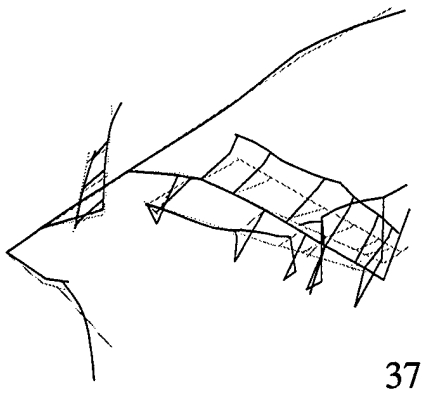

37.34 Hz

m.) Leading Edge Flap Rotation

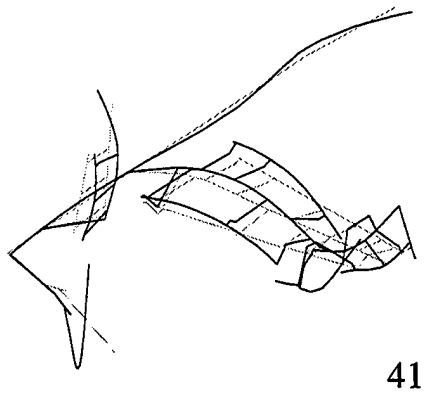

41.10 Hz

n.) Wing Third Bending

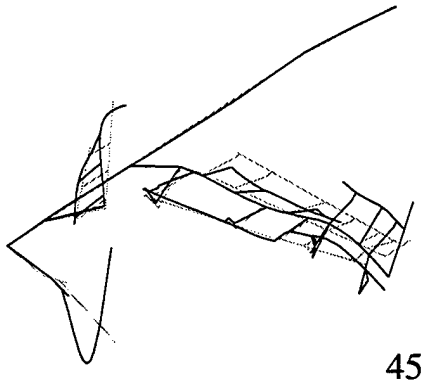

45.27 Hz

o.) Wing Second Torsion

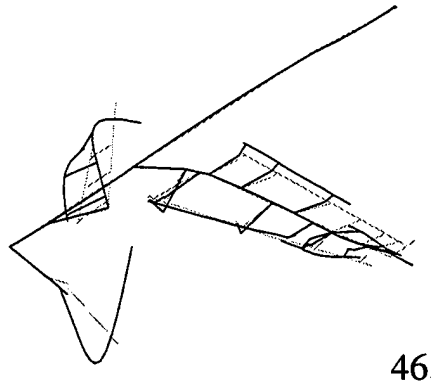

46.08 Hz

p.) Stabilator Second Bending

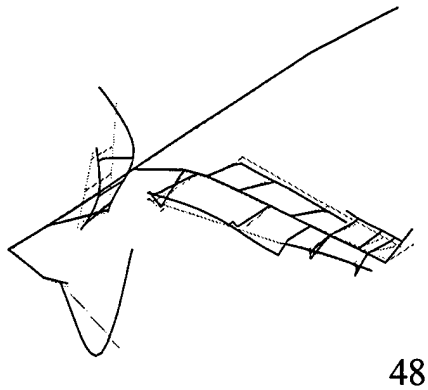

48.14 Hz

q.) Stabilator First Torsion

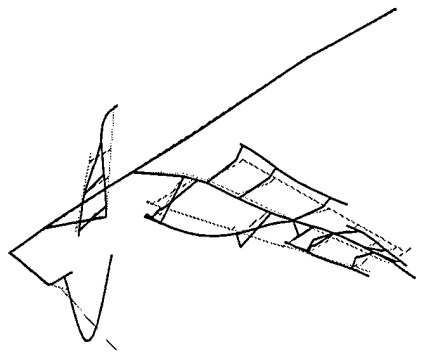

48.80 Hz

r.)

Figure 9 (Continued)

SECTION V

DYNAMIC AEROELASTIC ANALYSIS

With the inclusion of aerodynamics, the equations of motion for the system are:

$$[M]\{\ddot{x}\} + [K]\{x\} = [A]\{x\} \tag{5}$$

where $[M]$ is the mass matrix, $[K]$ is the stiffness matrix, $[A]$ is the aerodynamic stiffness matrix, $\{\ddot{x}\}$ is the vector of nodal accelerations, and $\{x\}$ is the vector of nodal displacements. The equation is reduced to an eigenvalue problem by assuming harmonic motion, which is effected by substituting $\{x\} = \{u\}e^{i\omega t}$:

$$\left[-[A] + [K] - \omega^2[M]\right]\{u\} = \{0\} \tag{6}$$

where ω is the natural frequency, and $\{u\}$ is the mode shape. The equations of motion are solved in ASTROS to determine flutter utilizing the *p-k* method.

p-k Flutter Solution

The aerodynamic stiffness matrix is a function of Mach number and reduced frequency. The aerodynamic stiffness matrix is assumed harmonic and therefore composed of real and imaginary parts:

$$[A] = \frac{1}{2}\rho V^2\left(\left[Q^r\right] + i\left[Q^i\right]\right) \tag{7}$$

In order to solve the equations of motion for flutter, assumptions are made about the motion and damping near the flutter point. The motion is assumed to be of the general, non-harmonic form, e^{pt}, where p is a complex number. This assumption is only possible if the damping is small, since the aerodynamic coefficients were generated with the constant amplitude harmonic motion. The following definitions are made to construct the algorithm for the solution to the flutter problem.

$$p = \gamma k + ik \tag{8}$$

$$k = \frac{\omega b}{V} \tag{9}$$

where k is the reduced frequency. The assumption that γ is small, generally either zero or two percent, allows the following relations:

$$i \cong \frac{p}{k} \tag{10}$$

$$\omega = \frac{kV}{b} \cong \frac{pV}{ib} \tag{11}$$

These relations are substituted into the equations of motion to produce the general flutter equation:

$$\left[-\frac{1}{2}\rho V^2\left(\left[Q^r\right] + \frac{p}{k}\left[Q^i\right]\right) + \left[K\right] + \left(\frac{V}{b}\right)^2 p^2\left[M\right]\right]\{u\} = \{0\} \tag{12}$$

The determinant of this equation provides a way to solve for the value of p:

$$\left| \left(\frac{V}{b}\right)^2 p^2\left[M\right] + \left(-\frac{1}{2}\frac{\rho V^2}{k}\right)p\left[Q^i\right] + \left(\left[K\right] - \frac{1}{2}\rho V^2\left[Q^r\right]\right) \right| = 0 \tag{13}$$

The flutter solution algorithm requires the selection of a velocity and iterative solution for p from the complex eigenvalue problem resulting from the equations of motion. The correct value for p for the selected velocity is considered converged when the imaginary part of p is equal to the reduced velocity utilized to create the aerodynamic stiffness matrix. The velocity for which the real part of p equals the assumed damping, γ equals zero or two percent, is the flutter velocity.

Beam/Rod Model Flutter Analysis

The dynamic aeroelastic analysis of the F/A-18 SRA aircraft has been conducted for the model under symmetric boundary conditions. The launcher configurations with a tip missile and without a tip missile were examined for flutter.

The aerodynamic planform of the wing extends to the center line of the aircraft. The aerodynamic panels, as shown in Figure 10, are modeled with 12 chordwise and 22 spanwise boxes. The first three rows of spanwise boxes from the centerline to the 42.15 in. span station represent the central fuselage.

All control surface aerodynamic panels are splined to the individual beams representing the control surface structures. The aerodynamic panels of the missile launcher are dependent upon the width of each configuration. The width of the configuration without a tip missle is modeled by two panels (6.4" wide), whereas the configuration with a tip missile is modeled by four panels (12.4"). The aerodynamic paneling of the configuration with a tip missile is shown in Figure 11. The control surfaces are outlined with respect to the aerodynamic panels and are noted as follows: leading edge inboard flap (LEIF), leading edge outboard flap (LEOF), trailing edge flap (TEF), and aileron (AIL).

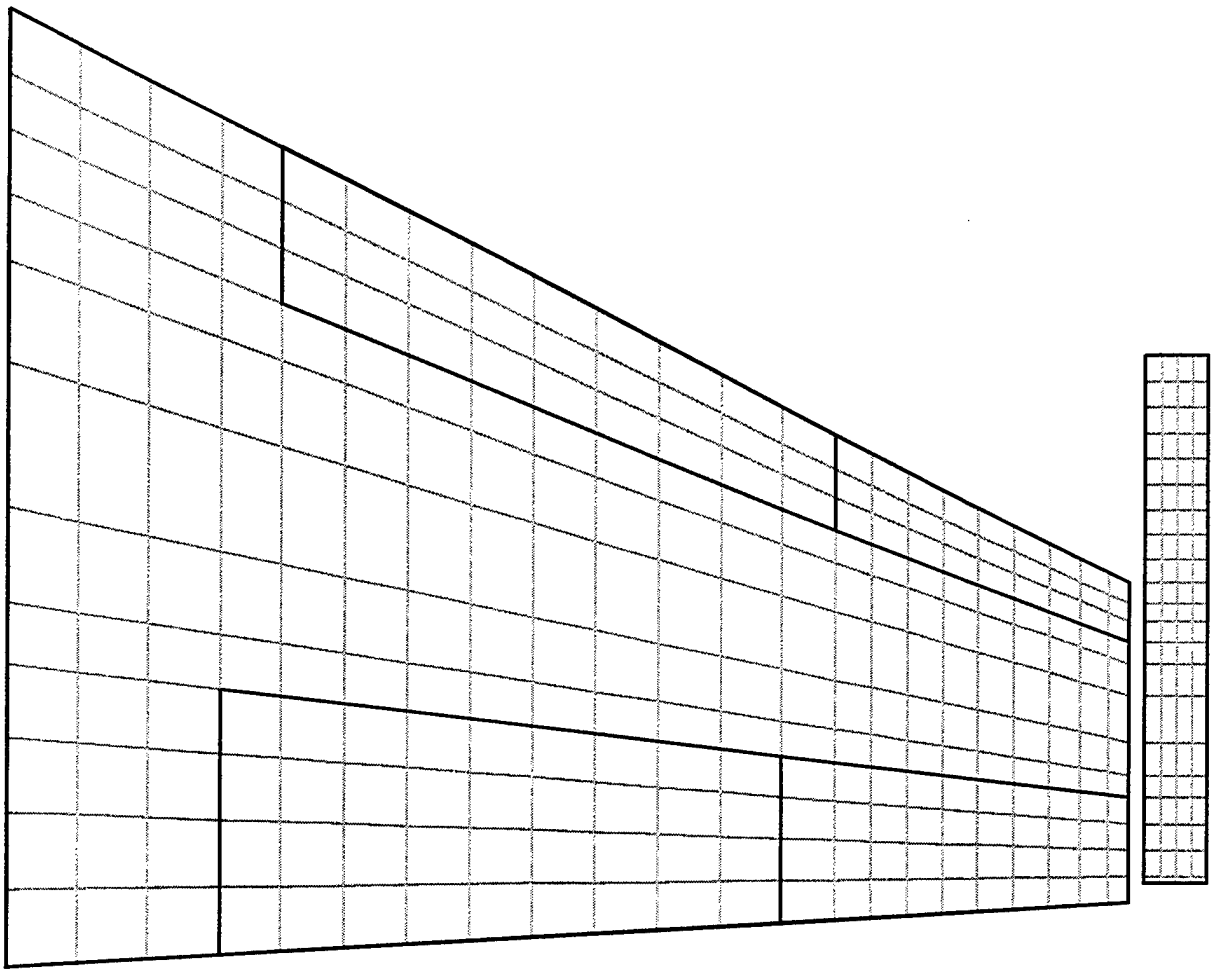

Figure 10: Aerodynamic Panel Representation for Wing and Launcher

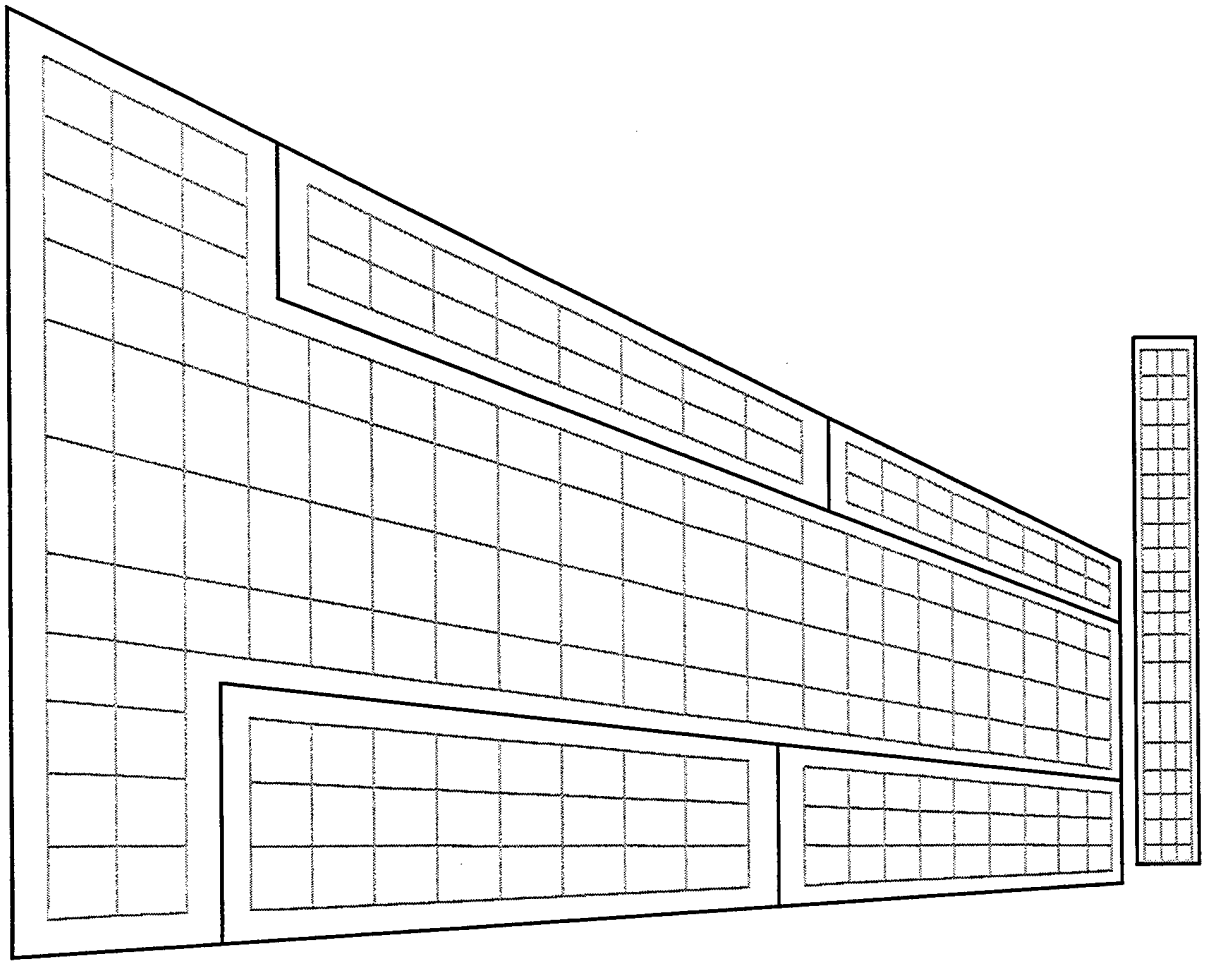

Figure 11: Division of Aerodynamic Panels for the Wing, Leading Edge In-board and Out-board Flap, Trailing Edge Out-board Flap, Aileron and Missile Launcher

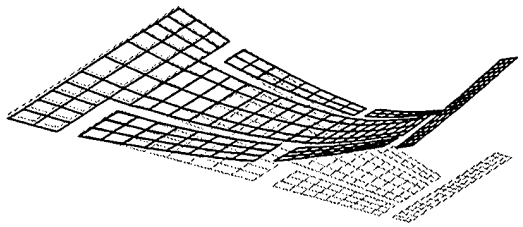

4.44 Hz

a.) Wing First Bending

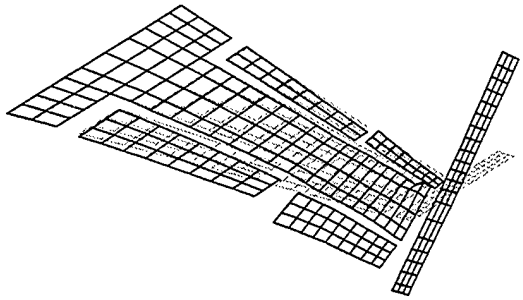

8.59 Hz

b.) Wing First Torsion

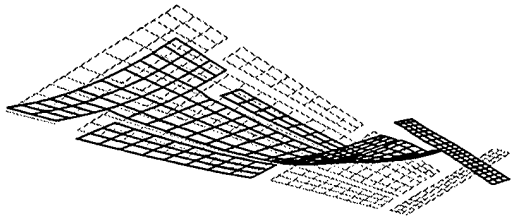

9.24 Hz

c.) Fuselage First Bending

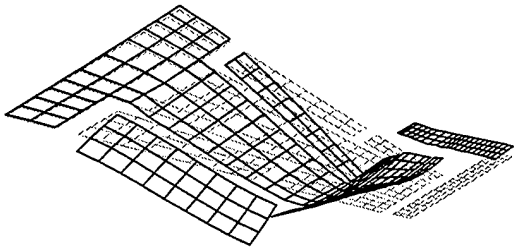

14.56 Hz

d.) Wing Second Bending

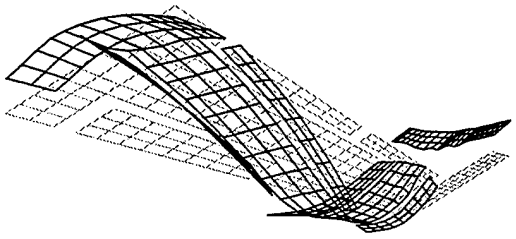

19.55 Hz

e.) Fuselage Second Bending

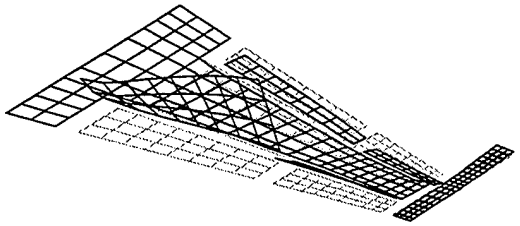

23.04 Hz

f.) Trailing Edge Flap Rotation

Figure 12: Splined Aerodynamic Mode Shapes and Frequencies of the F/A-18 Wing with a Tip Missile for Symmetric Boundary Conditions

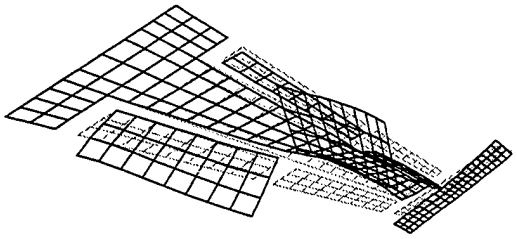

27.24 Hz

g.) Wing Second Torsion

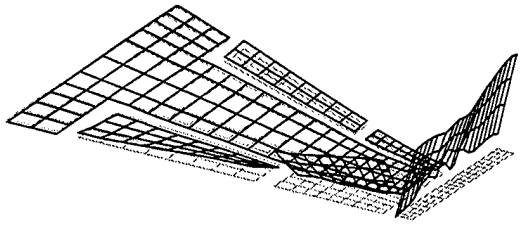

32.73 Hz

h.) Tip Missile Bending

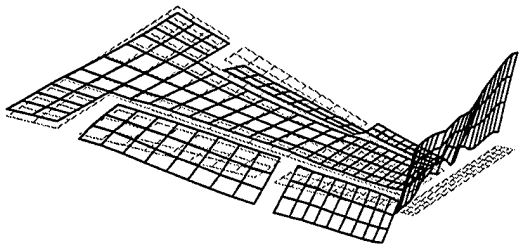

32.90 Hz

i.) Fuselage Third Bending

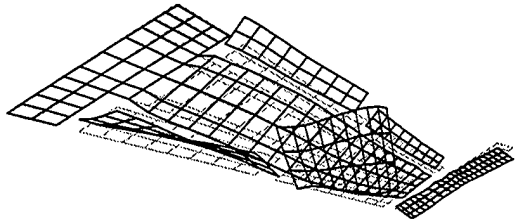

37.64 Hz

j.) Leading Edge Flap Rotation

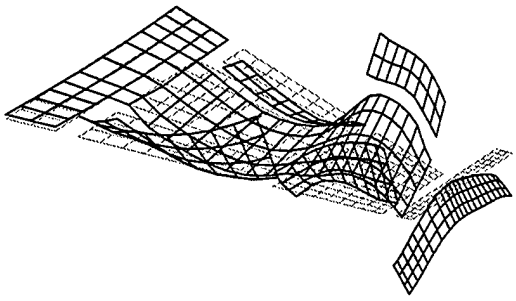

42.89 Hz

k.) Wing Third Bending

Figure 12 (continued)

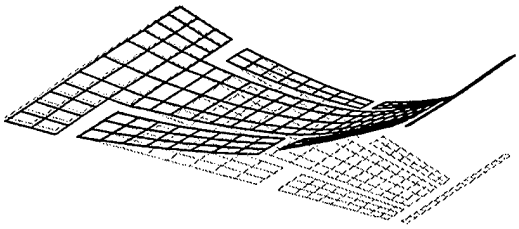

5.65 Hz

a.) Wing First Bending

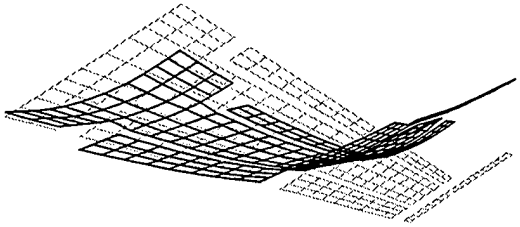

9.28 Hz

b.) Fuselage First Bending

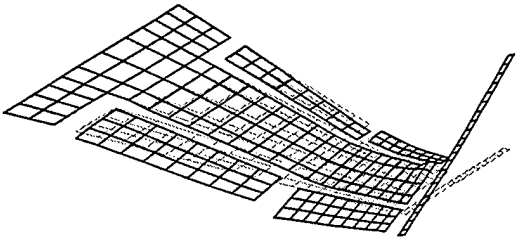

13.98 Hz

c.) Wing First Torsion

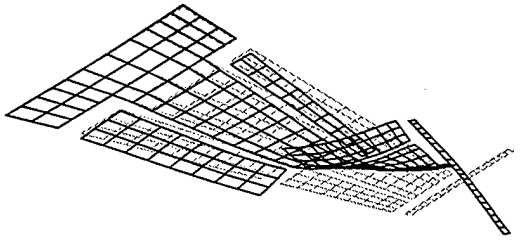

17.07 Hz

d.) Wing Second Bending

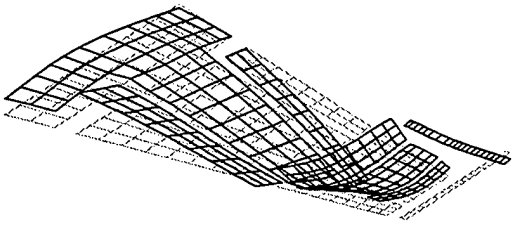

19.68 Hz

e.) Fuselage Second Bending

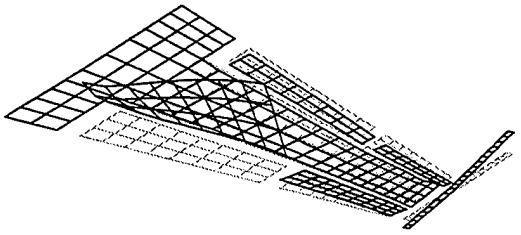

23.33 Hz

f.) Trailing Edge Flap Rotation

Figure 13: Splined Aerodynamic Mode Shapes and Frequencies of F/A-18 Aircraft without a Tip Missile for Symmetric Boundary Conditions

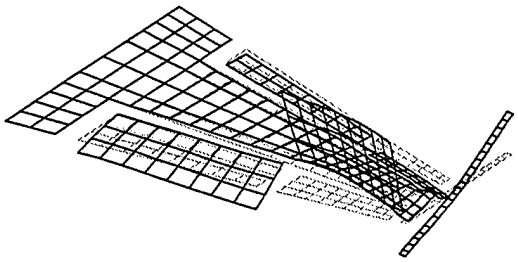

29.41 Hz

g.) Wing Second Torsion

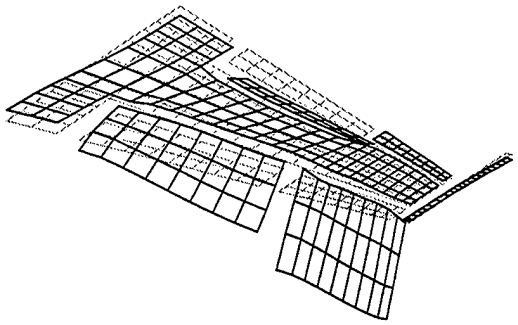

32.85 Hz

h.) Fuselage Third Bending

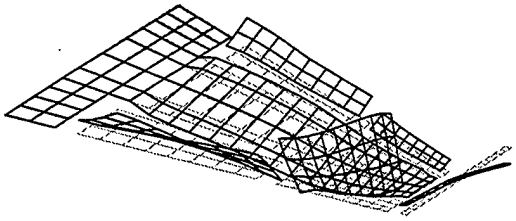

38.09 Hz

i.) Leading Edge Flap Rotation

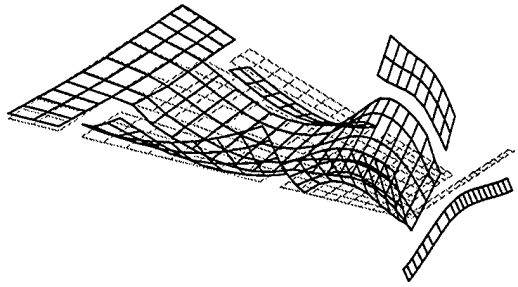

43.49 Hz

j.) Wing Third Bending

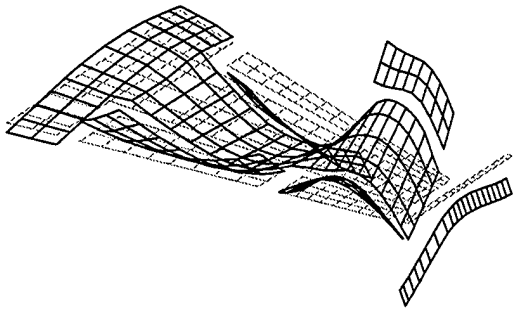

47.58 Hz

k.) Fuselage Fourth Bending

Figure 13 (continued)

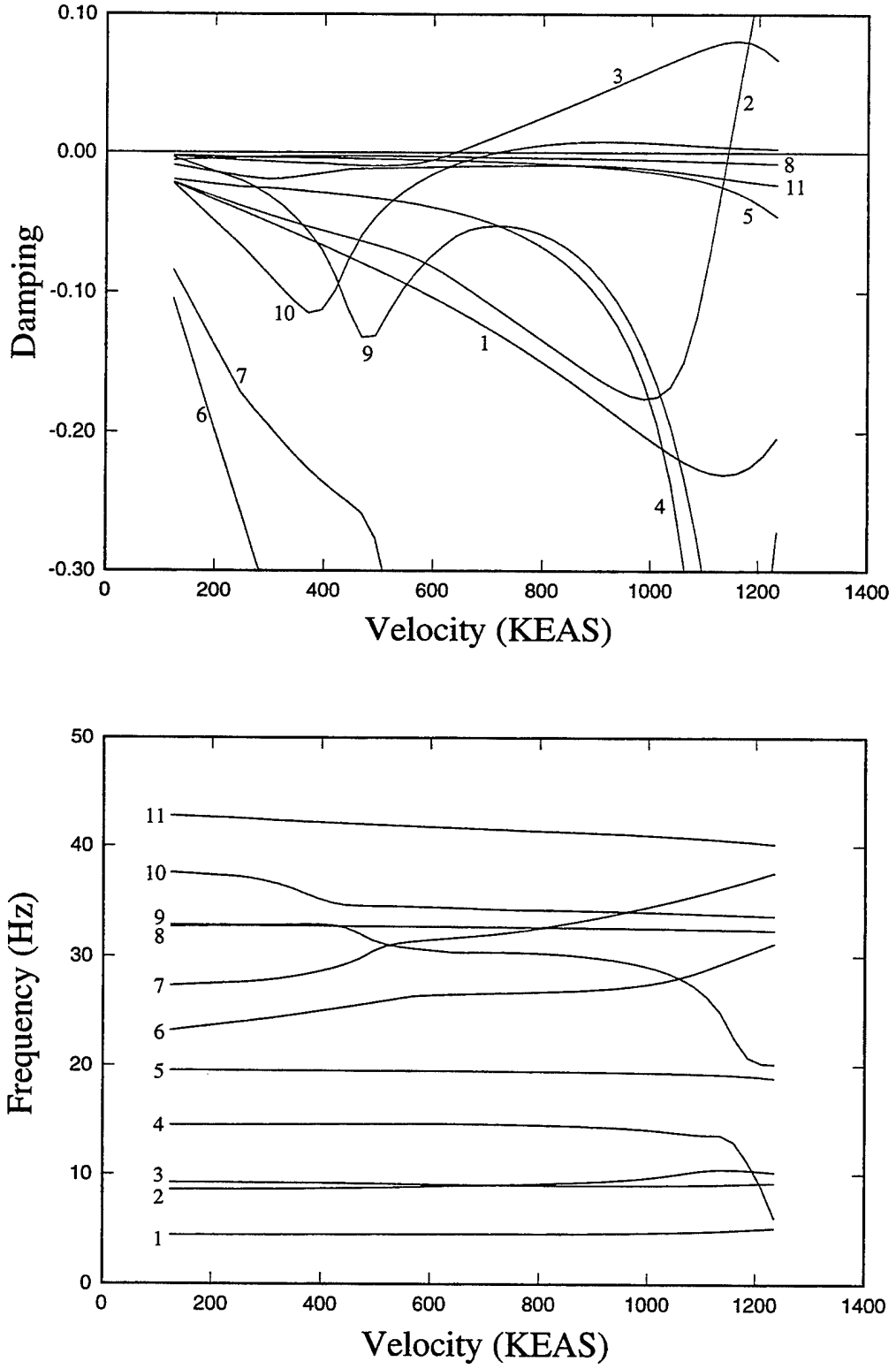

Figure 14: V-g-w Plot of F/A-18 Aircraft with a Tip Missile for Symmetric Boundary Conditions, Mach 0.7, Alt = Sea Level

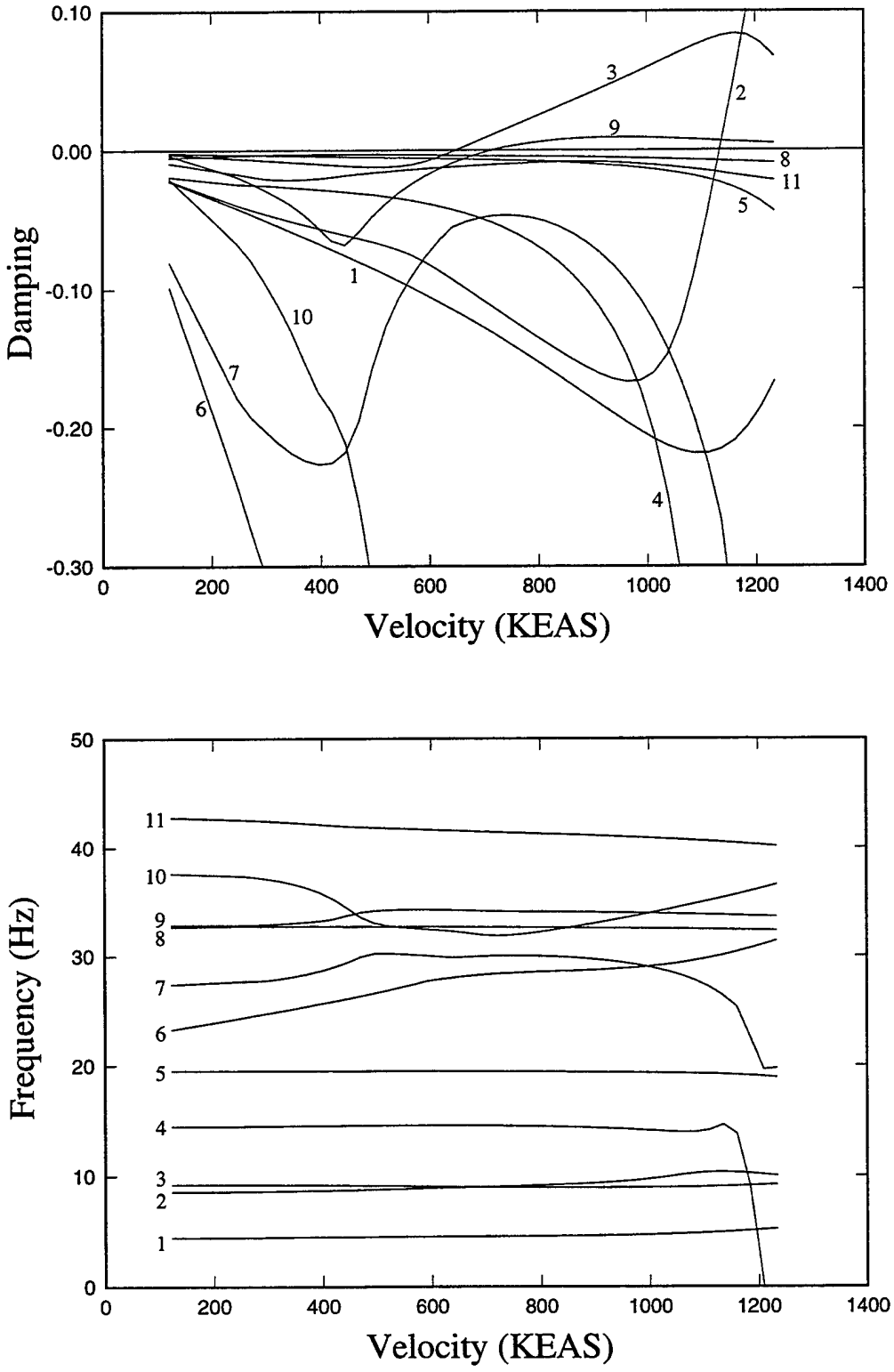

Figure 15: V-g-w Plot of F/A-18 Aircraft with a Tip Missile for Symmetric Boundary Conditions, Mach 0.75, Alt = Sea Level

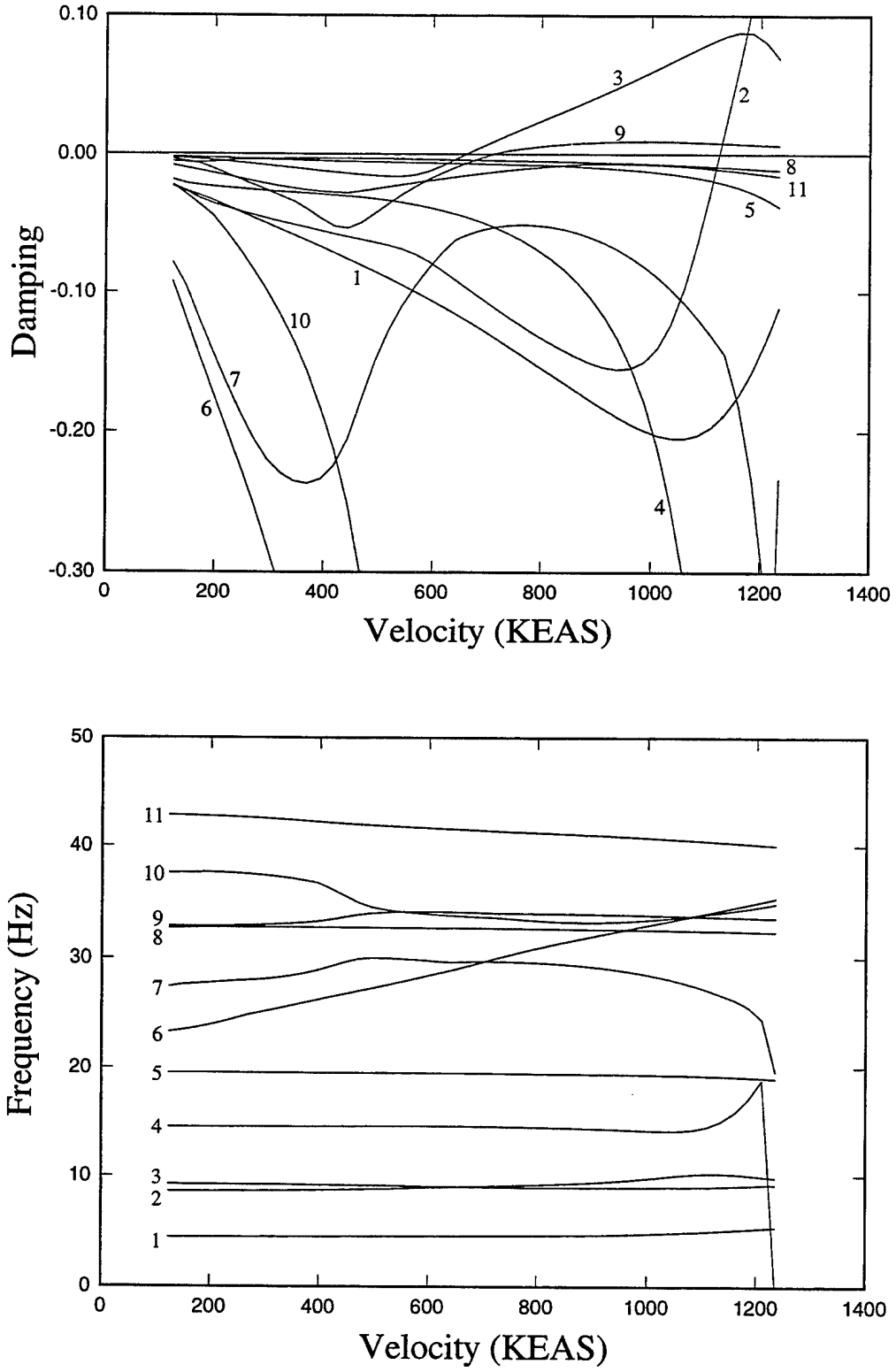

Figure 16: V-g-w Plot of F/A-18 Aircraft with a Tip Missile for Symmetric Boundary Conditions, Mach 0.8, Alt = Sea Level

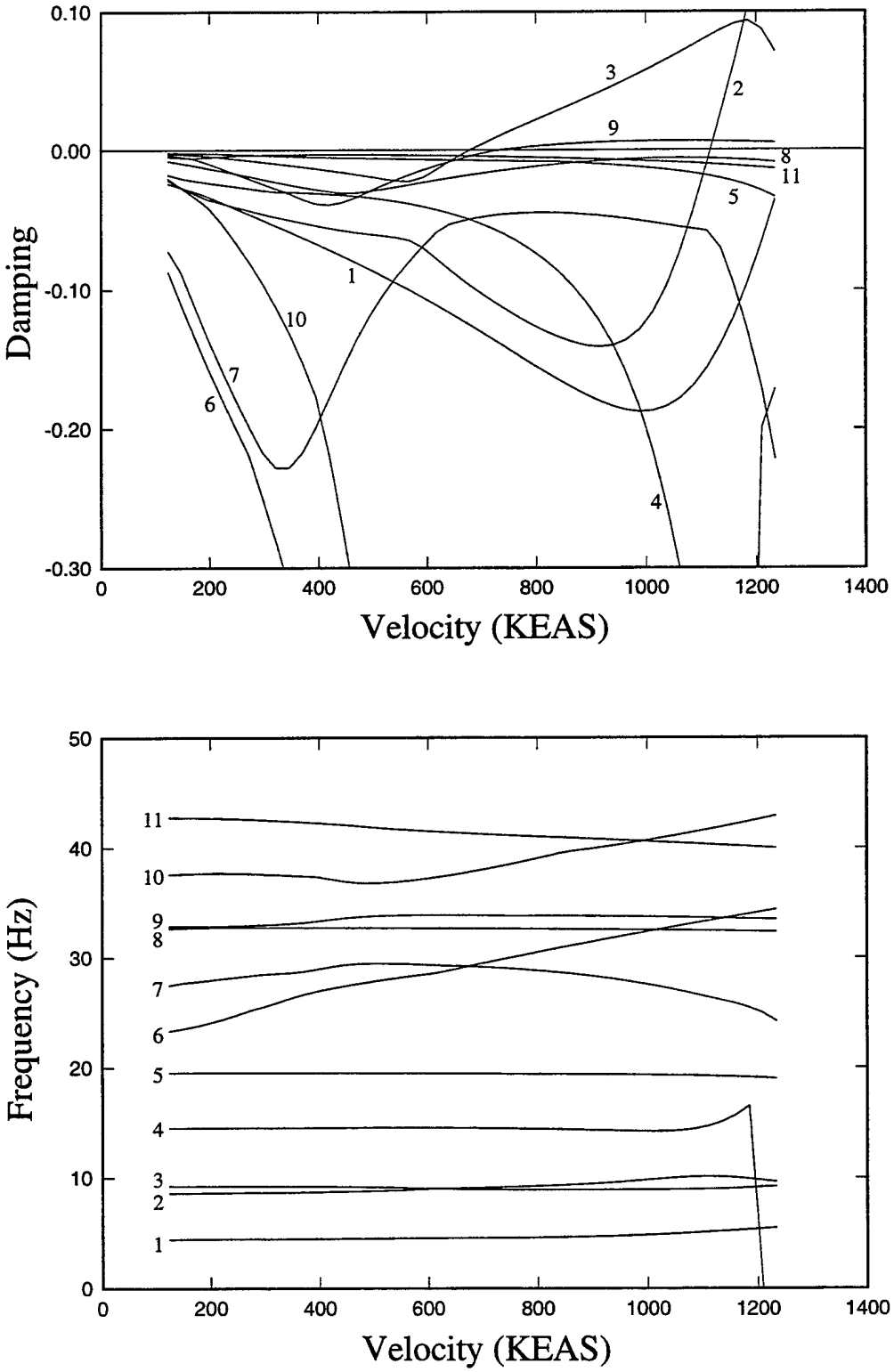

Figure 17: V-g-w Plot of F/A-18 Aircraft with a Tip Missile for Symmetric Boundary Conditions, Mach 0.85, Alt = Sea Level

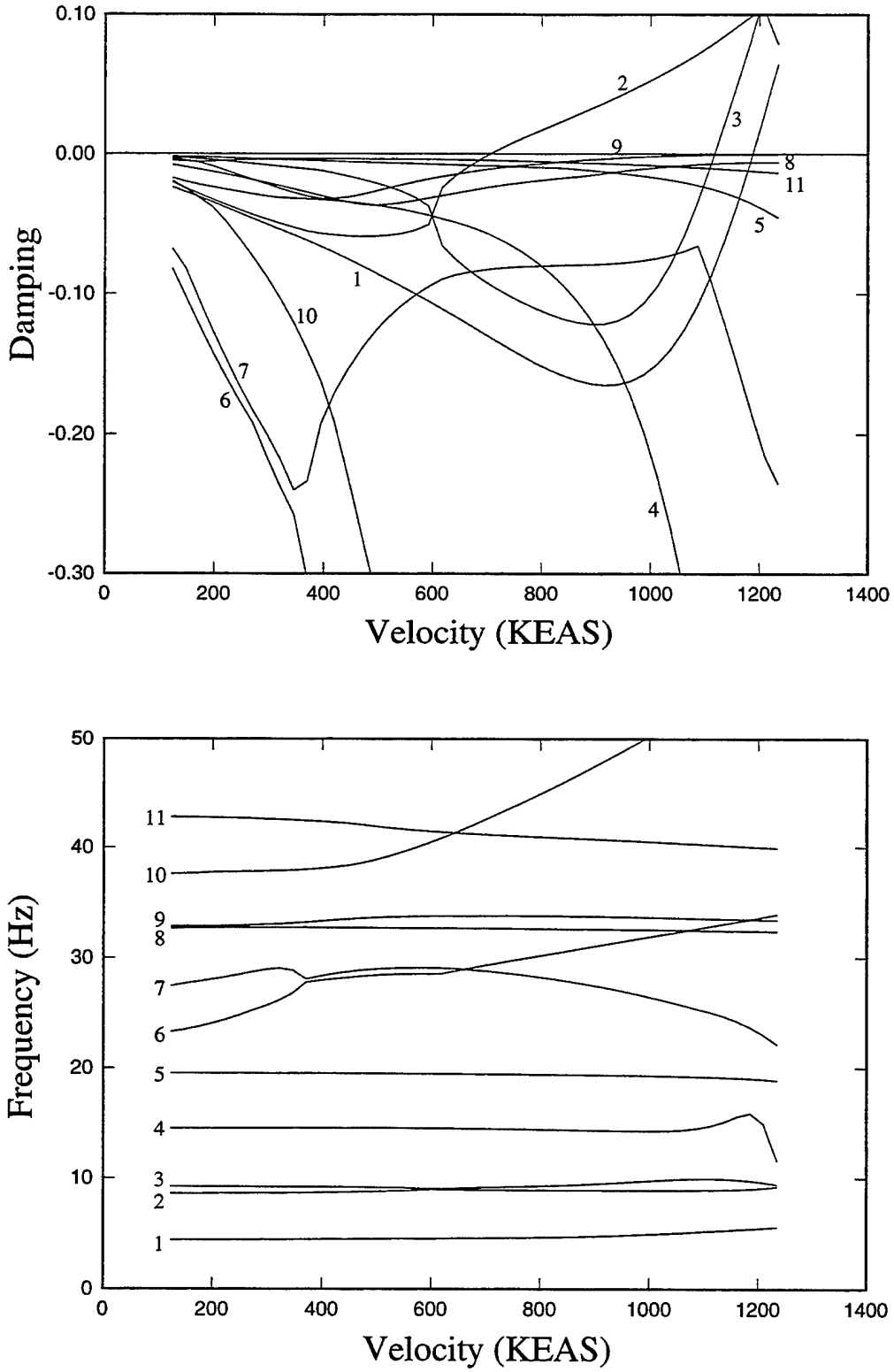

Figure 18: V-g-w Plot of F/A-18 Aircraft with a Tip Missile for Symmetric Boundary Conditions, Mach 0.9, Alt = Sea Level

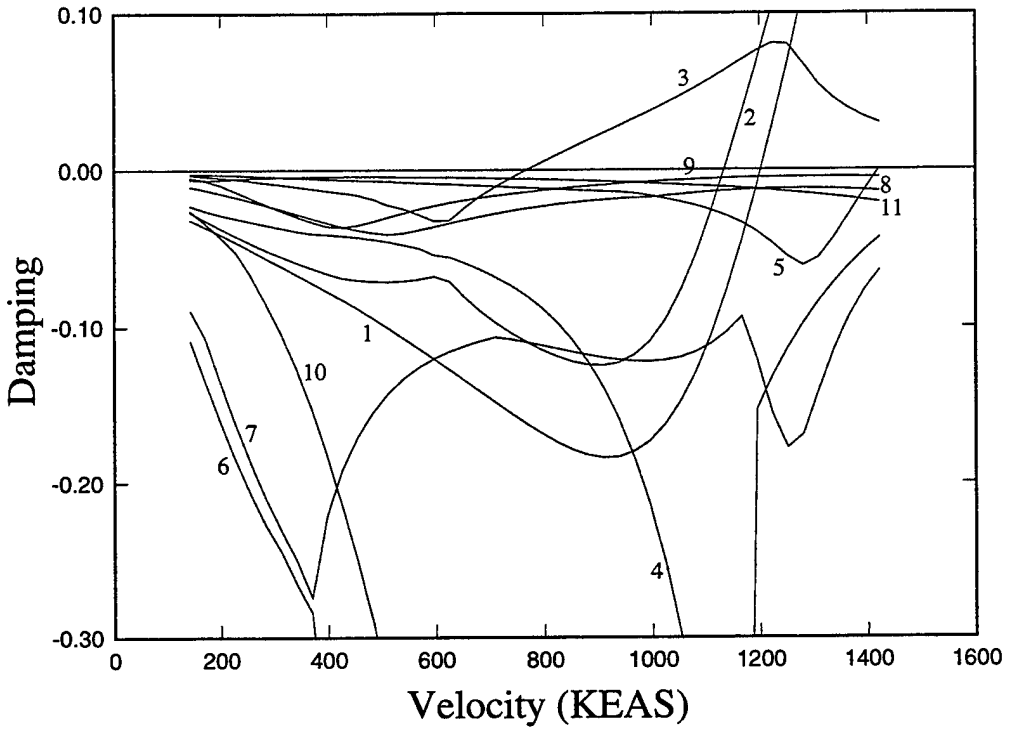

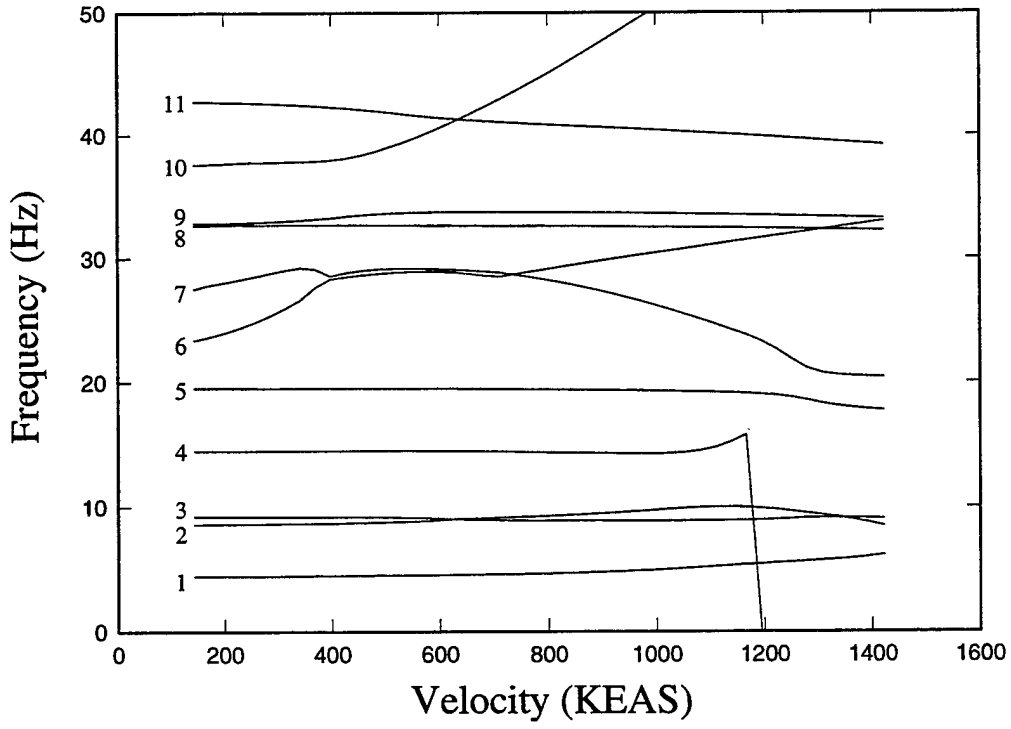

Figure 19: V-g-w Plot of F/A-18 Aircraft with a Tip Missile for Symmetric Boundary Conditions, Mach 0.9, Alt = -10K ft..

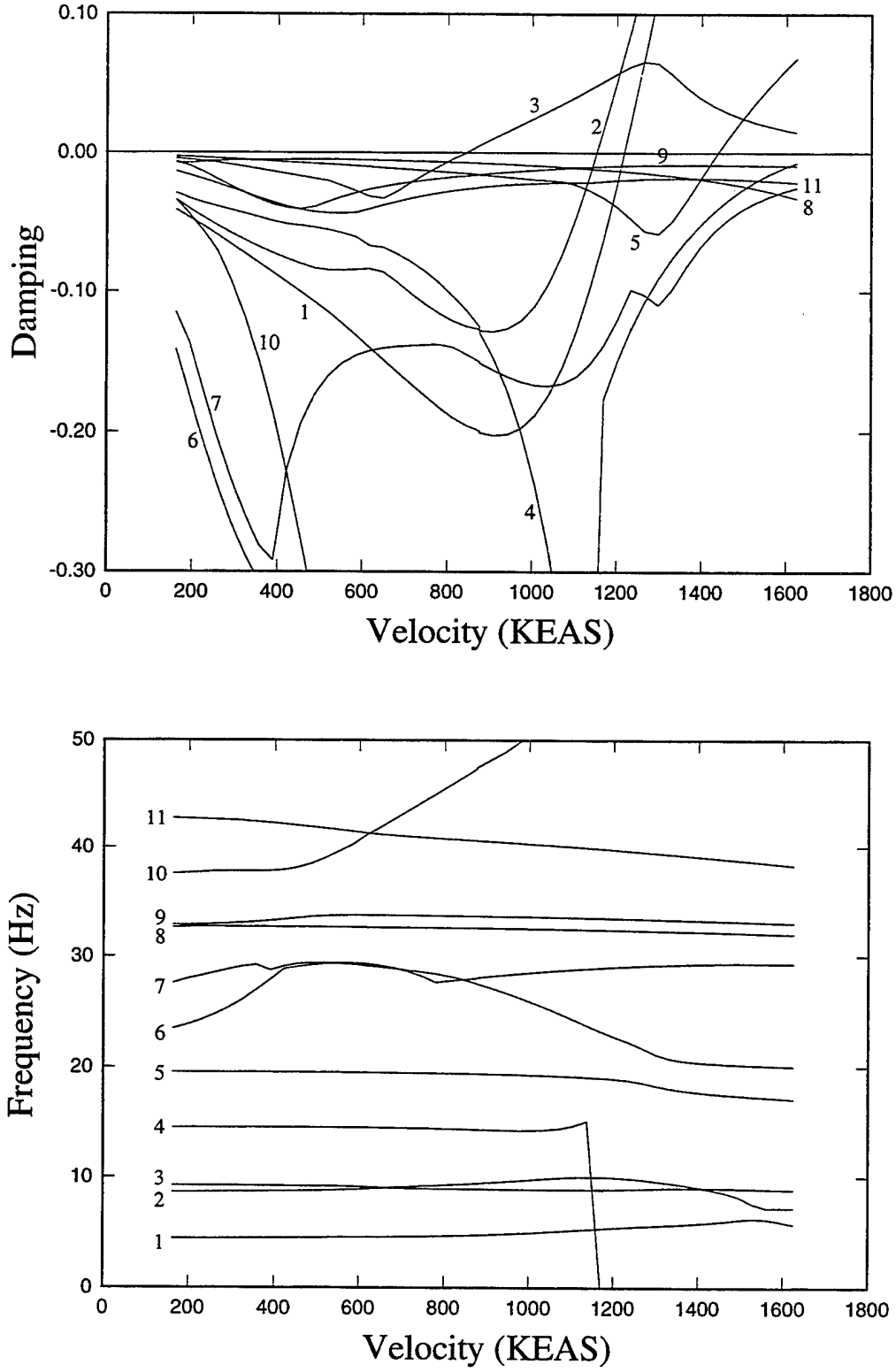

Figure 20: V-g-w Plot of F/A-18 Aircraft with a Tip Missile for Symmetric Boundary Conditions, Mach 0.9, Alt = -20K ft.

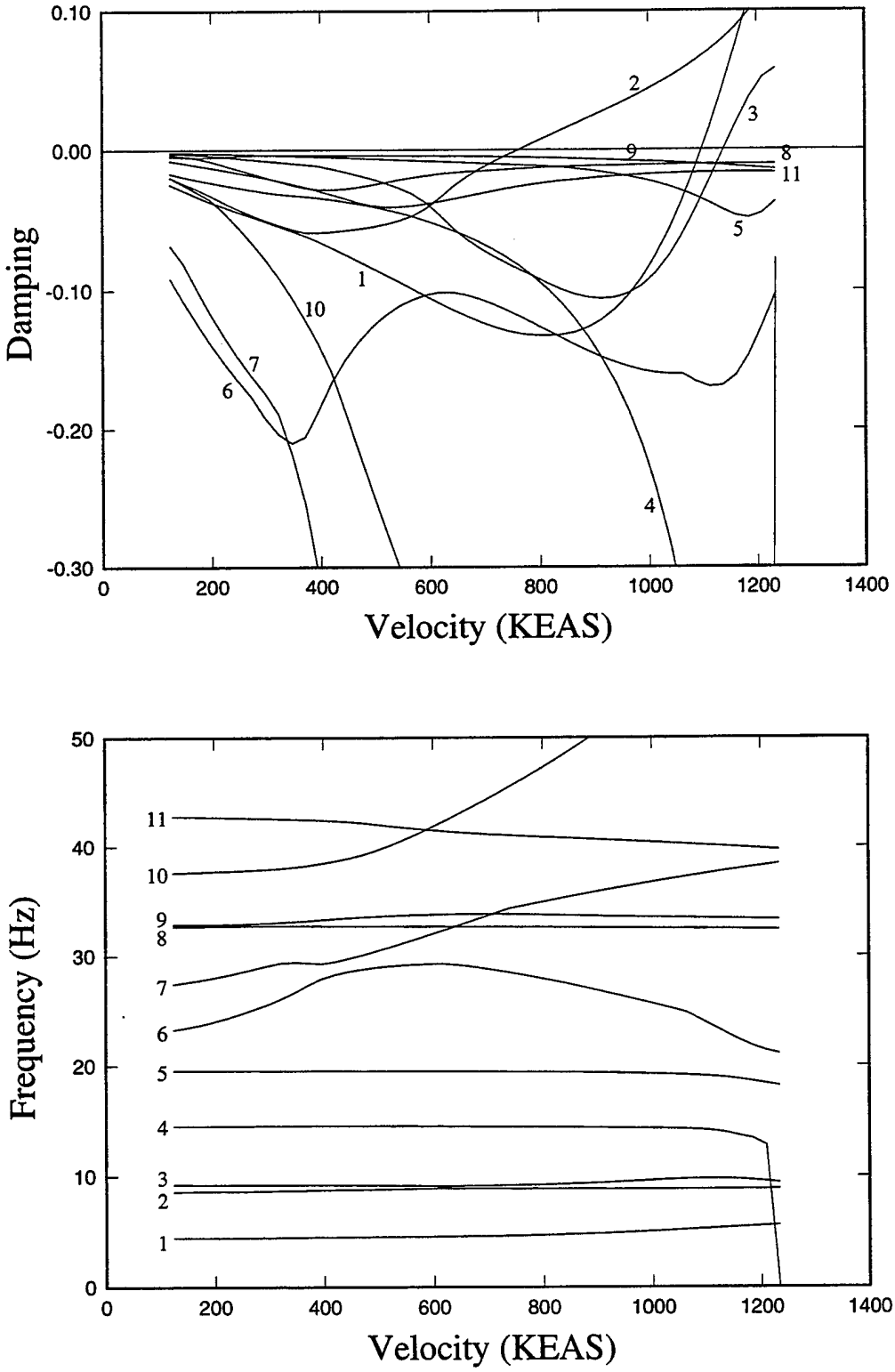

Figure 21: V-g-w Plot of F/A-18 Aircraft with a Tip Missile for Symmetric Boundary Conditions, Mach 0.95, Alt = Sea Level

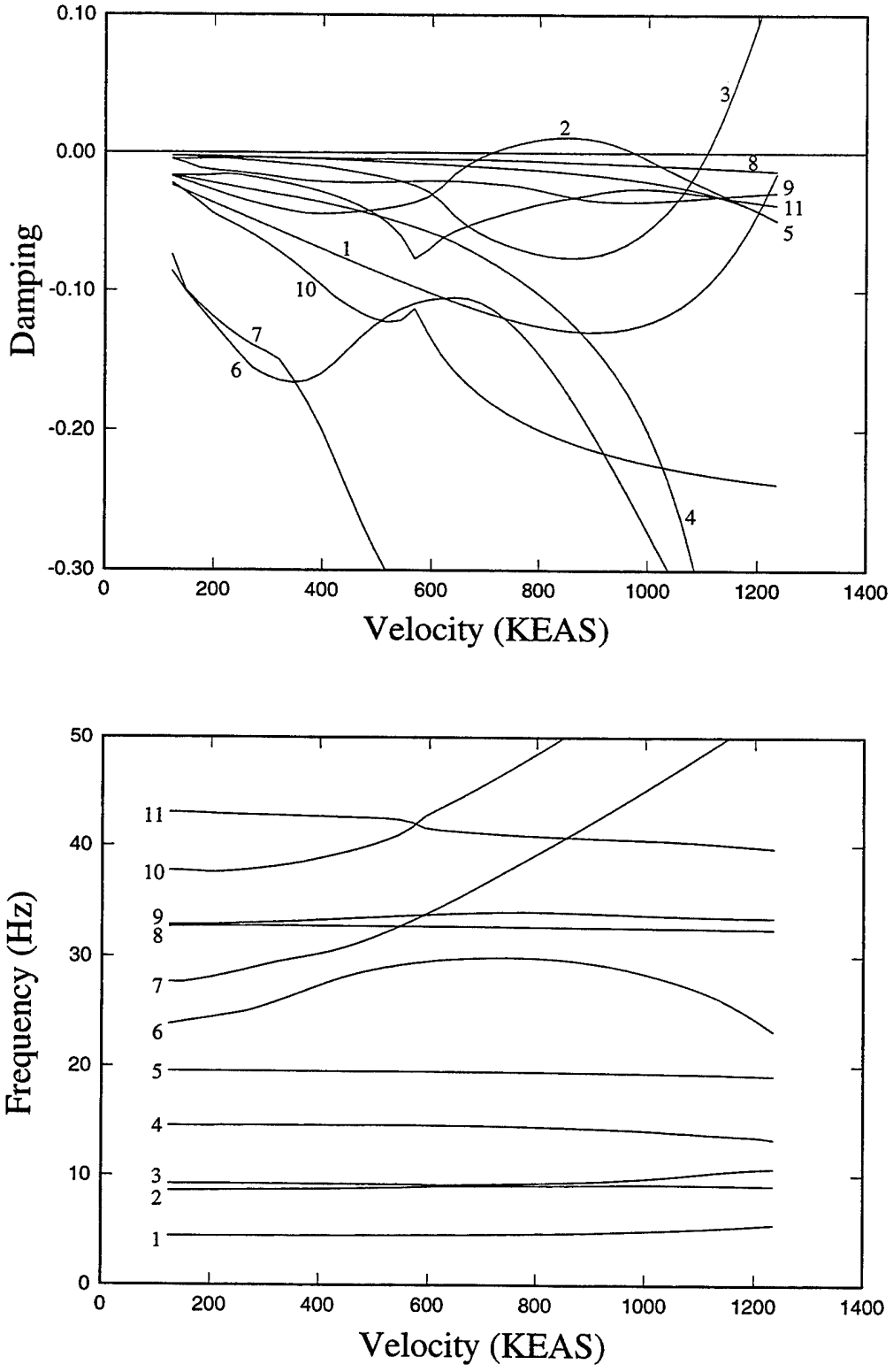

Figure 22: V-g-w Plot of F/A-18 Aircraft with a Tip Missile for Symmetric Boundary Conditions, Mach 1.1, Alt = Sea Level

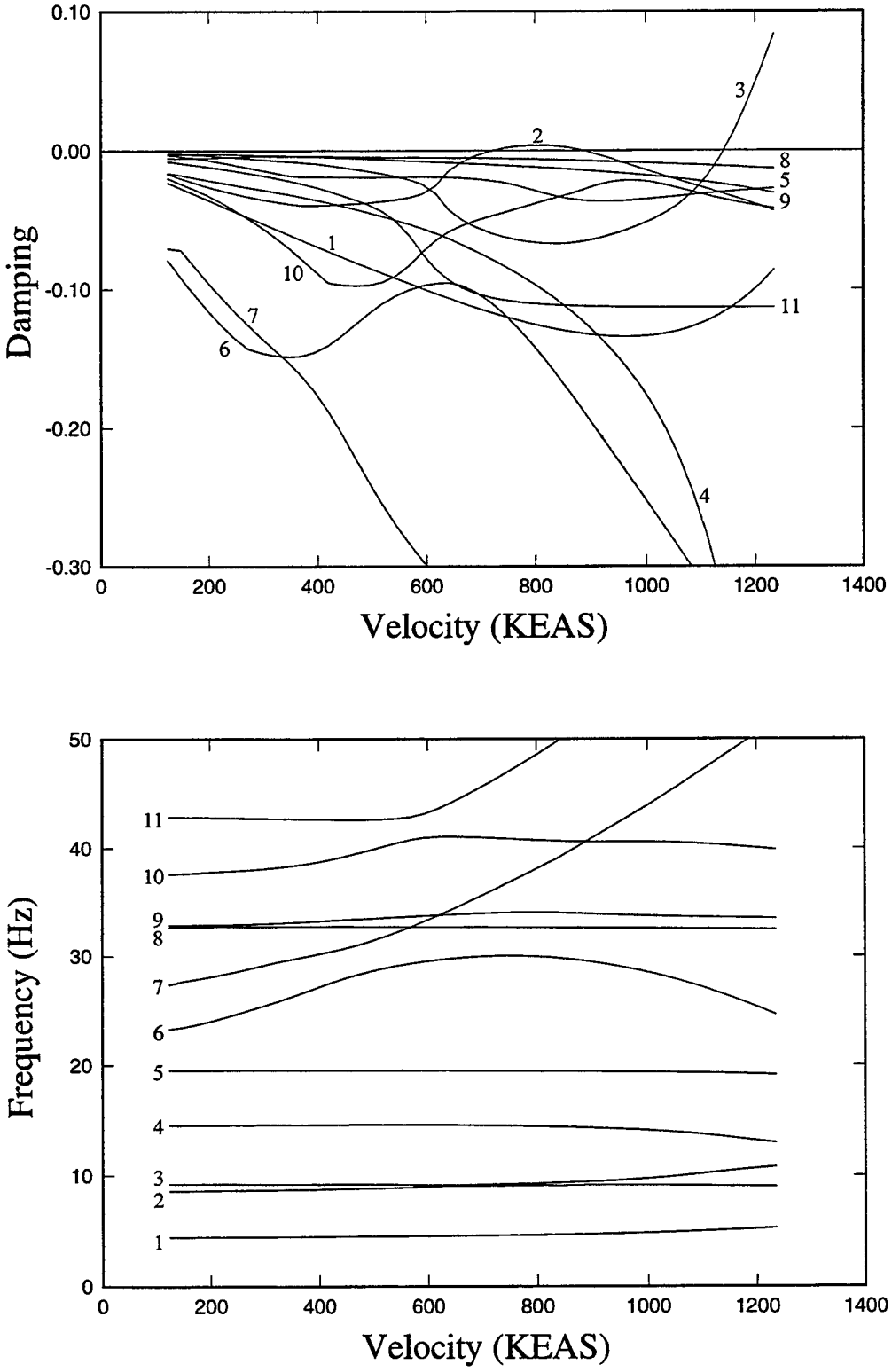

Figure 23: V-g-w Plot of F/A-18 Aircraft with a Tip Missile for Symmetric Boundary Conditions, Mach 1.15, Alt = Sea Level

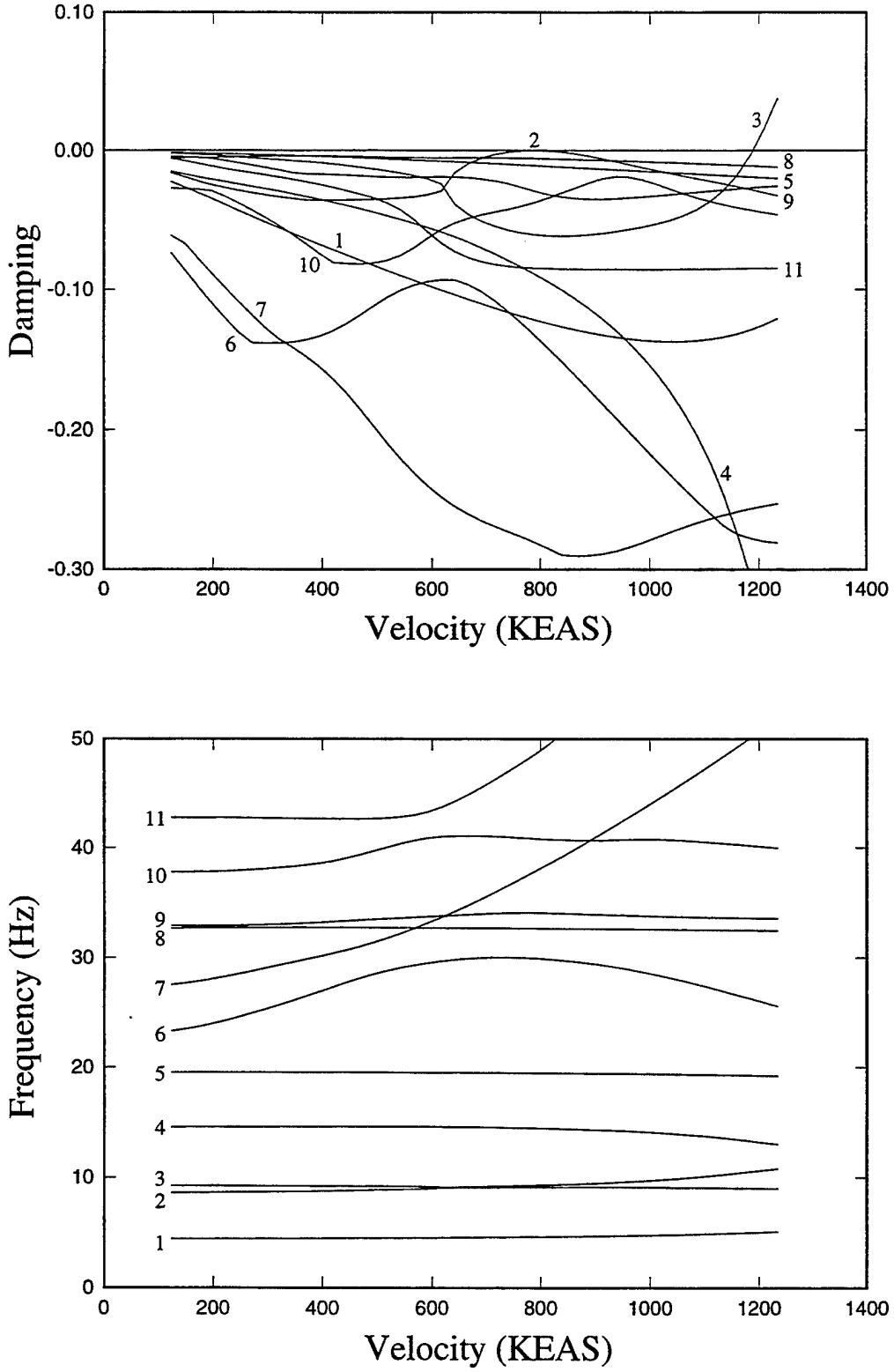

Figure 24: V-g-w Plot of F/A-18 Aircraft with a Tip Missile for Symmetric Boundary Conditions, Mach 1.2, Alt = Sea Level

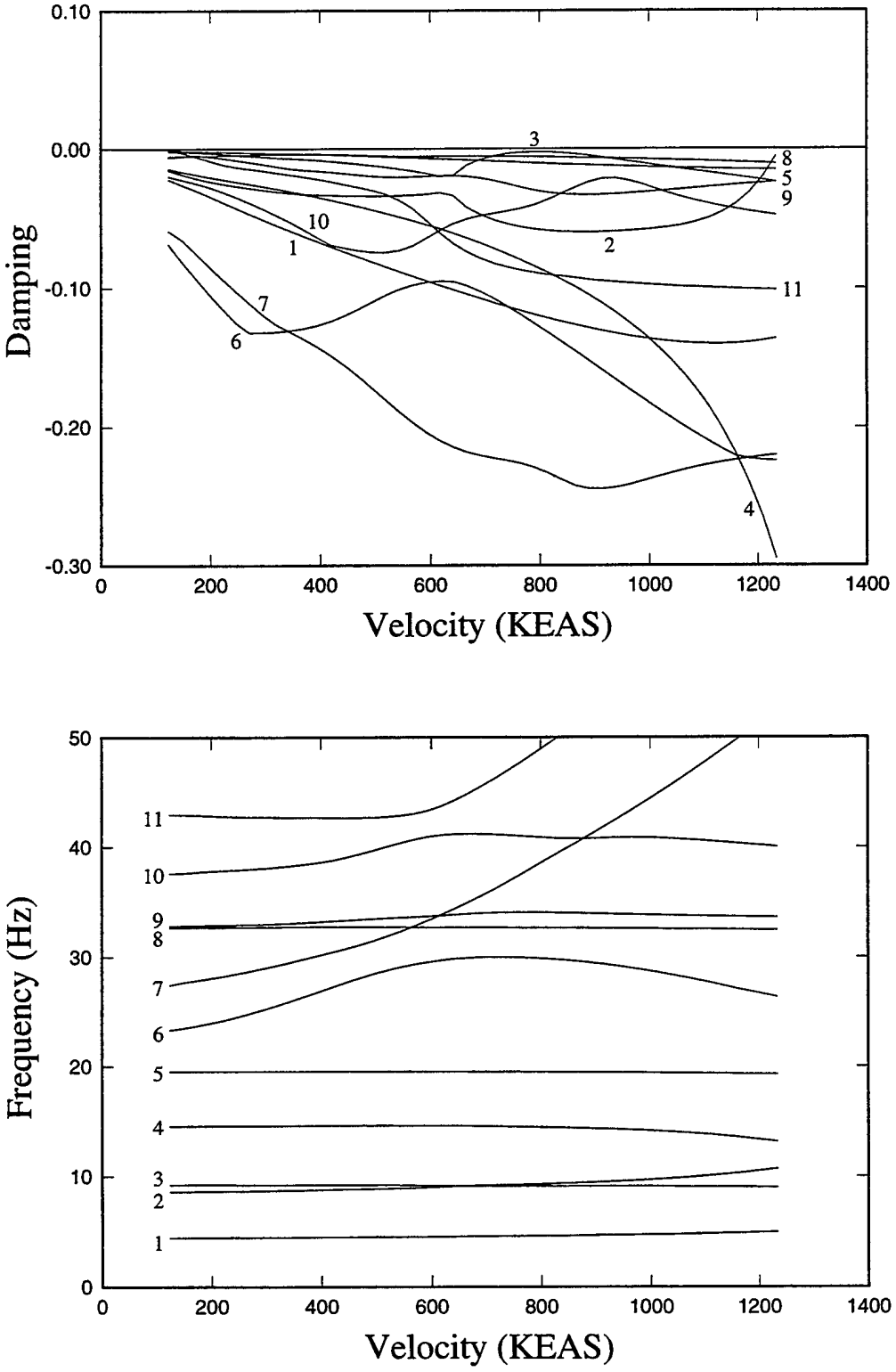

Figure 25: V-g-w Plot of F/A-18 Aircraft with a Tip Missile for Symmetric Boundary Conditions, Mach 1.25, Alt = Sea Level

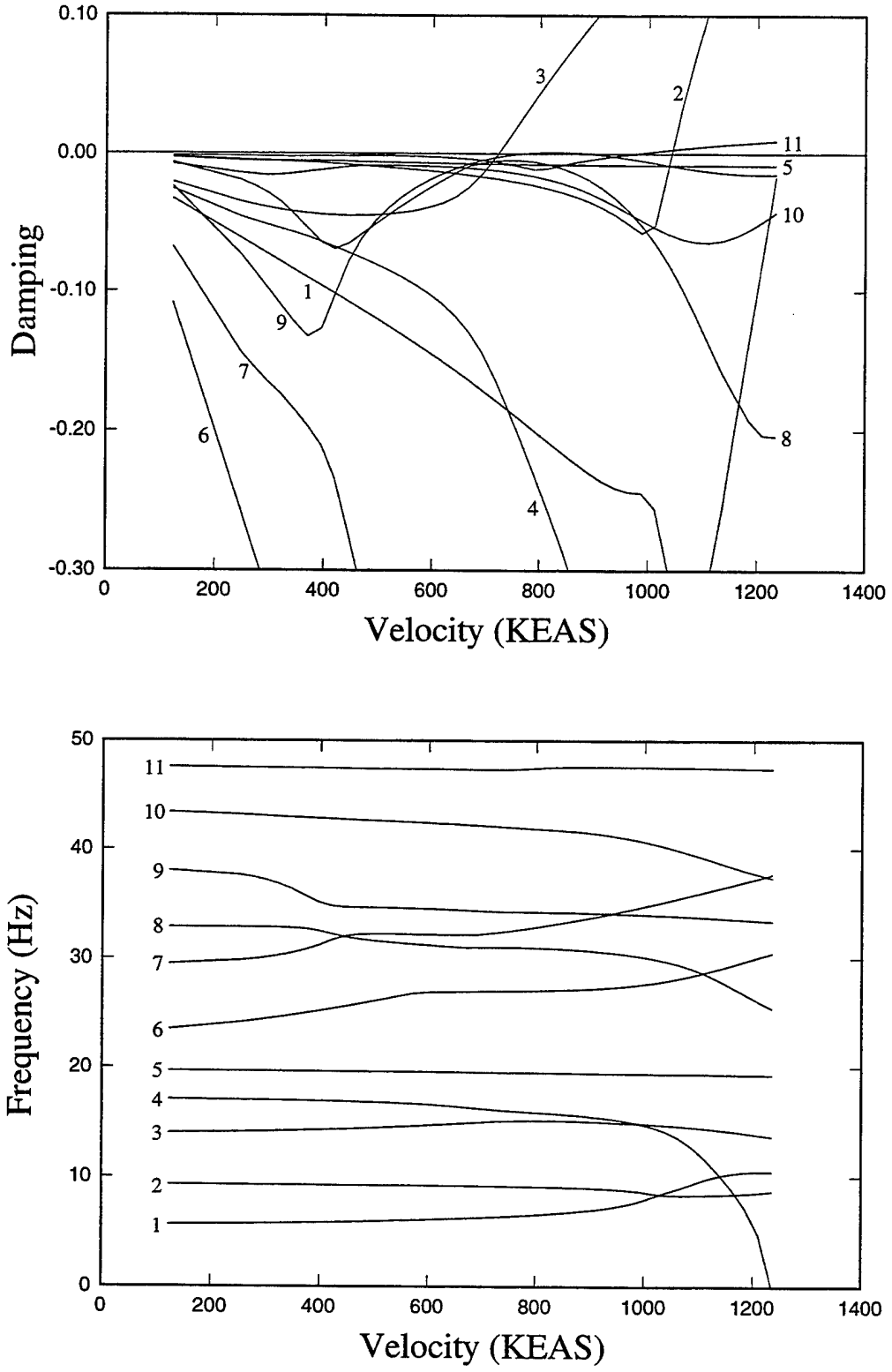

Figure 26: V-g-w Plot of F/A-18 Aircraft without a Tip MIssile for Symmetric Boundary Conditions, Mach 0.7

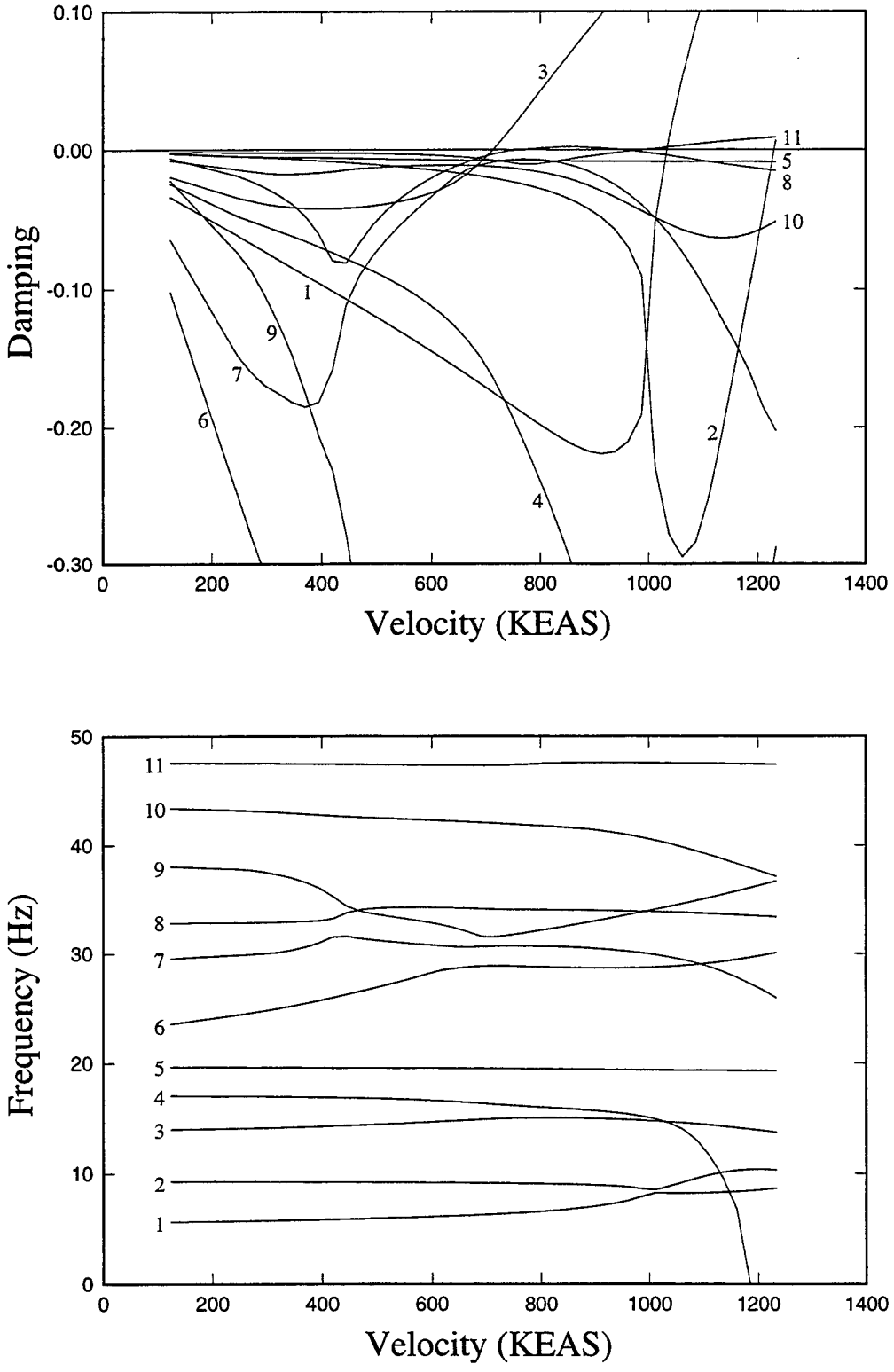

Figure 27: V-g-w Plot of F/A-18 Aircraft without a Tip Missile for Symmetric Boundary Conditions, Mach 0.75

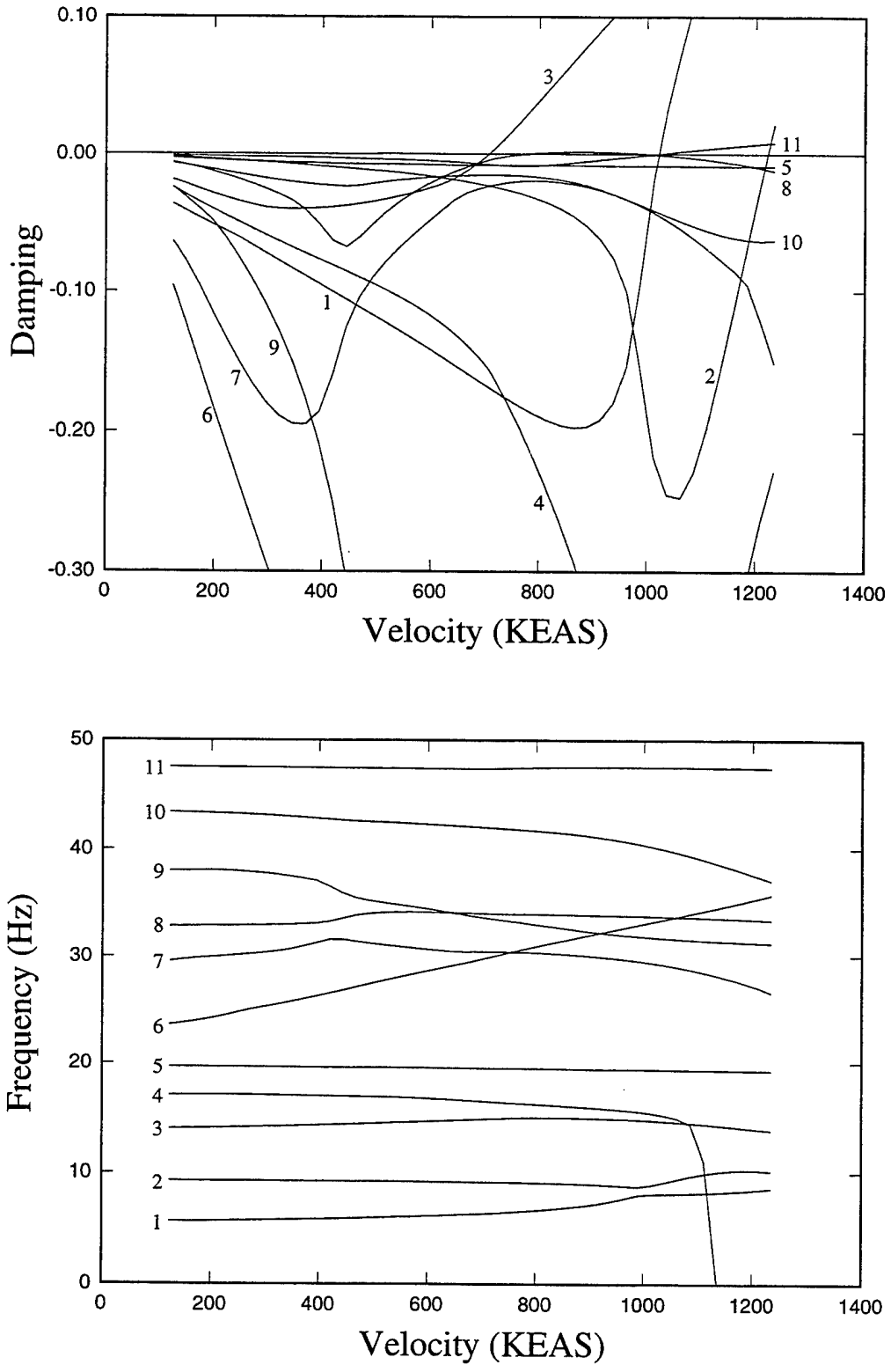

Figure 28: V-g-w Plot of F/A-18 Aircraft without a Tip Missile for Symmetric Boundary Conditions, Mach 0.8

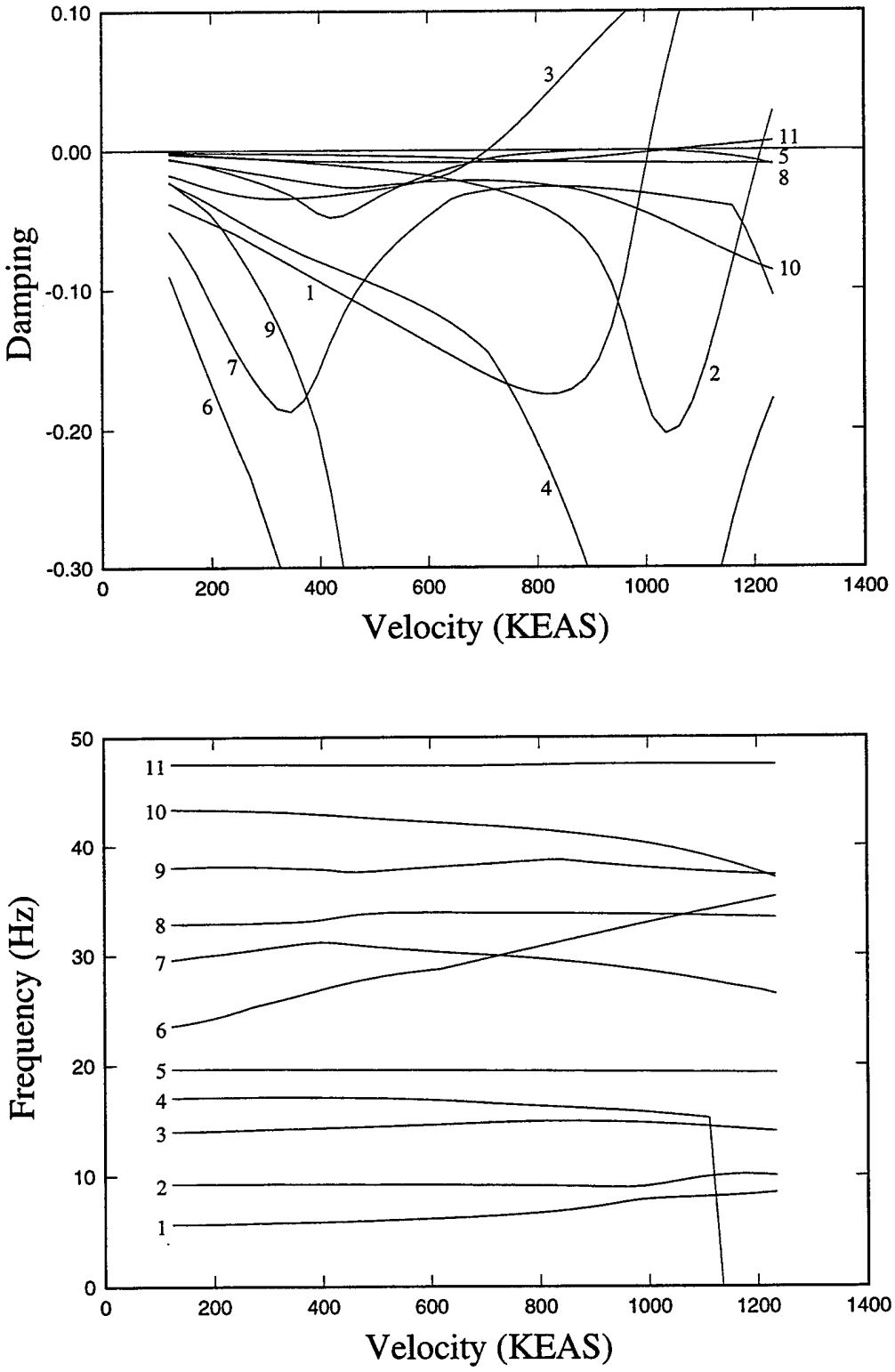

Figure 29: V-g-w Plot of F/A-18 Aircraft without a Tip Missile for Symmetric Boundary Conditions, Mach 0.85, Alt = Sea Level

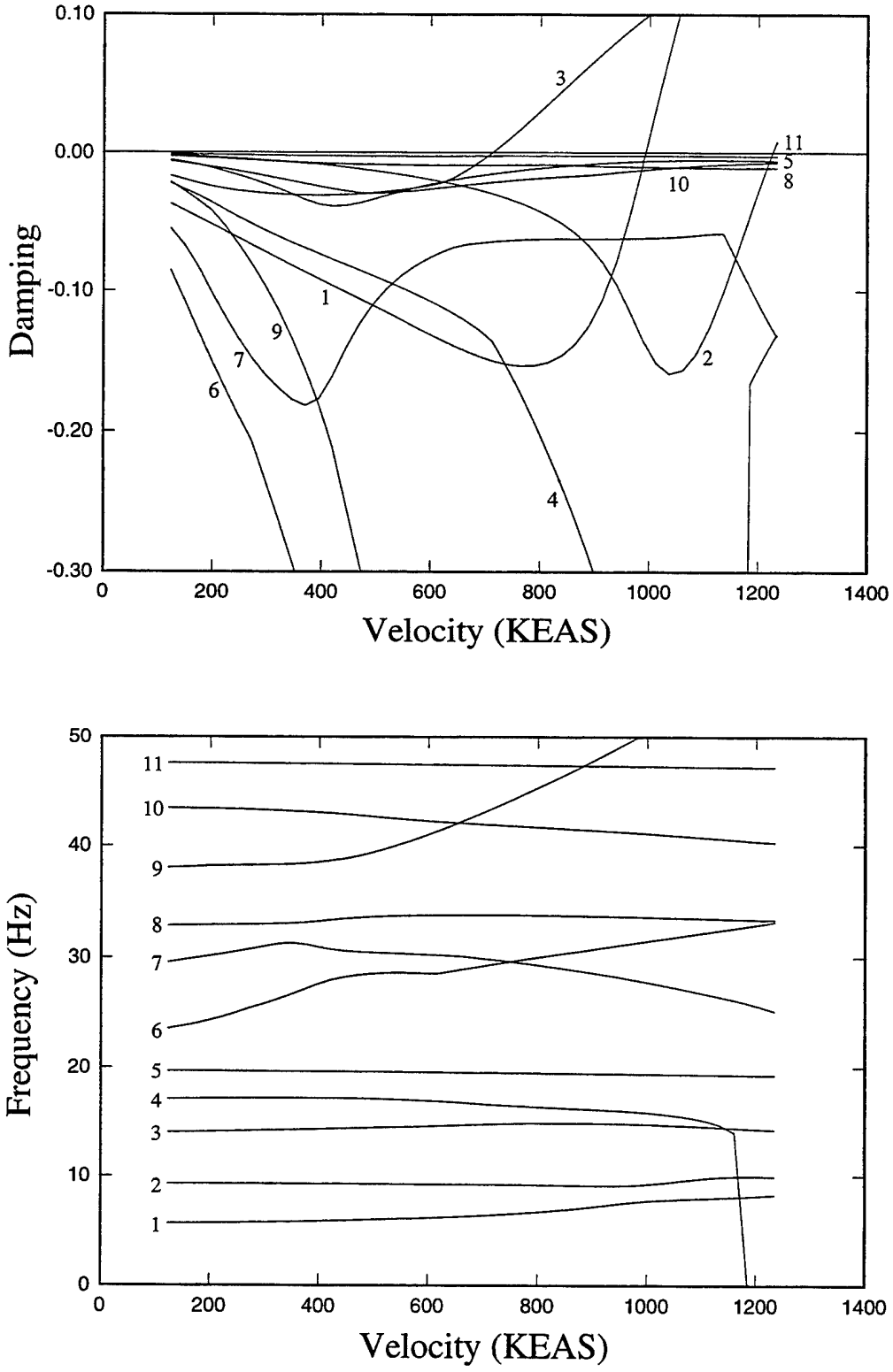

Figure 30: V-g-w Plot of F/A-18 Aircraft without a Tip Missile for Symmetric Boundary Conditions, Mach 0.9, Alt = Sea Level

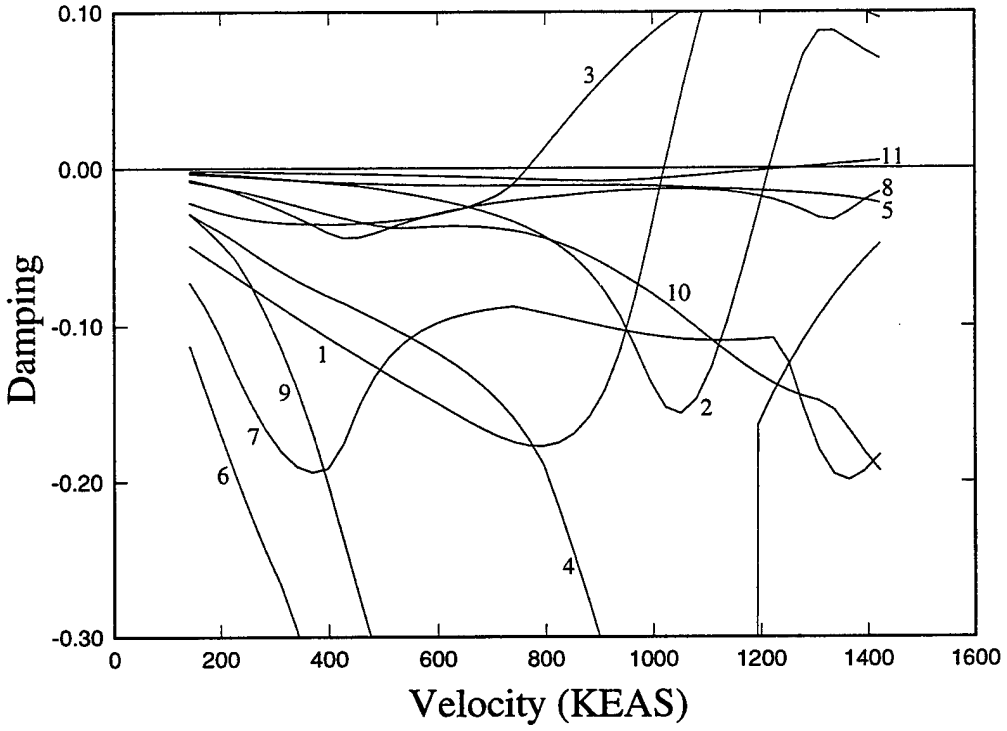

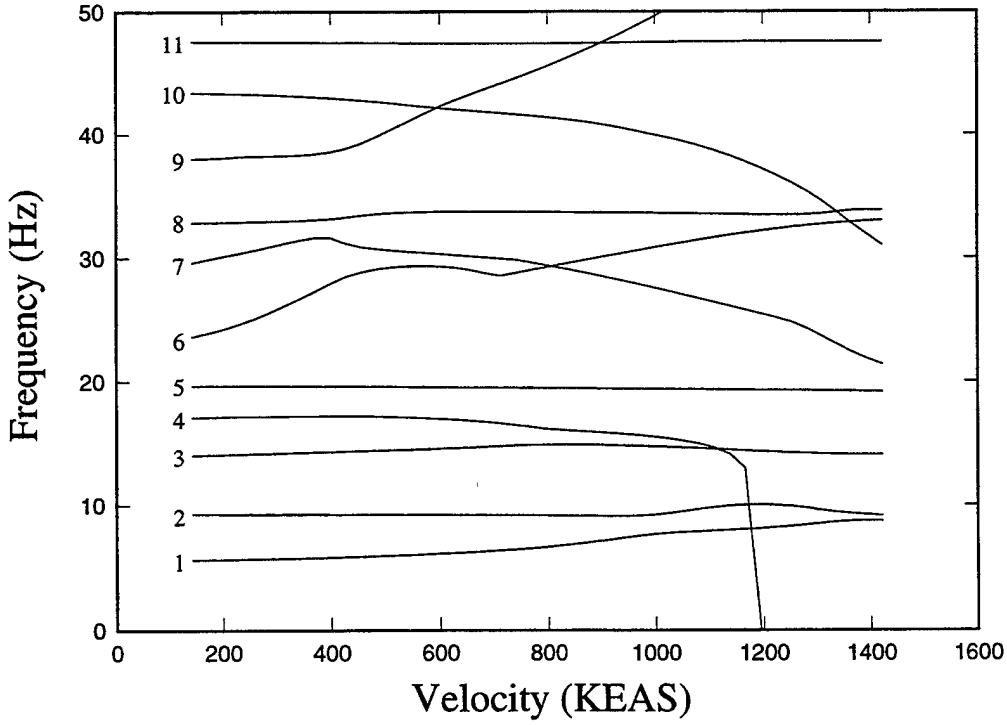

Figure 31: V-g-w Plot of F/A-18 Aircraft without a Tip Missile for Symmetric Boundary Conditions, Mach 0.9, Alt = -10K ft.

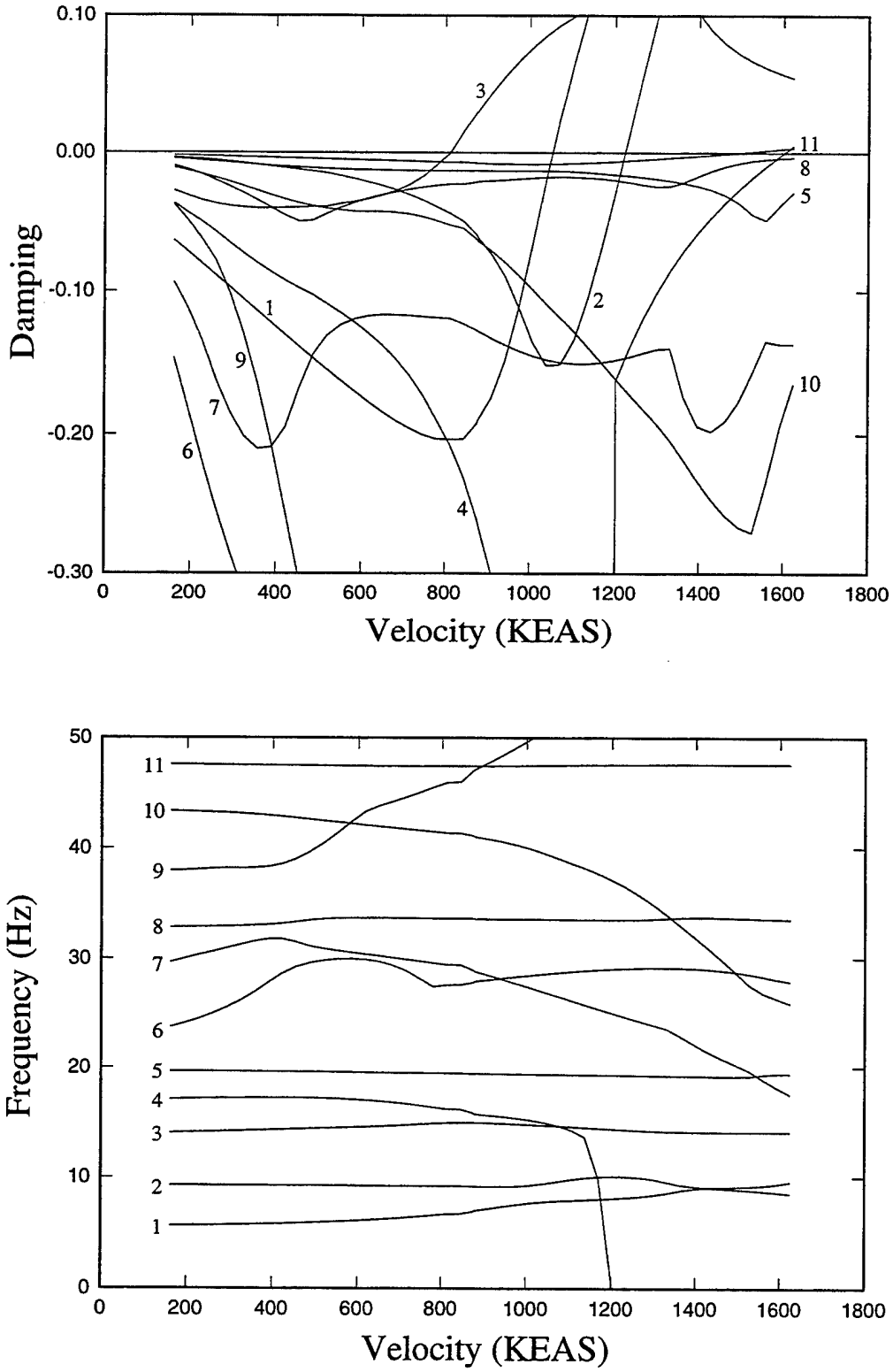

Figure 32: V-g-w Plot of F/A-18 Aircraft without a Tip Missile for Symmetric Boundary Conditions, Mach 0.9, Alt = -20K ft.

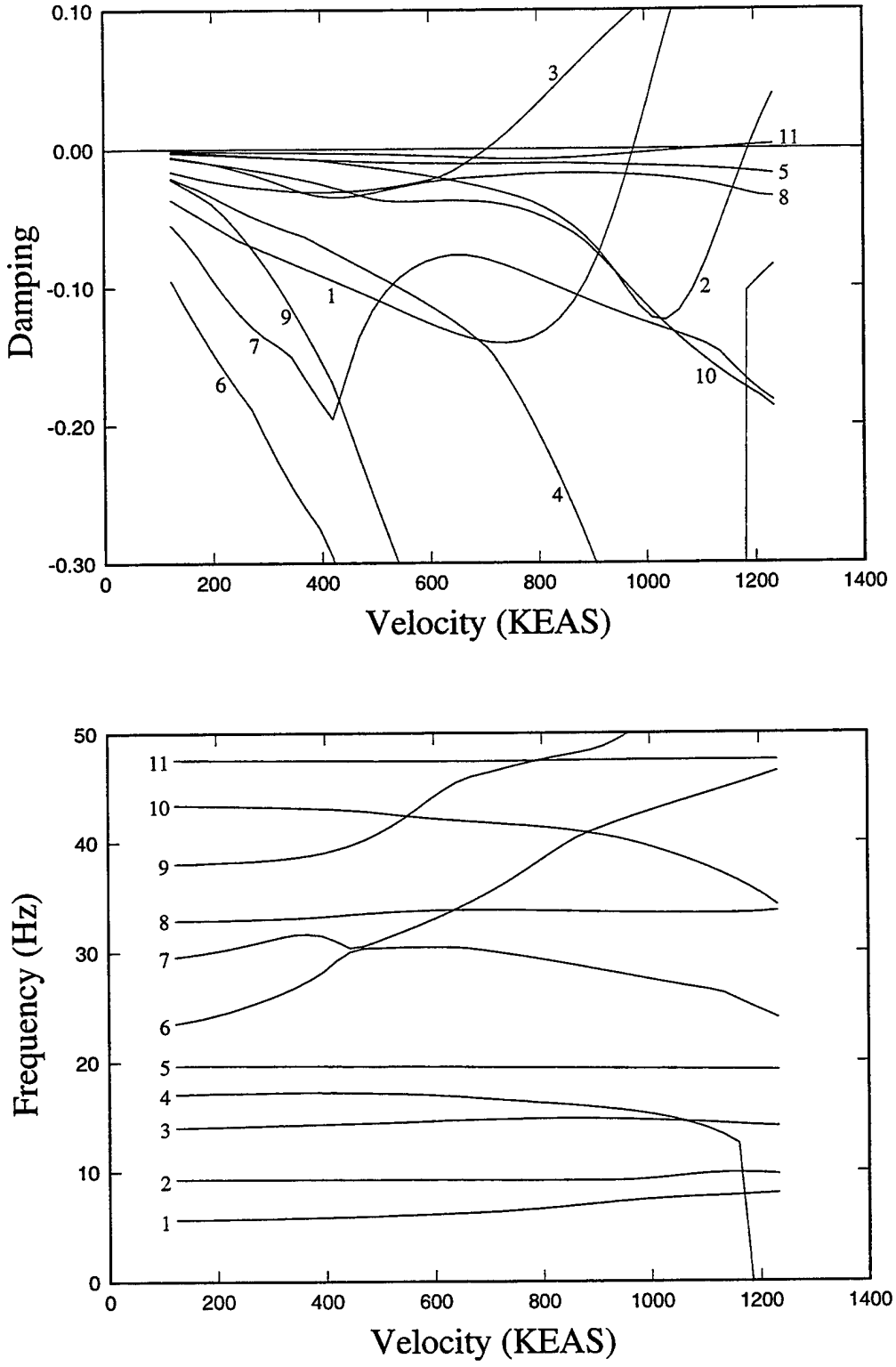

Figure 33: V-g-w Plot of F/A-18 Aircraft without a Tip Missile for Symmetric Boundary Conditions, Mach 0.95

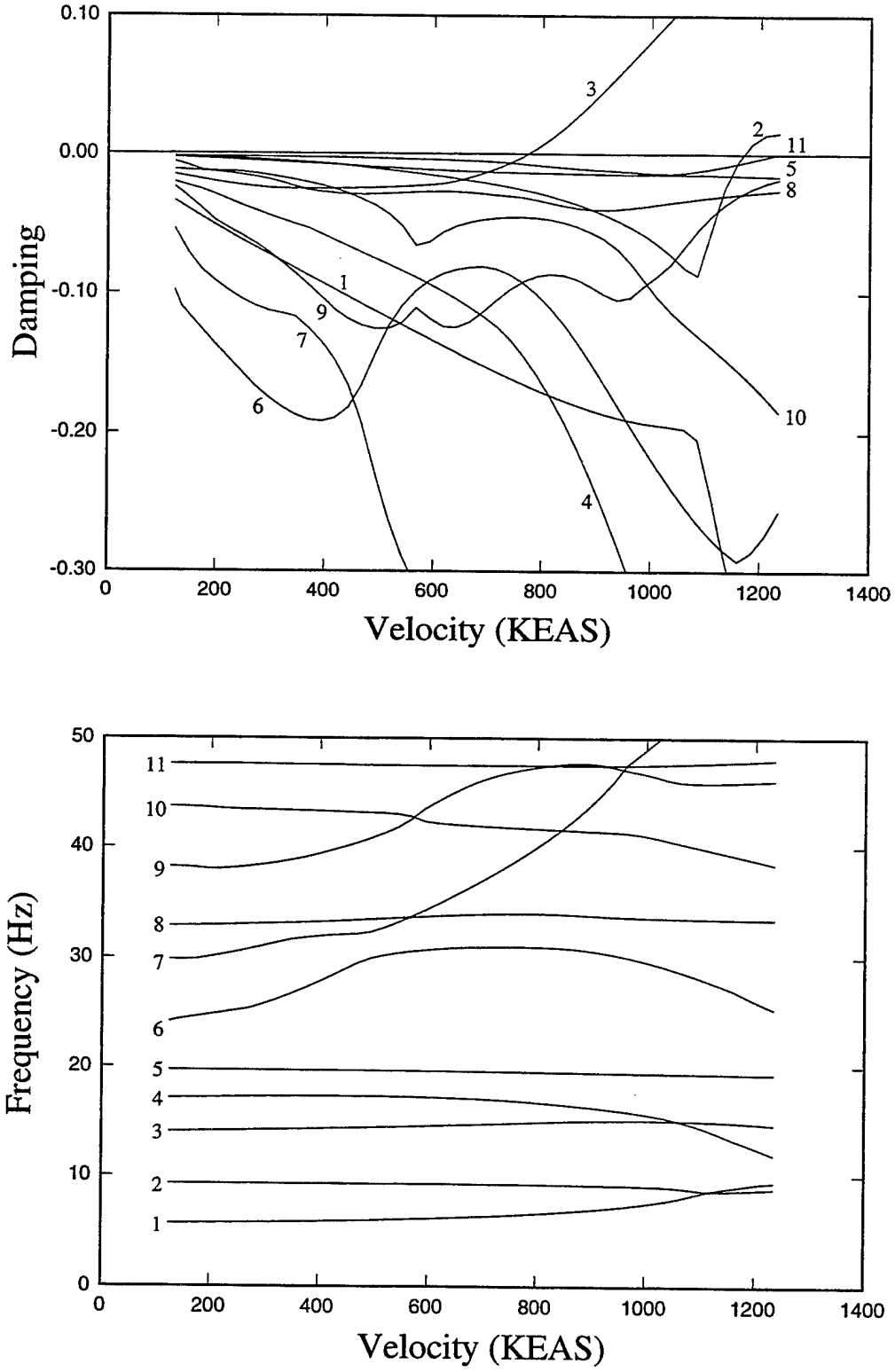

Figure 34: V-g-w Plot of F/A-18 Aircraft without a Tip Missile for Symmetric Boundary Conditions, Mach 1.1, Alt = Sea Level

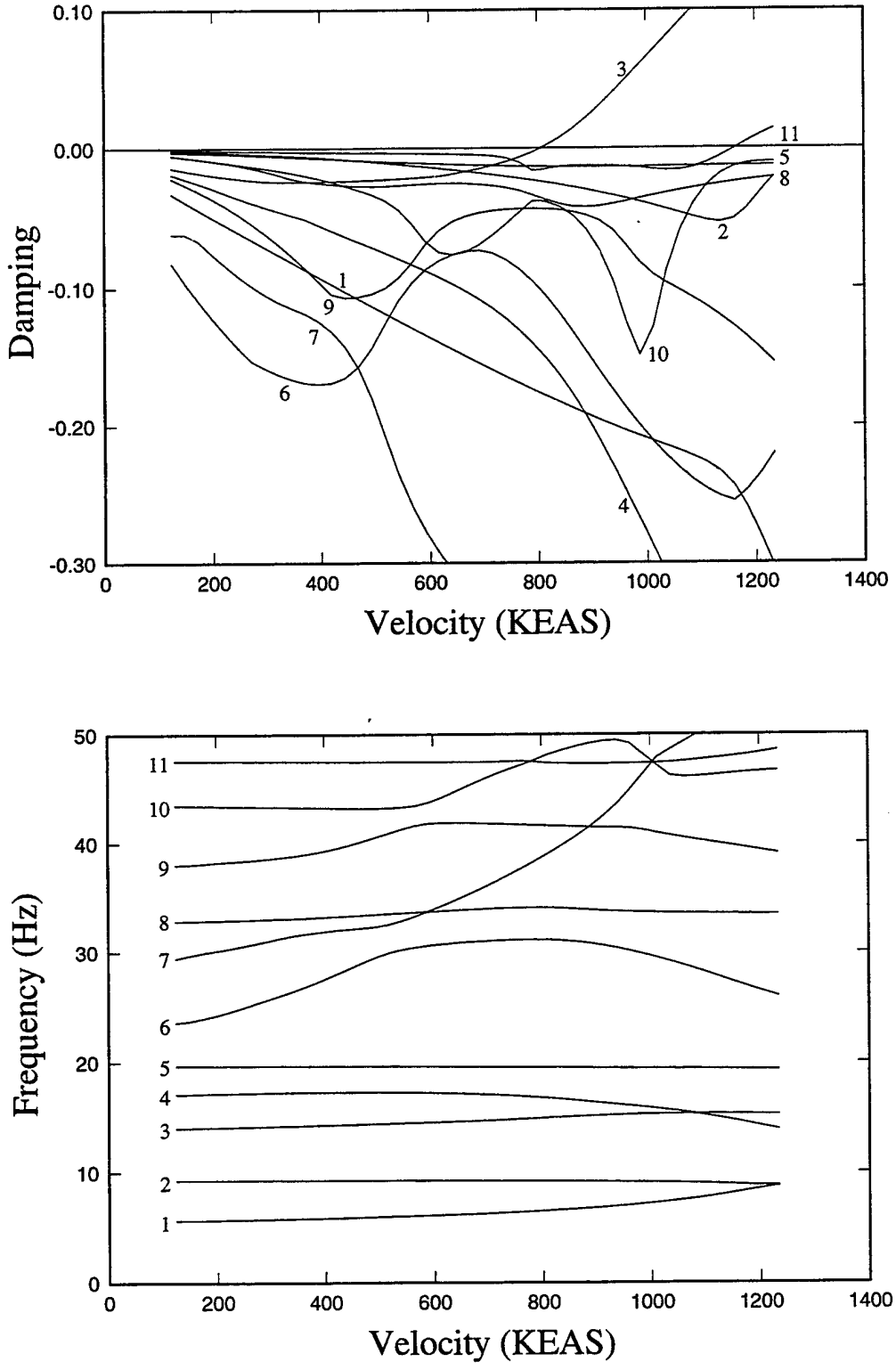

Figure 35: V-g-w Plot of F/A-18 Aircraft without a Tip Missile for Symmetric Boundary Conditions, Mach 1.15, Alt = Sea Level

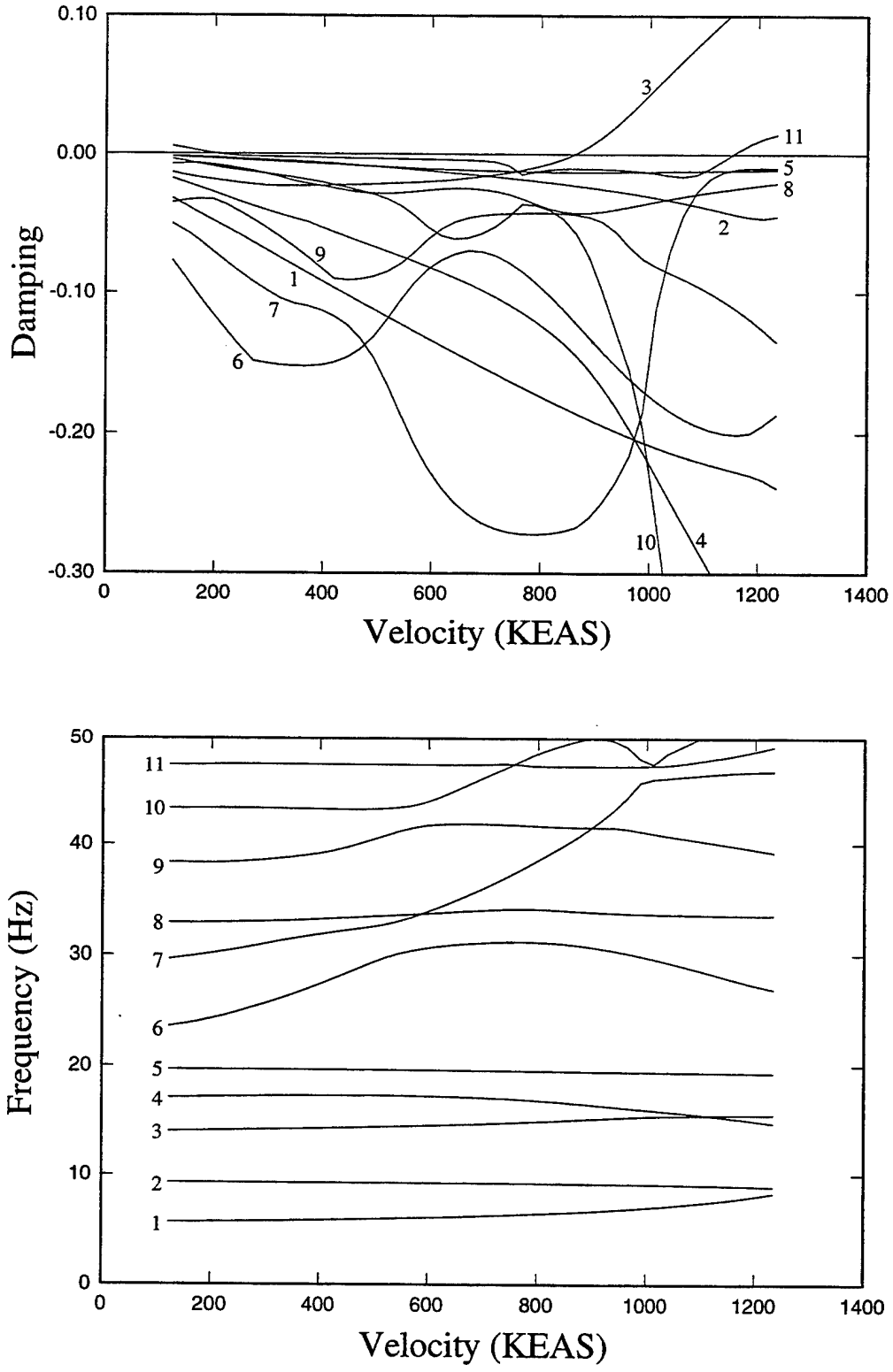

Figure 36: V-g-w Plot of F/A-18 Aircraft without a Tip Missile for Symmetric Boundary Conditions, Mach 1.2, Alt = Sea Level

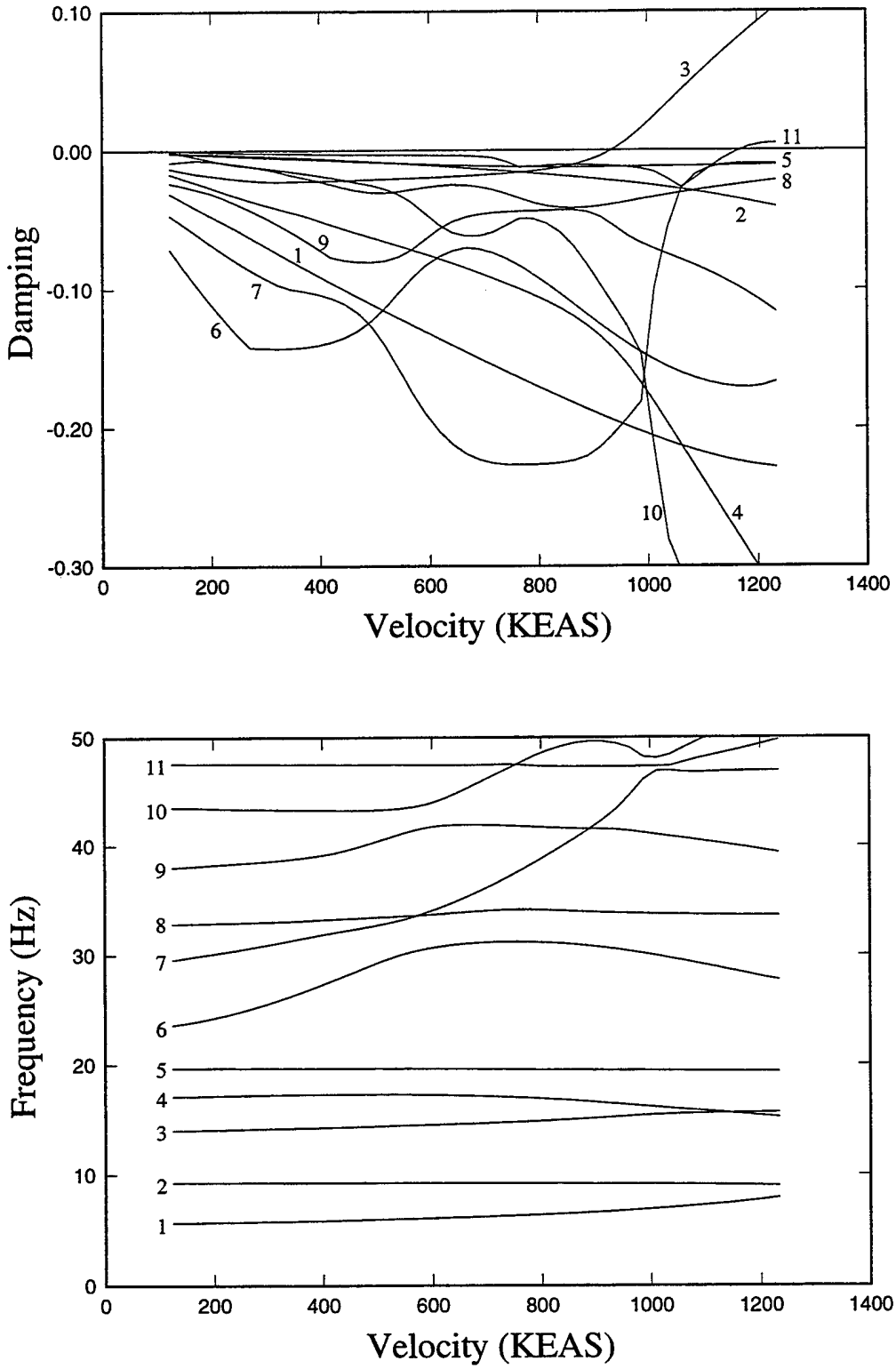

Figure 37: V-g-w Plot of F/A-18 Aircraft without a Tip Missile for Symmetric Boundary Conditions, Mach 1.25, Alt = Sea Level

SECTION VI

CONTROL SURFACE BLENDING FOR ROLL PERFORMANCE ENHANCEMENT

The goal of this section is to explore the utility of control surface blending to illustrate some benefits of AAW technology. Specifically, the capabilities of multiple control surfaces to effect trim on flexible wings will be examined. Static aeroelastic studies are to be performed on a beam/ rod model of the F-18 fighter aircraft, with beams modeling the fuselage, wing, control surfaces, missile launcher, horizontal stabilator, and vertical tail stiffnesses. General trends involving aileron effectiveness of the control surfaces with variation of dynamic pressure will be presented to establish a foundation for multiple control surface blending. Reduction of the wing stiffness of the aircraft model is used to establish whether roll performance requirements can be met using multiple blended control surfaces on a flexible wing. These flexible wing studies are also used to illustrate the increased roll maneuver control power of AAW technology.

Analytical Tools

To accomplish the objectives of this paper the Automated Structural Optimization System (ASTROS) is used for all analytical studies. ASTROS is a multidisciplinary design tool capable of incorporating statics, dynamics, and aerodynamics disciplines for analysis and optimization of finite element models[6]. One capability ASTROS provides is the ability to design linear structures in the presence of static aeroelastic loading. These designs can be driven by specifying limits on any of the following scalar quantities which are particular to static aeroelastic design: the stress or strain due to a specific maneuver, the required flexible to rigid ratio of the calculated stability derivatives, and the aileron effectiveness of the flexible aircraft. Antisymmetric static aeroelastic analyses are applied for roll performance, which includes design for aileron effectiveness. Some of the variables for analysis include roll rate and control surface deflection. Static aeroelastic studies are limited to a wing, fin, and canard configuration, each of which may have multiple control surfaces defined. Trim is achieved for either symmetric or antisymmetric analyses when the rigid body, elastic, and aerodynamic forces and moments are in equilibrium. In previous versions of ASTROS, when trimming for roll, only one variable could be 'free' for solution of this equation; therefore, at most one control surface deflection could be utilized as a variable for antisymmetric trim analyses. The inability of previous versions of ASTROS to utilize multiple control surfaces for aircraft trim is addressed through a trim module augmentation.

To address this issue, under contract with the USAF, Northrop Grumman created an enhanced trim module for ASTROS called the Adaptive Multi-Dimensional Integrated Controls (AMICS) module. AMICS incorporates a subset of the 'Generic Control Law' for conceptual and preliminary design[10]. This algorithm automates control surface blending based on aircraft stability and control derivatives for trim and transient maneuvering. Control surface scheduling and limiting are also incorporated into the design. Constraints which are input by the user include: control surface physical position limits, dynamic pressure limits, hinge moment limits, and scheduling of control surface deflections by Mach number versus angle of attack. Trim is achieved by the equilibrium of the rigid body, elastic, and aerodynamic forces and moments.

There can be an unlimited number of control surfaces defined; therefore, there can be an infinite number of possible surface deflections which satisfy equilibrium. Because of more unknowns than equations, trim is iteratively solved using the Newton-Raphson method which produces minimal actuator command signals. This method requires the derivatives of the forces and moments with respect to angle of attack, sideslip angle, and generalized roll, pitch, and yaw controller values. The end result is the minimum blended deflections of multiple control surfaces which satisfies equilibrium.

Theoretical Background

All analyses are performed within the ASTROS environment, which uses a linear panel method to determine the aerodynamic loads, and the finite element method to determine the structural response. Standard surface and beam splining techniques are applied to transfer the aerodynamic loads from the aerodynamic grid points to the structural grid points. The program's static aeroelastic analysis discipline is employed to generate control and stability derivatives as well as to solve the roll equation of motion.

Steady Aerodynamics

The Unified Subsonic And Supersonic Aerodynamic Analysis (USSAERO) algorithm is utilized by ASTROS[6] for the computation of aerodynamic loads on the aircraft structure. For a lifting surface, this approach uses a superposition of vortex singularities applied to a discrete number of aerodynamic panels to calculate the pressure distribution about the surface. The algorithm is capable of accounting for wing thickness and camber effects through the boundary conditions. The basic equation is:

$$[A]\{\gamma\} = \{\omega\} \tag{14}$$

where the singularity values, $\{\gamma\}$, are obtained knowing the velocities due to a prescribed boundary condition, $\{\omega\}$, and the normal velocity influence coefficients, $[A]$. Once the singularities have been determined, velocity components are computed and the pressure coefficients at each of the panels is calculated. The pressure coefficients are converted to forces which in turn yield the rigid aerodynamic loads.

The aerodynamic influence coefficient matrix, $[AIC]$, is generated to calculate the incremental loads due to structural deformations. This matrix calculation is:

$$[AIC] = -4S[U][A]^{-1} \tag{15}$$

where S is the aerodynamic surface area, and the matrix $[U]$ is the velocities on the wing panel due to singularities on the wing. The aerodynamic influence coefficient matrix is important for the formulation of the equilibrium equation.

Static Aeroelastic Analysis

The static aeroelastic features in ASTROS[6] provides the capability to analyze linear structures in

the presence of steady aerodynamic loading. The equation of equilibrium is:

$$[M]\{\ddot{x}\} + ([K] - [A_f])\{x\} = [A_r]\{\delta\} \tag{16}$$

where $[M]$ is the mass matrix, $[K]$ is the structural stiffness matrix, $[A_f]$ is the aerodynamic stiffness matrix due to structural displacements, $[A_r]$ is the aerodynamic stiffness matrix due to control surface deflections, $\{x\}$ is the nodal displacement vector, and $\{\delta\}$ is the control surface deflection vector. The aerodynamic stiffness matrices, $[A_f]$ and $[A_r]$, are generated from the aerodynamic influence coefficient matrix, $[AIC]$.

Since roll performance is the focus of this study, antisymmetric analysis is employed. Stability and control derivatives, or sensitivities of the rolling moment coefficient, C_M, with respect to the roll rate, C_{M_p}, and control surface deflections, C_{M_δ}, respectively, are calculated from the aerodynamic stiffness matrices.

A convenient way of quantifying the ability of a particular control surface to generate rolling moments is through the control surface effectiveness parameter, ε. This value is defined as the ratio of a flexible control surface stability derivative to the flexible roll damping stability derivative. Thus there are n control surface effectiveness values given by:

$$\varepsilon_i = -\frac{C_{M_{\delta_i}}}{C_{M_p}}, \; i=1,\ldots,n \tag{17}$$

By this definition, control surface reversal occurs when the control surface effectiveness becomes negative, which is the consequence of the stability derivative of a particular control surface changing signs. In the examples studied during this effort, effectiveness values were determined as a function of dynamic pressure, thereby indicating the usefulness of each control surface over a range of flight conditions.

Another analysis technique utilized in these studies was the determination of control surface deflections required to achieve a desired roll rate. The static trim equation for roll:

$$qSb\left[\sum_{i=1}^{n} C_{M_{\delta_i}}\delta_i + C_{M_P}\frac{pb}{2V_0}\right] = I_{roll}\dot{p} \tag{18}$$

where q is the dynamic pressure, b is the wing span, δ is the control surface deflection, p is the roll rate, V_0 is the free stream velocity, I_{roll} is the rolling moment of inertia, and $\dot{p}$ is the roll acceleration. This equation has a unique solution for only one unknown variable, which is determined by the user. This variable is either a control surface deflection, the roll rate, or the roll acceleration.

The current problems explored are simplified by the assumption of constant roll rate. In terms of control surface efficiencies, the trim equation is given by:

$$\sum_{i=1}^{n} \varepsilon_i \delta_i = \frac{pb}{2V_0} \tag{19}$$

This equation for trim is further explored by considering a typical wing with only one control

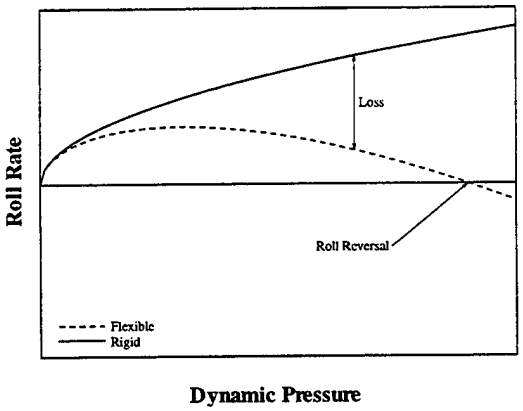

Figure 38: Comparison of Flexible and Rigid Roll Rates for Trim, Given Aileron Deflection

surface, an aileron, available for trim. By specifying a control surface deflection, and solving for roll rate over a range of dynamic pressures, the loss of ability of an aileron on a flexible wing to produce a required roll rate can be seen in figure 38. Roll reversal behavior is seen where the roll rate goes from positive to negative for a defined control surface deflection.

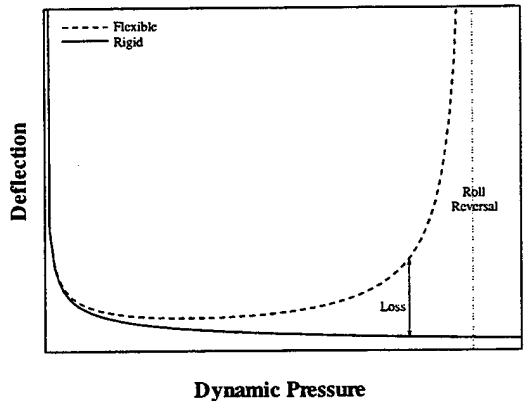

Figure 39: Comparison of Flexible and Rigid Aileron Deflections for Trim, Given Constant Roll Rate

Another method to examine this deficiency of an aileron on a flexible wing can be explored by specifying a required roll rate and solving for the deflection necessary for trim. The hyperbolic behavior of the aileron as dynamic pressure approaches roll reversal is illustrated in figure 39.

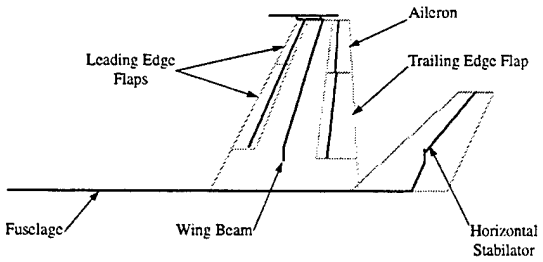

Figure 40: Diagram of Fighter Aircraft Finite Element and Aerodynamic Model

Blended Control Surface Trim

For a single control surface, the solution for trim in equation (19) is trivial. For multiple control surfaces, however, there exists an infinite number of solutions for the single equation.

The Adaptive Multi-Dimensional Integrated Controls (AMICS)[10] enhanced trim module, developed under Air Force contract with Northrop Grumman, provides the capability to determine a unique solution. The AMICS module takes the sum total of inertial, elastic, and aerodynamic forces and moments acting on the aircraft and defines trim to be achieved when this sum is zero. The Newton-Raphson method is used to solve the equations. This method is an iterative scheme based on a minimum control energy criteria in which the effectiveness of each control surface is taken into account. The derivatives of the rolling moment with respect to generalized roll controller values for each control surface provides the search directions. In effect this procedure minimizes the overall control surface actuator command signals, enabling a roll maneuver to be performed using the minimum amount of control surface deflections.

Example: Fighter Aircraft

This example utilizes a half model of a typical fighter aircraft where the fuselage, wing, horizontal tail, and vertical stabilator are modeled as beams. The control surfaces are also modeled as beams, with rigid bars connecting to the hinge line and springs modeling actuators. Aerodynamic surfaces are modeled for the wing and horizontal stabilator. The structural and aerodynamic model is illustrated in figure 40.

The structural element properties simulate those of a generic F/A-18 aircraft[9]. The fuselage beam runs along the centerline from the cockpit to the horizontal tail. The wing, stabilator, and control surface beams are located along their respective elastic axes. The wing and stabilator beams both run approximately along the 40% chord of their respective aerodynamic surfaces.

The wing and stabilator aerodynamic surfaces are modeled such that they extend to the aircraft centerline. The wing has a semi-span of 225 in., with a root chord of 190 in. and a tip chord of 65

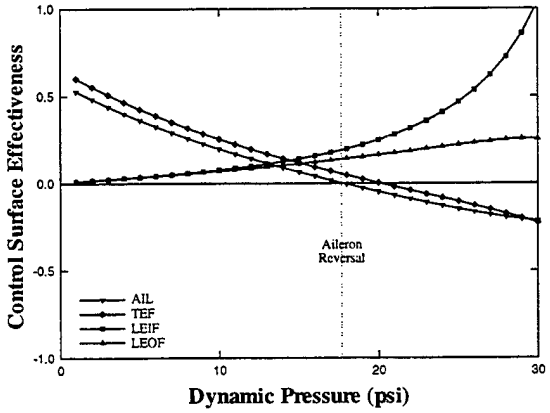

Figure 41: Control Surface Effectiveness for Fighter Aircraft Wing, Mach 0.9

in., which indicates a 3.5 aspect ratio. The wing leading edge is swept at 27 deg. The stabilator has a semi-span of 130 in., with a root chord of 120 in. and a tip chord of 45 in., which indicates a 3.2 aspect ratio. The stabilator leading edge is swept at 47 deg. The leading edge hinge line is at the 19% chord. The leading edge inboard flap starts at a span location of 54 in. and extends to the 165 in. span station. The leading edge outboard flap continues from the 165 in. span station to the wing tip. The trailing edge hinge line is at the 68% chord. The trailing edge flap starts at a span location of 42 in. and extends to the 154 in. span station. The aileron continues from the 154 in. span station to the wing tip.

Analysis began with a check of the structural model. Static and dynamic analyses provided validation of behavioral responses of a typical fighter aircraft[9]. The spline was checked by observing the 'rigid' and 'rigid splined' stability and control derivatives. Near equality of these two quantities indicates a good spline. The wing and tail are modeled with flat plate aerodynamics for antisymmetric trim analyses.

The fighter aircraft was first analyzed to establish static aeroelastic behavior trends. At Mach 0.9, the model was analyzed for roll trim at a constant roll rate of 90 deg/sec over a range of dynamic pressures. The flexible stability and control derivatives established the effectiveness of the control surfaces. The control surface effectiveness is illustrated in figure 41 for the leading edge inboard flap (LEIF), leading edge outboard flap (LEOF), trailing edge flap (TEF), and aileron (AIL).

The first noticeable characteristic of the control surface effectiveness trends is that they are not linear with dynamic pressure. It is also apparent that until very high dynamic pressure the trailing edge flap has slightly higher effectiveness values than the aileron. This is because the trailing edge flap has a much larger area than the aileron. The leading edge inboard control surface also has a higher effectiveness than the leading edge outboard control surface due to its much larger area.

Also evident is that with increasing dynamic pressure there is increasing effectiveness for the leading edge control surfaces, and decreasing effectiveness of the trailing edge control surfaces. The control surface effectiveness of the trailing edge flap and aileron, in fact, become negative indicating that roll reversal has occurred. The aileron reversal occurs at 18 psi. The trailing edge

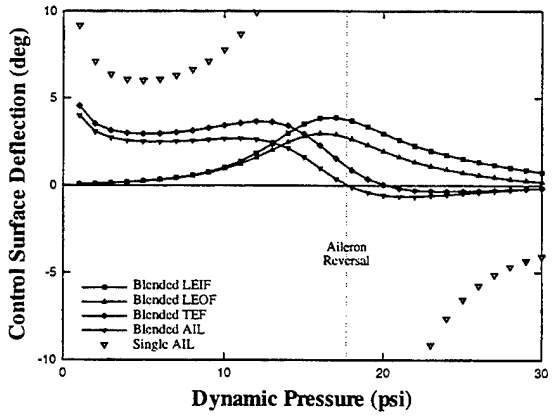

Figure 42: Roll Trim for Fighter Aircraft Wing, 90 deg/ sec Roll Rate, Mach 0.9

flap reversal is at a slightly higher dynamic pressure.

Roll trim is achieved by solving for the control surface deflections in the roll equation of motion. Control surface deflections for trim of the aircraft are exhibited in figure 42 for both a standard single aileron case as well as blending of all four control surfaces.

Trim employing the aileron alone shows a standard hyperbolic pattern about the roll reversal dynamic pressure. From 6 to 10 degrees of deflection of the aileron are needed for dynamic pressures up to 12 psi, and an increasingly large deflection is needed as the dynamic pressure approaches 18 psi, the point of aileron reversal. Above the reversal point, the deflection required for trim is negative and decreases from large values near the reversal point to around -5 degrees at high dynamic pressure. The trim of the vehicle is constrained by roll reversal.

Trim is achievable throughout the flight dynamic pressure envelope by employing blended leading and trailing edge control surfaces. A deflection magnitude of no greater than 5 degrees is required of any one surface, and the deflections are considerably smaller at high dynamic pressures. The largest deflection occurs for the leading edge inboard flap at a dynamic pressure slightly less than that of aileron reversal.

The relative deflections of the control surfaces appear to be dependent upon the relative values of control surface effectiveness. It is apparent that where the trailing edge flap deflection is larger than that of the aileron, the trailing edge flap control surface effectiveness is greater than that of the aileron. The leading edge inboard flap also exhibits this behavior of larger deflections than the leading outboard flap. The leading edge flap deflection becomes greater than the trailing edge flap deflection at the same dynamic pressure at which the control surface effectiveness of the leading edge flap becomes greater than that of the trailing edge flap. Also notable is that the aileron and trailing edge flaps are trimmed at zero deflection at the dynamic pressure at which control surface effectiveness values are at zero. The blended control surfaces exhibit a behavior of utilizing the most effective control surfaces to effect roll trim of the aircraft.

The next analysis of this model is intended to show the increased roll power of a simulated aircraft with reduced wing stiffness. Due to the spanwise bending effect on free stream angle of attack of a swept wing, the bending as well as the torsional stiffness is reduced. Therefore, the reduced stiffness aircraft is modeled with 50% wing torsional (GJ) and 50% bending stiffness (EI) of the original aircraft.

For comparison, the model was again analyzed for roll trim at Mach 0.9, at a constant roll rate of 90 deg/sec. The control surface effectiveness for all four surfaces is illustrated in figure 43.

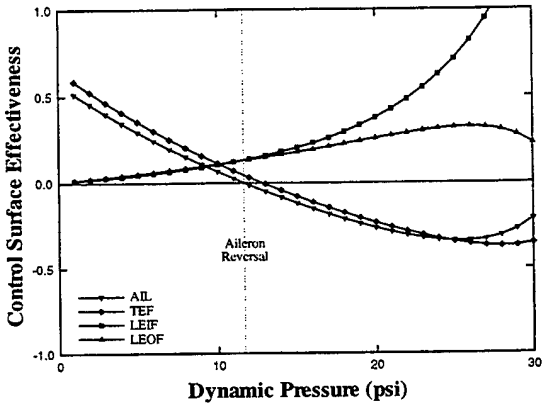

Figure 43: Control Surface Effectiveness for Reduced Stiffness Fighter Aircraft Wing, Mach 0.9

The characteristics of the trends are similar to those of the original stiffness model. The most noticeable difference is apparent at high dynamic pressures in which control surface effectiveness of the leading edge flaps for the reduced stiffness model is higher than that of the original stiffness model. Similarly, for high dynamic pressures, the trailing edge control surfaces have lower control surface effectiveness than the original stiffness model. Consequently, roll reversal for the aileron occurs at a lower dynamic pressure of 12 psi.

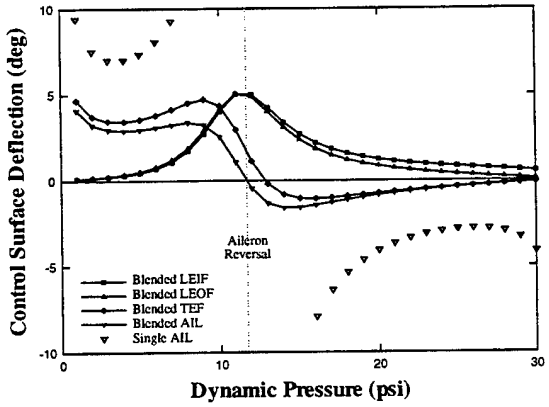

Figure 44: Roll Trim for Reduced Stiffness Fighter Aircraft Wing, 90 deg/sec Roll Rate, Mach 0.9

Control surface deflections for trim of the reduced stiffness aircraft are illustrated in figure 44. Again the single aileron deflections as well as the blended control surface deflections are shown.

The trim capability of the single aileron has been substantially diminished for the reduced stiffness model. The aileron is able to perform the rolling maneuver with deflections of 7 to 10 degrees up to a dynamic pressure of 7 psi. The decrease in stiffness of the wing corresponds to a decrease in ability for the aileron to effectively roll the aircraft at a prescribed rate.

The blended control surfaces are able to achieve trim throughout the dynamic pressure range with the largest deflections occurring at the reversal point. The leading edge inboard and outboard flaps both deflect 5 degrees to achieve the roll rate at this point, which is only slightly larger than the deflections required of the original stiffness model. The characteristic trends of the blended control surface trim for the reduced stiffness model mimic those of the original stiffness model. The most noticeable benefit of the reduced stiffness wing is the small deflections required by the control surfaces at post-reversal high dynamic pressure.

To further illustrate the benefits of multiple control surface blending for trim, the reduced stiffness model was analyzed with supersonic aerodynamics, at Mach 1.2, at a constant roll rate of 90 deg/ sec. The control surface effectiveness for all four surfaces is shown in figure 45.

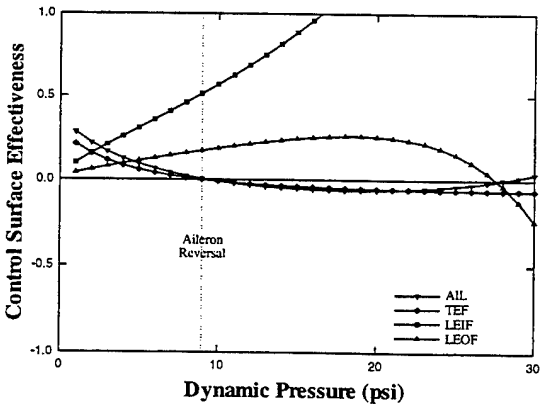

Figure 45: Control Surface Effectiveness for Reduced Stiffness Fighter Aircraft Wing, Mach 1.2

The most remarkable differences in the control surface effectiveness trends are accountable to the change in the aerodynamic center location from subsonic to supersonic aerodynamics. The leading edge surfaces have a generally higher control surface effectiveness than their subsonic counterpart, whereas the trailing edge control surfaces have a lower control surface effectiveness. The leading edge inboard control surface is the most effective. The aileron has a higher control surface effectiveness than the trailing edge flap; however, the aileron and trailing edge flap both reverse at the same dynamic pressure, 9 psi. After reversal, the trailing edge flap and aileron are generally ineffective.

The trim capabilities are illustrated in figure 46 for the multiple blended control surfaces. The aileron and trailing edge control surfaces are deflected from 5 to 10 degrees up to the dynamic

pressure of 3 psi and then are surpassed by effective leading edge surfaces. The leading edge inboard flap reaches a maximum deflection of 7 degrees between 4 and 5 psi, well before aileron reversal occurs. Beyond reversal, the flap deflections required become quite small, primarily due to the effectiveness of the leading edge inboard flap. Trim of an aircraft in the supersonic regime is best effected through the use of leading edge control surfaces.

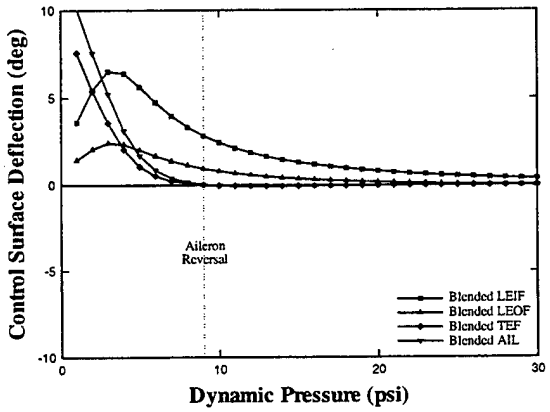

Figure 46: Roll Trim for Reduced Stiffness Fighter Aircraft Wing, 90 deg/sec Roll Rate, Mach 1.2

This study of a typical fighter aircraft asserts the utility of multiple blended control surfaces for roll trim. The usefulness of the implementation of leading edge control surfaces is particularly evident at high dynamic pressures. Roll performance is maintained for the reduced stiffness wings, with little increase of control power, indicating the need to address AAW technology in preliminary design.

SECTION VII

F/A-18A BUILT-UP FINITE ELEMENT MODEL

The main goals in the development of the F/A-18A built up Finite Element Model (FEM) are to develop an analytical tool for performing both static, dynamic and aeroelastic analysis on a F/A-18A wing. These analysises will be used to make accurate predictions of aileron reversal and flutter speeds of the F/A-18A, which will be used in support the Active Aeroelastic Wing (AAW) Flight Test program. Additional goals of the development are to provide Flight Dynamics Structures' engineers a tool for performing trade studies into the benefits of AAW technology on future fighter designs and to assist in the continuing validation of ASTROS.

Initially built by Capt Scott Hamilton of WL/FIBAD, the FEM is based upon top level drawings of the F/A-18A wing box obtained from NASA Dryden micro fiche and concentrated mass data from the McDonnell Douglas F/A-18A beam rod model. Orientation for the model follows standard practice for a right handed model where 'X' is in the direction of flow (chordwise), 'Y' is out the right wing (spanwise) and 'Z' is vertical. The model is represented by finite elements composed of skin, ribs, and spars. The skin is modeled using CQUAD4 elements, with all the out of plane rotation removed by single point constraints (SPCs) in directions 4, 5 and 6. The ribs and spars are composed of CROD and CSHEAR elements, with the rods along the upper and lower wing surface. Finally there are posts represented by CRODS which are oriented in the 'Z' direction. These posts provide the spars and ribs the ability to take compressive forces in the 'Z' direction. Figures 47 shows the general structural layout of the model.

The built up FEM was transferred to WL/FIBGE, Lt Christopher Shearer, in Jun 95 along with a list of modal frequencies obtained from the National Air and Space Administration (NASA) Dryden Flight Research Center and a top level wing box drawing. Run in Automated Structural Optimization System (ASTROS) version 10, the FEM would be optimized for a first bending frequency of 5.6 hz. Work began to match both higher frequencies and mode shapes by using the optimization function in ASTROS 10. This yielded poor results consisting of localized movement, incorrect modes shapes and incorrect frequencies.

The first modification was the removal of structure representing leading and trailing edge control surfaces. This was done to reduce model complexity as development on the wing box was being performed. Concentrated masses, CONM2s, associated with the flaps and ailerons, from the beam rod model, were rigidly attached to nodes on the wing box and offset with rigid bar (RBAR) elements.

The second change at correcting poor results was to add rib caps composed of CRODs to the top and bottom of each rib shear web. These rib caps allowed the model to absorb compressive and tensile forces in the 'X' direction generated by torsion motion. The third correction was to the tip missile launch rail. The use of rigid bars (RBARs) to attach the launch rail to the wing box tip prevented tip rotation about the 'Y' axis (spanwise). This precluded the first torsion mode from appearing. Analysis was conducted to determine the cause of this anomaly, however it was abandoned due to insufficient results. In order to retain the mass characteristics associated with

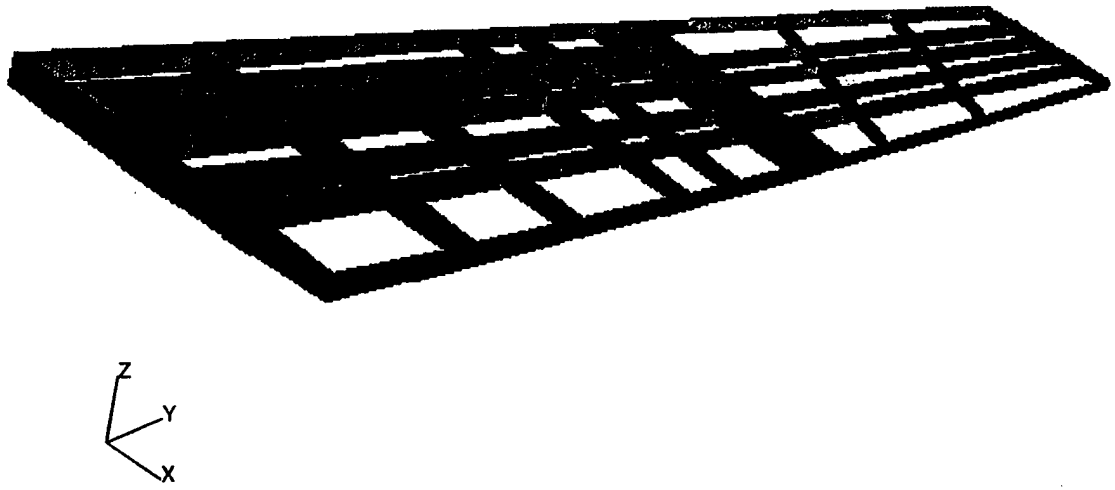

Figure 47: Initial Finte Element Model F/A-18

the launch rail, its CONM2s were attached to the tip of the wing box and provided offset values to their location in space.

The fourth change involved the modifying the boundary condition of the wing root. The roots' of #1, #2, #4, #5 and the rear spars were rigidly connected to the center of gravity of the aircraft utilizing RBARs. This configuration was based upon a visual inspection of the F/A-18A wing box to fuselage connection. Note that the aft spar was not rigidly attached.

The fifth major modification to the model was changing the material property of the CQUAD4s representing the skin from aluminum to a graphite epoxy composite. The composite layers were given ply orientations of +/-90, +/-45 and 0 degrees. The final change was commenting out all CONM2s with extensions of the form **TBOX**. It was assummed that these CONM2s were representative of both structural and non-structural wing box mass. In their place the material cards representing the aluminum ribs and spars and the graphite epoxy were given densities.

Figures 48 through 53 and table 11 are the results of the above changes. While they match well with the frequencies and mode shapes of beam rod model, the sizing results of the optimization yielded elements representing the skin, spars and ribs at approximately 1/10 their physical size. Dynamically this run provided the best results. Despite these positive results, they do not support the first goal of using the model to perform static analyses. The objective function of ASTROS 10 works to minimize weight. ASTROS 10 optimized the weight to be 569.94 lbs, compared to the summed weight of the CONM2 cards denoted by TBOX is 1591.15 lbs. Since there were no static constraints, i.e. stresses or deflections, ASTROS correctly optimized the structure to meet the modal frequencies.

Table 11: Comparison of Natural Frequencies for the Beam-Rod Model of F/A-18

Mode	Shape	ASTROS	McAir GVT	STARS
1	First Bending	5.60 Hz	5.79 Hz	5.63 Hz
2	First Torsion	14.20 Hz	14.05 Hz	14.05 Hz
3	Second Bending	17.00 Hz	17.18 Hz	17.03 Hz
4	In Plane, Fore/Aft	17.60 H	---	17.29 Hz
5	Second Torsion	29.32 Hz	29.33 Hz	29.89 Hz
6	Third Bending	43.04 Hz	---	43.37 Hz

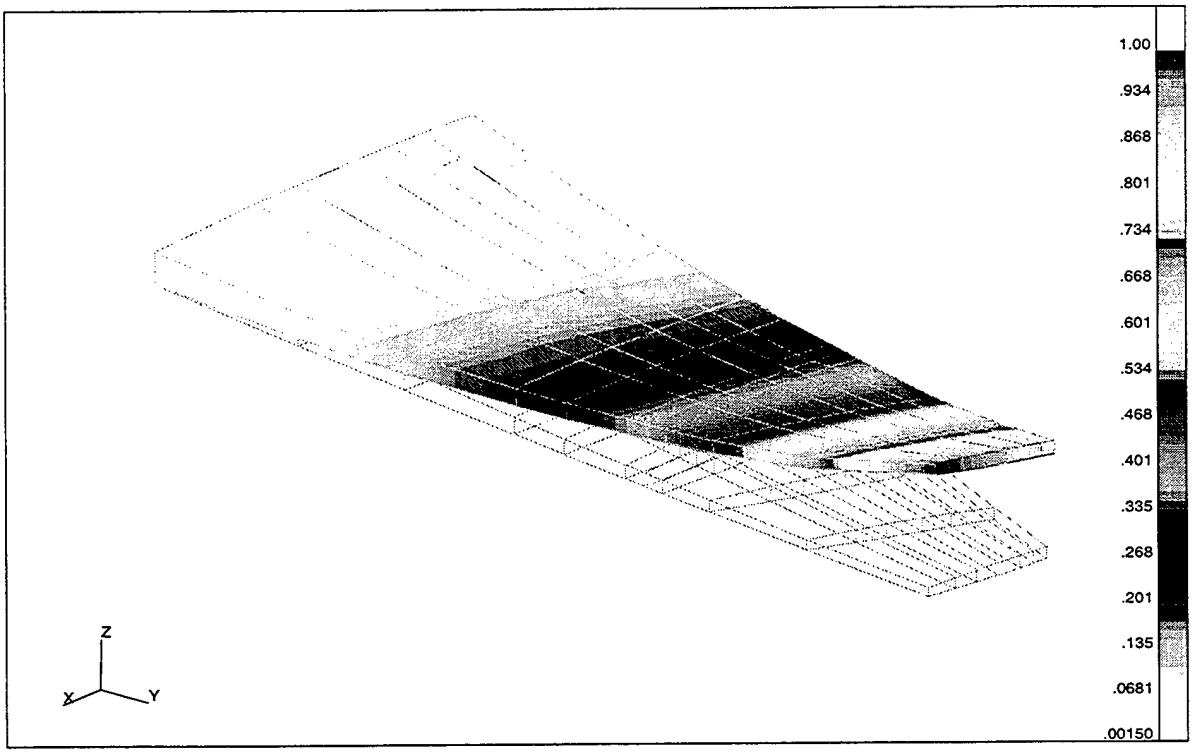

Figure 48 - Mode 1

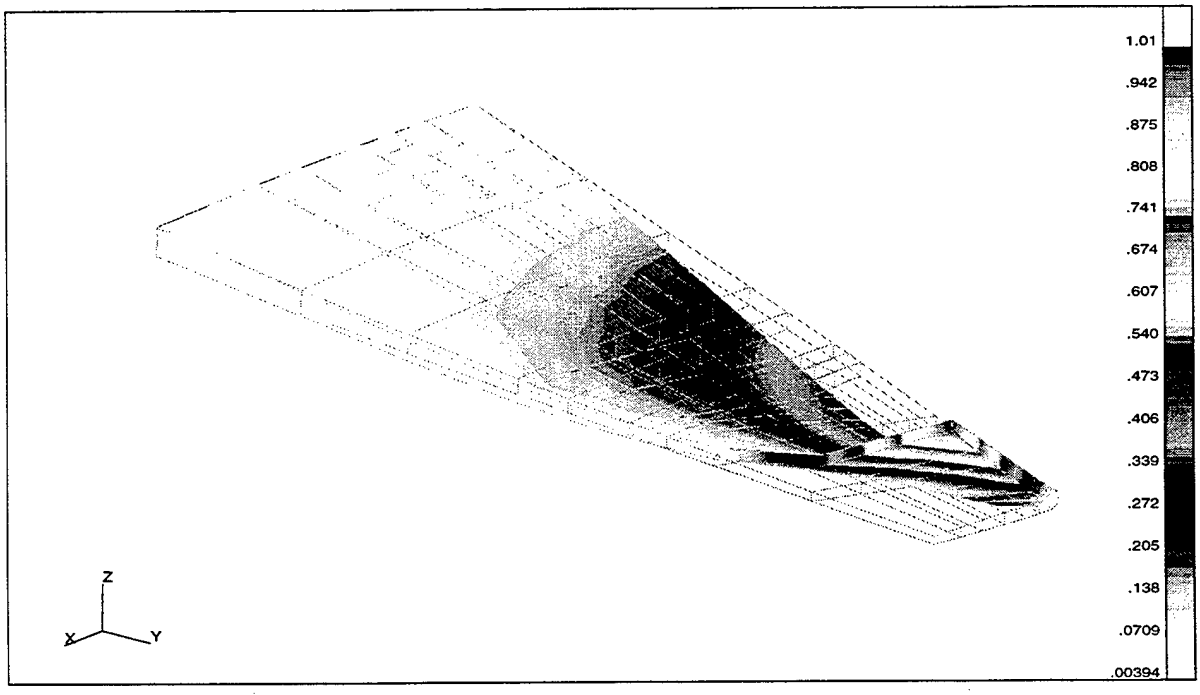

Figure 49 - Mode 2

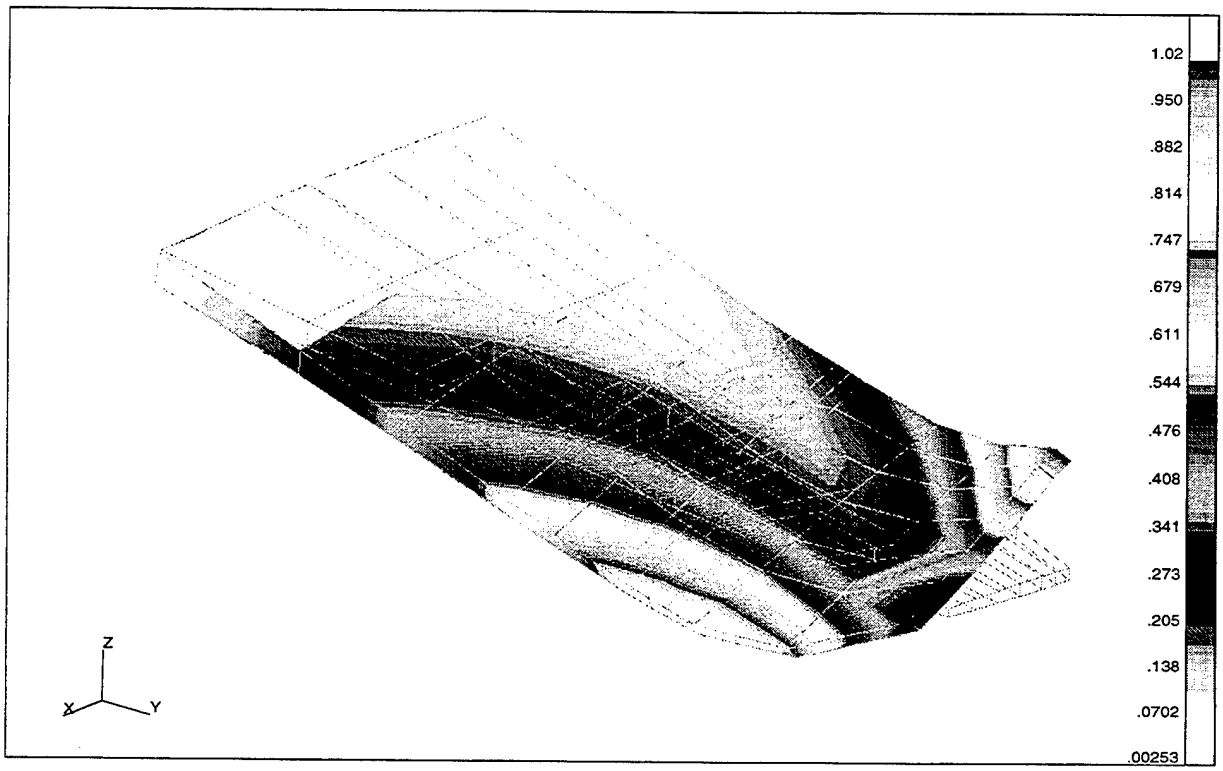

Figure 50 - Mode 3

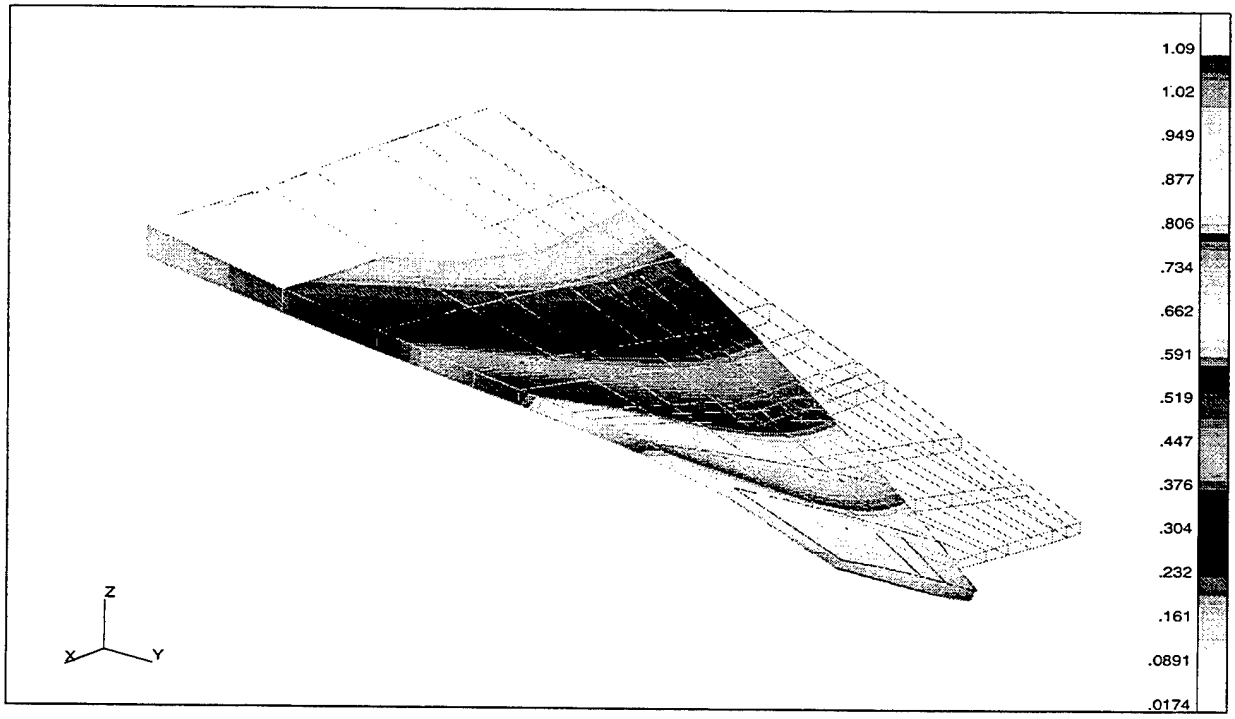

Figure 51 - Mode 4

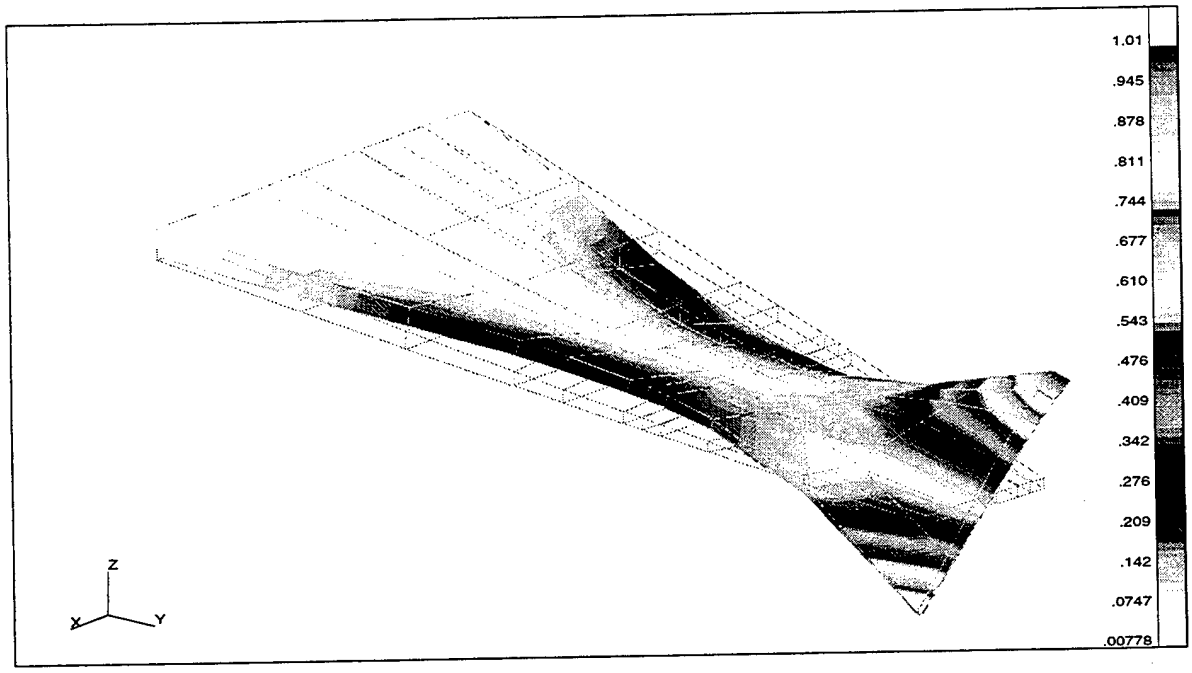

Figure 52 - Mode 5

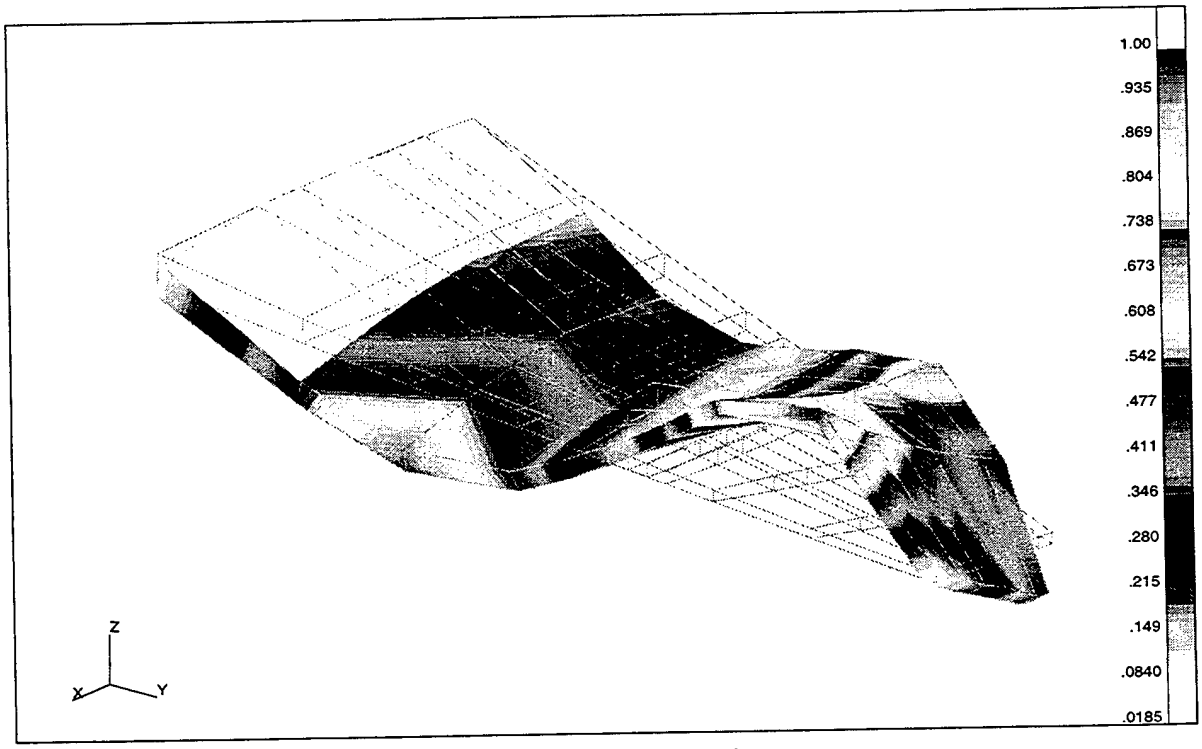

Figure 53 - Mode 6

Since the weight of the built up structure is already known, changing the objective function to optimize to that weight would be ideal. ASTROS 12 does have the capability to define the objective function and optimize to a given weight, however it requires that all elements with density be added together to determine the weight of the structure. Due to the complexity of the FEM, it was decided not to pursue the tedious task of adding together every element with density for two reasons. First ASTROS 12 has had limited validation. Second was due to the lack of any mass distribution data of the wing. It was not possible to accurately issolate structural and non-structural mass.

Another possibility would have been to use ASTROS ID. This is a code which optimizes based upon nodal lines for the different modes. However due to lack of any actual aircraft mode shape data this avenue was not explored. Additionally this would only assist in the dynamic modeling of the wing and not in the static analysis.

Lacking any static deflection, stress, mass distribution, mode shape plots data and limited spar, skin and rib sizing data it was decided to contract with McDonnell Douglas to obtain their assistance in further development of the model to meet its original goals. While waiting to get McDonnell Douglas on contract, through the Structural Technology and Analysis Program (STAP), work continued on the FEM with the hopes that results would prove satisfactory. Since early results and discussions indicated that the lumping or removal of CONM2s along spar #3 was the probable culprit for poor results, work began on various distribution methods for the CONM2s. In a first attempt to solve the localized movement, the mass associated with each CONM2 was divided equally among the top and bottom of spar number #3. No consideration was made to the inertia values. Results were encouraging. However there was no chordwise distribution of the masses as it was uncertain how to distribute the inertia values with no available mass distribution data. The second modification was to scale the mass and inertia associated with each CONM2 to attempt to retain non-structural mass in the CONM2 and use the density associated with the optimized structure to represent structural mass.

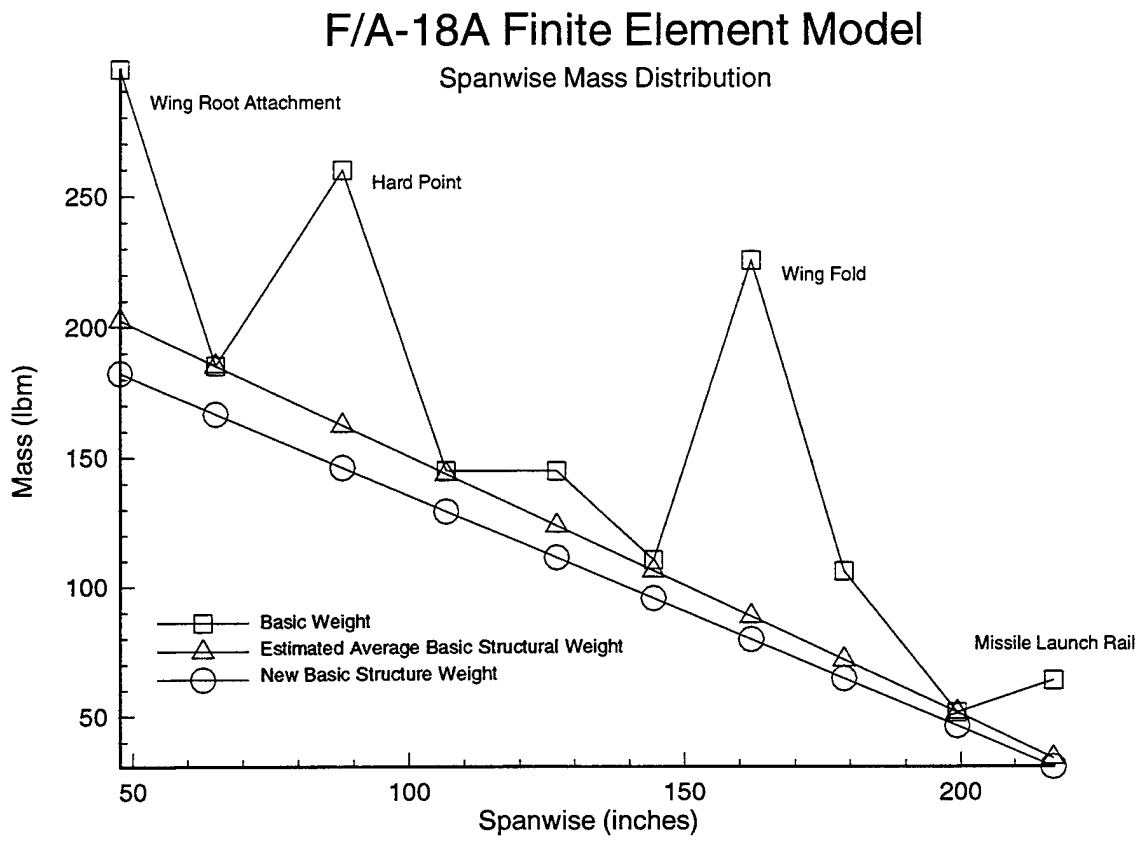

Figure 54

Figure 54 represents the scaling of CONM2s and inertia values. The heavy black line with squares labeled "Basic Weight" is a plot of the CONM2s taken from the beam rod model with "TBOX" extensions. The solid black line with triangles labeled "Estimated Average Basic Structure Weight" is a line drawn between the spanwise locations of 62" and 198". The assumption was that given no wing hard points or wing fold, there should be a linear representation of the wing structural weight. The circles, "New Basic Structure Weight", is a 10 percent reduction of the "Estimated Average Basic Structure Weight." The 10 percent reduction was an accounting of non-structural mass like rivets, wires and tubing. The difference between the "New Basic Structure Weight" and "Basic Structure" became new CONM2s representing both non-structural weight and structural items not currently well modeled like wing hard points and the wing fold. New inertial values were calculated by taking the difference between the "New Basic Structure Weight" and the "Basic Weight" and dividing by the "Basic Weight." This perecentage was multiplied by the original inertia value at each spanwise loctation and placed into the new CONM2 cards. Results of these changes were not incouraging. The three main problems that occured during modal anayses were localized movement of the nodes, mode switching and optimized structure which was still too small and light. There was also an attempt to force the size of the elements to be larger and thus increase the weight by placing lower bounds on the

design constraint cards. Typical values were 0.1 to 1.0 inches thick on the skins (CQUAD4s), 0.5 to 4.0 square inches of area on the spar and rib caps (CRODs) and 0.2 - 0.75 inches thick on the spar and rib shear webs (CSHEARs). In general this did not help as ASTROS then had trouble converging as the model was too stiff given the mass distribution.

Due to the problems and lack of static and dynamic data available to WL, WL/FIBGE contracted with McDonnell Douglas to finish the model. The two tasks for the McDonnell Douglas are to provide initial sizing and mass distribution, Task 1, and correlation of the FEM, Task 2. The initial sizing consists of geometry, average element properties, mass distribution, actuator and control surface attachment and boundary conditions. The correlation is to be done to both ground vibrational testing and flight test data. Goals for the correlation are modal frequencies, static deflections and aileron reversal speeds within +/-5%. Work on Task 1 was completed the week of 20 May 96. Work on Task 2 is contracted to be finished by mid September 1996.

Shown in figure 55 is a finite element representation of the F/A-18 wing model provided by McDonnell Douglas along with the mass properties given in Table 12. The natural frequencies of this built-up model representation are determined for the first eight natural modes in Table 13 along with a comparison of the frequencies obtained from the beam-rod model. The corresponding mode shapes for the built-up model are displayed in Figures 56 through 66 for a comparison of the mode shapes obtained from the beam-rod model and shown in Section IV.

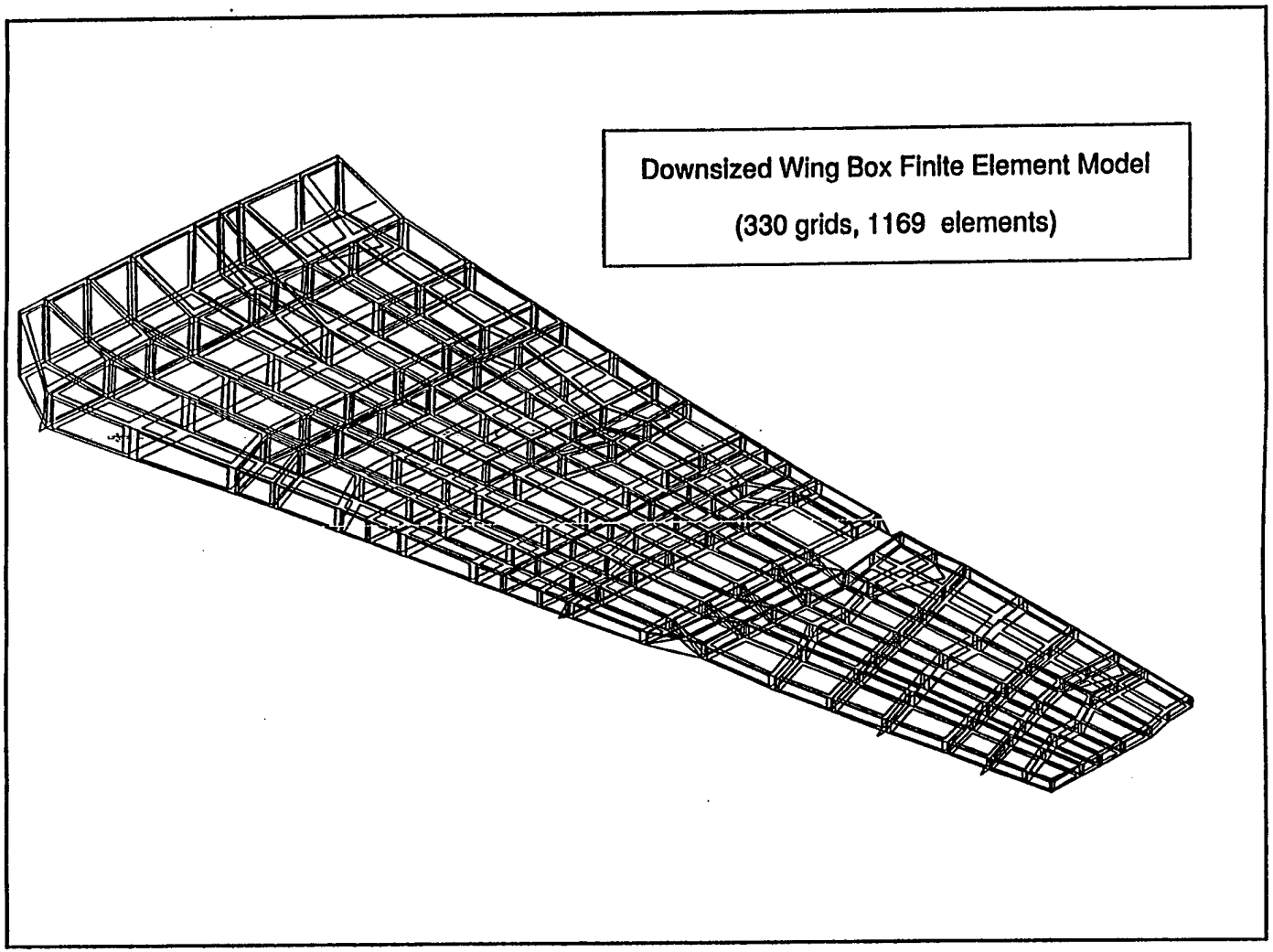

Figure 55: McDonnell Douglas Finite Element Model of F/A-18

Table 12: Wing Sectional Mass Properties

TORQUE BOX STRUCTURE ONLY (WITHOUT CONTROL SURFACES)

SECTION NUMBER	SECTION BOUNDARY Y_W ~ IN	SECTION WIDTH ΔY_W ~ IN	SECTION CENTER Y_W ~ IN	SECTION CHORD(1) c ~ IN	SECTION LEADING EDGE X_{LE} ~ IN	WEIGHT W ~ LB	CENTER OF GRAVITY		INERTIA @ C.G.(2)		w(3) LB/IN	Xcg/c(4) IN/IN	ρ_α/c(5) IN/IN
							Y_W CG IN	X_W CG IN	PITCH ~ I_α LB-IN^2	ROLL ~ I_θ LB-IN^2			
1	43.35- 56.00	12.65	49.68	163.11	22.70	298.30	47.57	102.37	156215	13173	23.581	.490	.140
2	56.00- 76.00	20.00	66.00	153.93	30.90	185.24	65.05	100.04	111460	8324	9.262	.449	.159
3	76.00- 96.00	20.00	86.00	142.69	40.94	259.90	87.94	97.72	111276	11026	12.995	.398	.145
4	96.00-116.00	20.00	106.00	131.44	50.98	145.06	106.69	113.78	41147	4824	7.253	.479	.128
5	116.00-136.00	20.00	126.00	120.19	61.38	144.96	126.76	115.35	49469	5105	7.248	.450	.154
6	136.00-154.00	18.00	145.00	109.51	70.56	110.54	144.35	119.96	33966	3665	6.141	.458	.160
7	154.00-172.00	18.00	163.00	96.39	79.60	225.41	162.10	124.43	46367	7904	12.523	.468	.149
8	172.00-190.00	18.00	181.00	86.46	88.64	106.05	178.89	132.49	21635	3188	5.892	.512	.165
9	190.00-207.00	17.00	198.50	77.71	97.42	51.60	199.33	138.16	8668	1012	3.035	.525	.167
10	207.00-225.5	18.50	216.25	65.78	106.33	64.09	217.07	136.91	14984	2459	3.464	.466	.232
TOTAL	43.35-225.5	182.15	134.43	---	---	1591.14	112.25	112.47	865519	4150360	---	---	---

WING TIP LAUNCHER/MISSILE

LAU-7(6)	225.50-231.25	5.75	229.00	ℓ = 111.00	66.85	89.66	229.00	121.28	64532	242	15.593	0.481	0.242
AIM-9	231.25-236.25	5.00	233.75	ℓ = 113.00	58.07	185.00	233.75	119.33	218554	1729	37.000	0.542	0.3042

WING FUEL

1	43.35- 56.00	12.65	49.68	162.85	24.94	87.40	49.70	94.30	13321	1223	6.909	0.4259	0.0758
2	56.00- 76.00	20.00	66.00	153.86	33.14	128.50	66.10	96.90	22496	4275	6.425	0.4144	0.0860
3	76.00- 96.00	20.00	86.00	142.79	43.18	115.00	85.90	100.20	21384	3832	5.750	0.3993	0.0955
4	96.00-116.00	20.00	106.00	131.74	53.22	92.70	105.80	105.80	14980	3067	4.635	0.3991	0.0965
5	116.00-136.00	20.00	126.00	120.69	63.26	72.10	125.80	111.40	9874	2368	3.605	0.6212	0.0969
6	136.00-158.50	22.50	147.25	108.95	73.93	35.30	145.80	117.00	4262	118	1.569	0.3953	0.1008
TOTAL	43.35-158.50	115.15	100.93	---	---	531.00	88.00	102.10	110387	455913	---	---	---

NOTES: (1) Section Geometry: $c = 190.29 - 0.552382 * Y_W$; $X_{LE} + 0.502073 * Y_W$

(2) Inertia data is in streamwise coordinates (FS, BL, WL) and at the section center of gravity

(3) $w = W/\Delta Y_W$

(4) $Xcg = X_{Wcg} - X_{LE}$

(5) $\rho_\alpha / c = \sqrt{I_\alpha / (W * c^2)}$

(6) Data listed are for missile to tip-rib adapter

Table 13: Comparison of Beam/Rod and Built-Up Model Natural Frequencies

F/A-18 Built-Up FEM

Mode		Frequency (Hz)		Difference
Number	Description	Built-up	Beam/Rod	%
1	W1B	4.63	4.20	4.9
2	W1T	8.66	8.54	0.7
3	W2B	15.89	13.54	8.0
4	L Lat	16.31	---	---
5	TEFR	19.52	23.02	8.2
6	Ail Rot	22.50	---	---
7	W1 F/A B	24.04	14.44	24.9
8	TMB	34.98	32.77	3.3

Figure 56: F/A-18 Wing

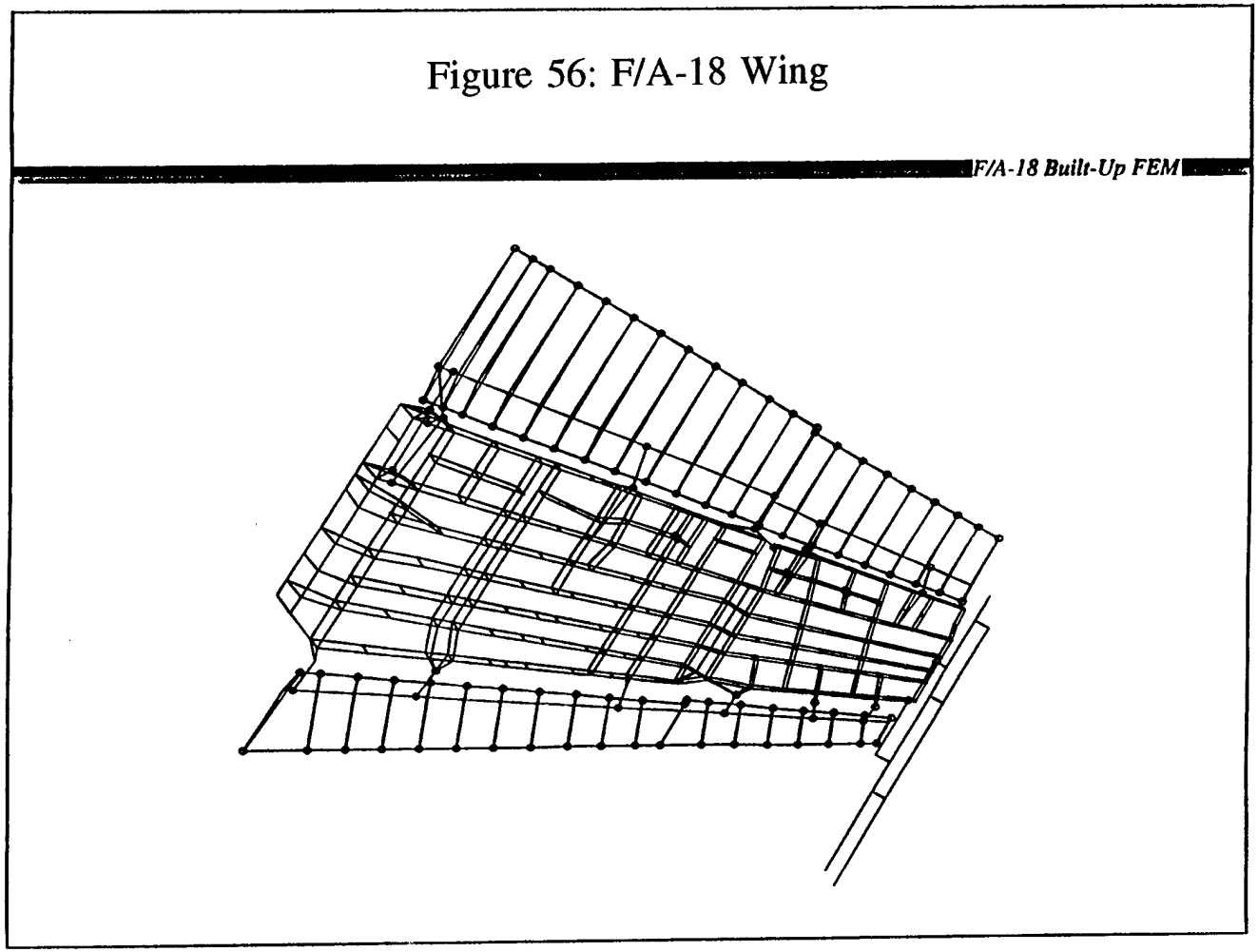

Figure 57 - Mode 1: Wing First Bending

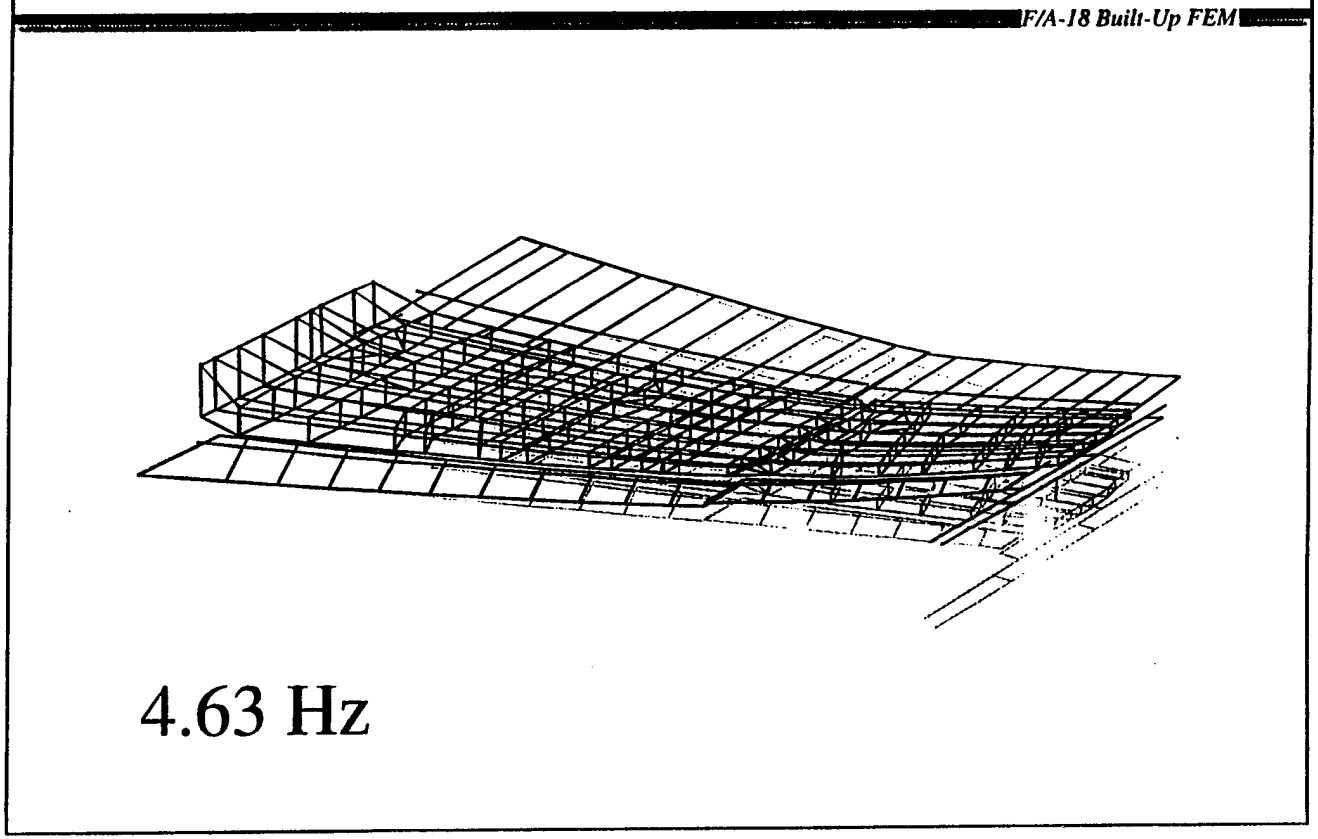

Figure 58 - Mode 2: Wing First Torsion

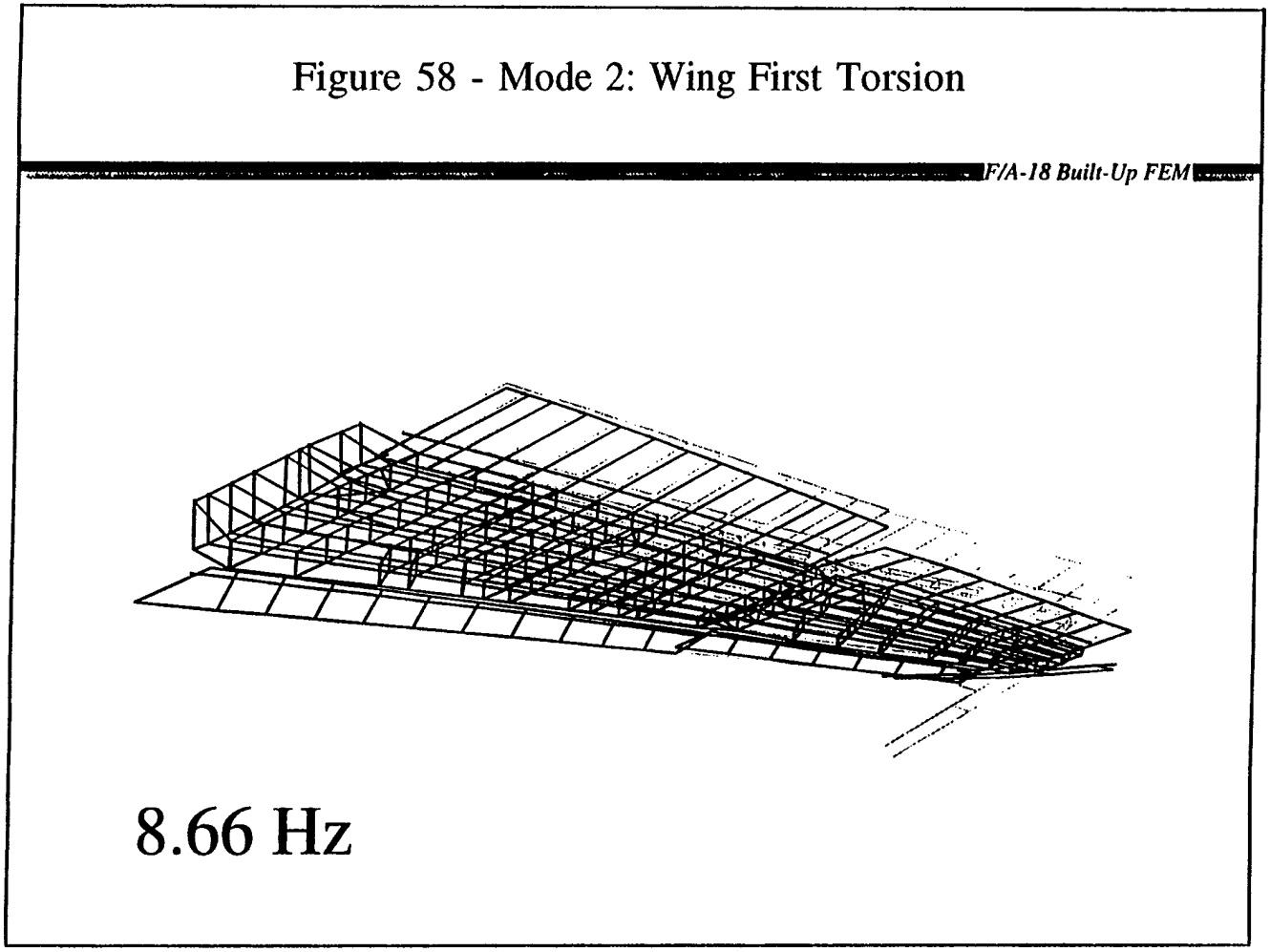

Figure 59 - Mode 3: Wing Second Bending

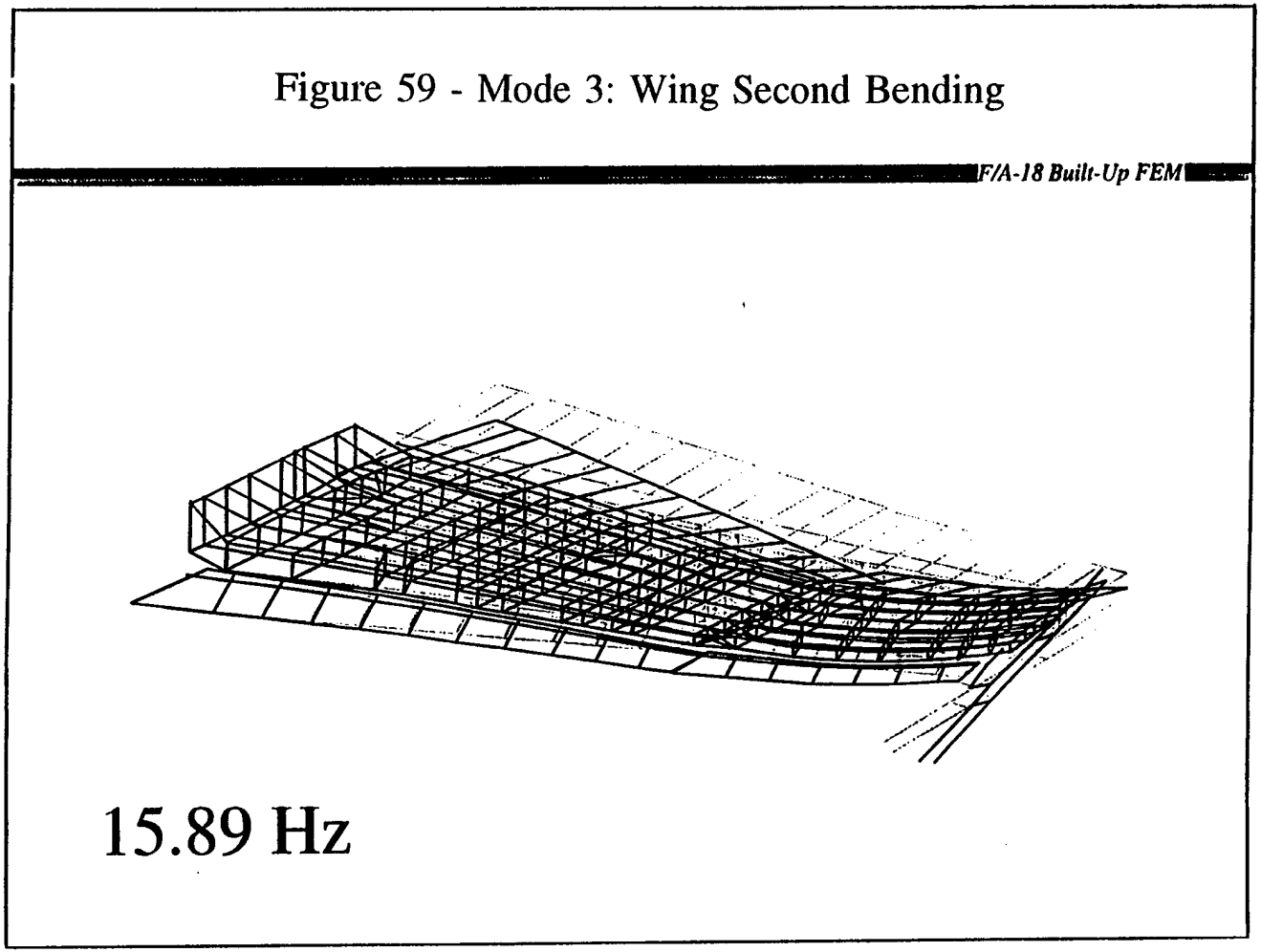

Figure 60 - Mode 4: Launcher Lateral

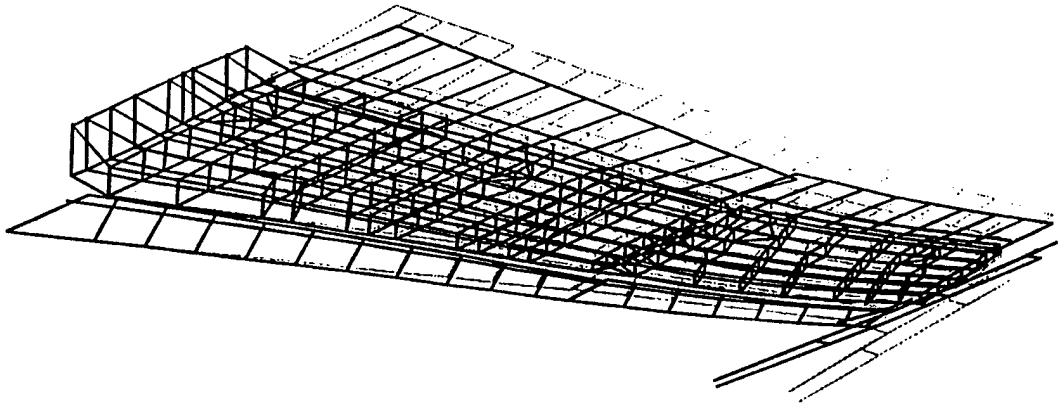

16.31 Hz

Figure 61 - Mode 5: Trailing Edge Flap Rotation

F/A-18 Built-Up FEM

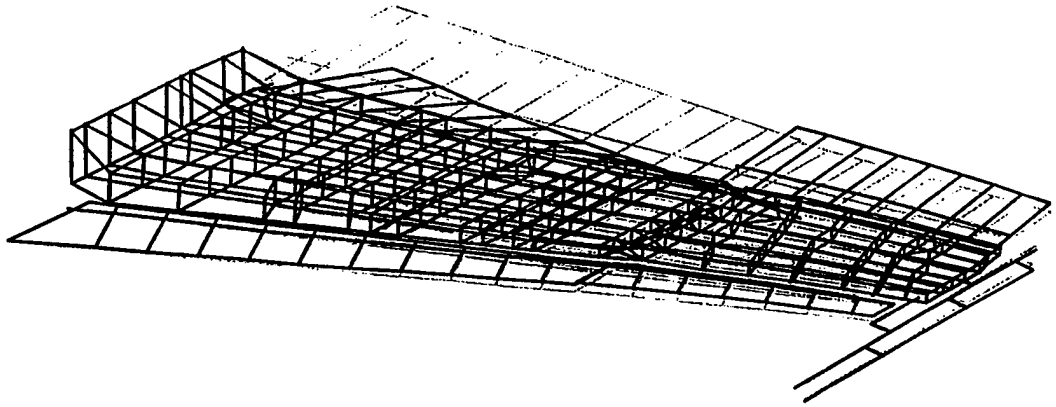

19.52 Hz

Figure 62 - Mode 6: Aileron Rotation

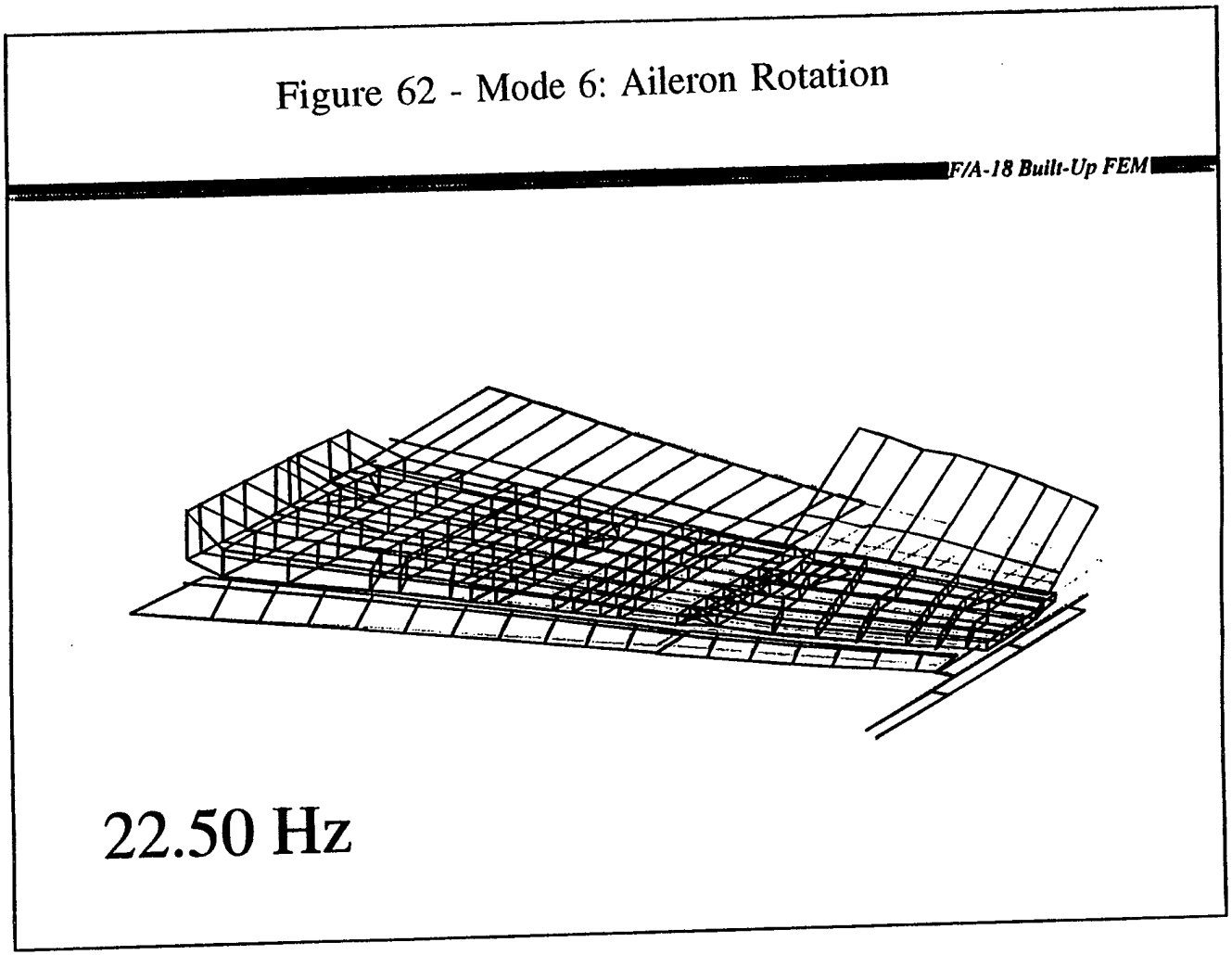

Figure 63 - Mode 7: Wing Fore/Aft Bending

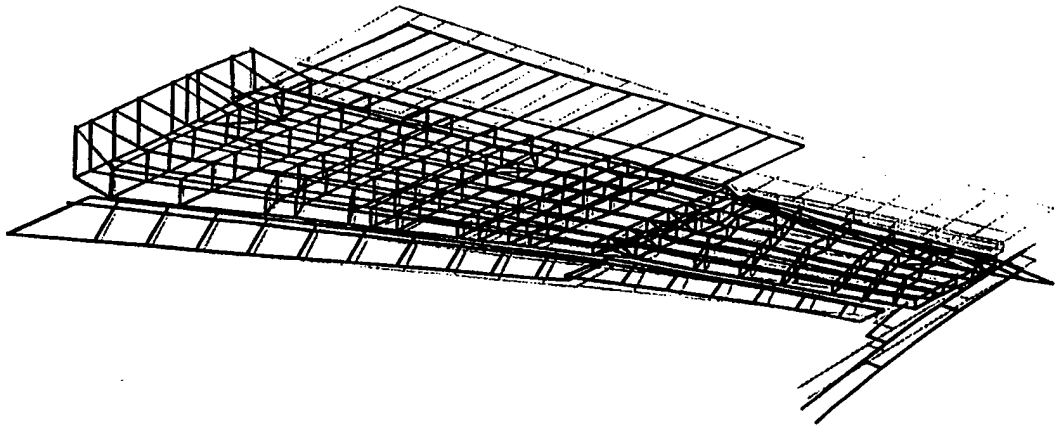

24.04 Hz

Figure 64 - Mode 8: Tip Missile Bending

F/A-18 Built-Up FEM

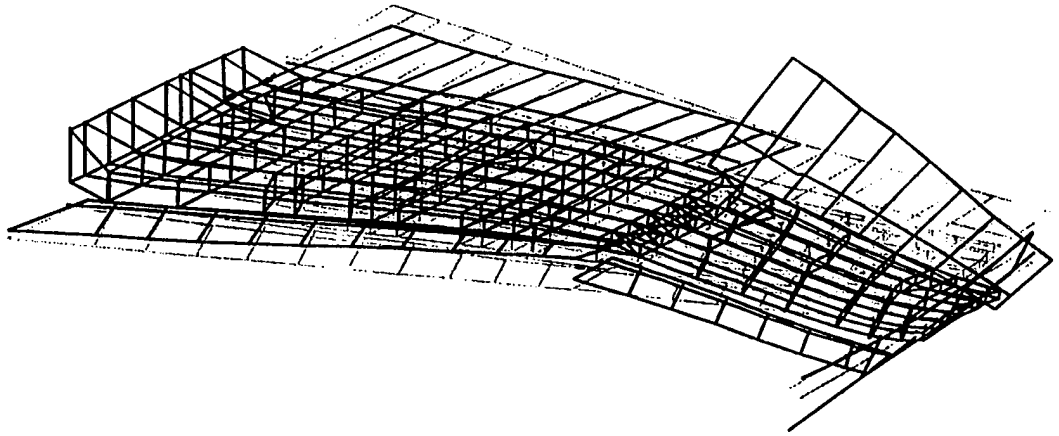

34.98 Hz

Figure 65 - Mode 9: Leading Edge Flap Rotation

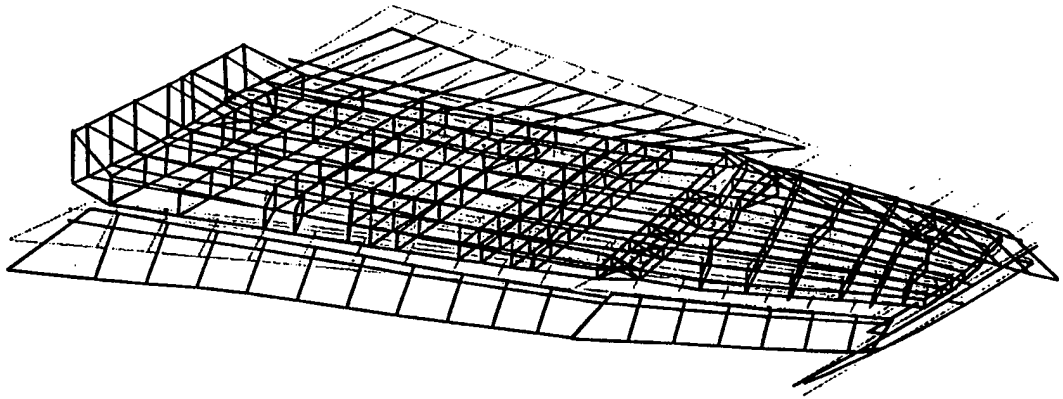

36.91 Hz

Figure 66 - Mode 10: Trailing Edge Flap Bending

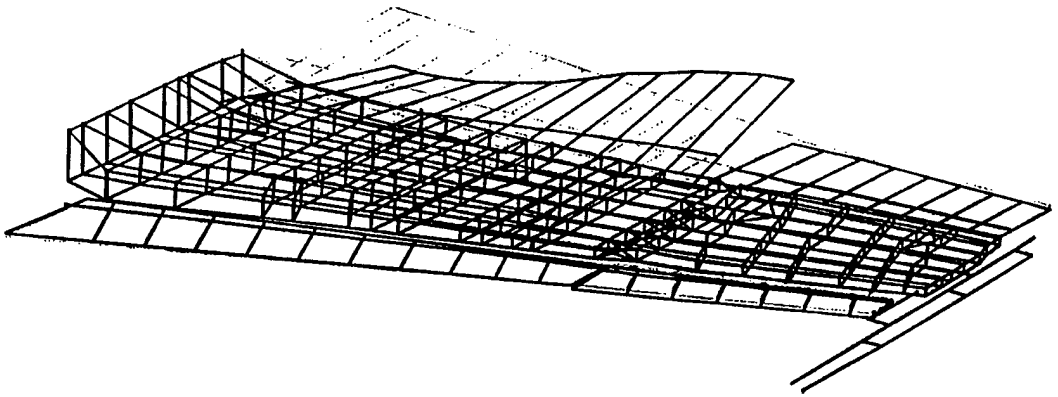

44.04 Hz

SECTION VIII

OPTIMIZATION OF A GENERIC FIGHTER WING INCORPORATING ACTIVE AEROELASTIC WING TECHNOLOGY

Introduction

Aircraft wing designers have used optimization techniques to minimize weight while satisfying constraints for stress/strain, buckling, flutter, and maneuver performance. The first two constraints, stress/strain and buckling, specifically accomplish the structures ability to withstand static aerodynamic loads generated by flight maneuvers, such as a 9g pull-up. The flutter constraint ensures that the dynamic aeroelastic instability due to the interaction of modes with inertial and aerodynamic coupling does not occur in the aircraft flight envelope. The final constraint, although not a critical aircraft safety issue, is an important design measure, such as a fighter aircraft's ability to perform a roll maneuver.

The goal here is to explore the utility of AAW technology by using control surface blending in the preliminary design stage to meet roll performance requirements. A fully built-up finite element model of a generic fighter aircraft wing will be used in this design study. Antisymmetric static aeroelastic analysis of the model with nominal element thicknesses and areas will provide a roll performance baseline using a single trailing edge surface or multiple leading and trailing edge surfaces. Weight optimization of the wing finite element skin, spar-web, and rib-web thicknesses as well as spar-cap and vertical post areas with stress and flutter constraints will show that a lighter weight structure can be achieved utilizing AAW technology to meet roll performance constraints compared with the traditional design methodology of using a single trailing edge outboard control surface.

Analytical Tools

To accomplish the objectives of this study the Automated Structural Optimization System (ASTROS) is used for analysis and optimization studies. ASTROS is a multidisciplinary design tool capable of incorporating static, dynamic, aerodynamic, and aeroelastic disciplines for analysis and optimization of finite element models[6]. ASTROS minimizes the weight of a finite element model while satisfying combinations of constraints: stress, strain, and displacement constraints for the statics discipline; frequency constraints for the modes discipline; flutter velocity constraints for the dynamic aeroelastic discipline; and stress, strain, displacement, control surface effectiveness, and control surface trim deflection constraints for the static aeroelastic discipline. Static aeroelastic analyses are divided into symmetric and antisymmetric subcases. Symmetric static aeroelastic analyses are applied for lift performance, which includes design for lift effectiveness. Antisymmetric static aeroelastic analyses are applied for roll performance, which includes design for aileron effectiveness and control surface trim deflection. Some of the variables for analysis include pitch and roll rate, and control surface deflection. Static aeroelastic studies are limited to a wing, fin, and canard configuration, each of which may have multiple control surfaces defined. Trim is achieved for either symmetric or antisymmetric analyses when the inertial, elastic, and aerodynamic forces and moments are in equilibrium. In previous versions of ASTROS, when trimming for roll, only one variable could be 'free' for

solution of this equation; therefore, at most one control surface deflection could be utilized as a variable for antisymmetric trim analyses or optimization. The inability of previous versions of ASTROS to utilize multiple control surfaces for aircraft trim is addressed through a trim module augmentation.

To address this issue, under contract with the USAF, Northrop Grumman created an enhanced trim module for ASTROS called the Adaptive Multidimensional Integrated Controls (AMICS) module. AMICS incorporates a subset of Northrop Grumman's 'Generic Control Law' for conceptual and preliminary design[10]. This algorithm automates control surface blending based on aircraft stability and control derivatives for trim and transient maneuvering. Control surface scheduling and limiting are also incorporated into the design. Constraints which are input by the user include: control surface physical position limits, dynamic pressure limits, hinge moment limits, and scheduling of control surface deflections by Mach number versus angle of attack. Trim is achieved by the equilibrium of the inertial, elastic, and aerodynamic forces and moments. There can be an unlimited number of control surfaces defined; therefore, there can be an infinite number of possible surface deflections which satisfy equilibrium. Because of more unknowns than equations, trim is iteratively solved using the Newton-Raphson method which produces minimal actuator command signals. This method requires the derivatives of the forces and moments with respect to angle of attack, sideslip angle, and generalized roll, pitch, and yaw controller values. The end result is the minimum blended deflections of multiple control surfaces which satisfies equilibrium.

Theoretical Background

All analysis and optimization studies are performed within the ASTROS environment. The optimization procedure utilizes a mathematical programming method, the Method of Modified Feasible Directions[6], to find the set of design variables (element thicknesses and areas) which minimize the objective function (weight), subject to constraints from the various disciplines. Also, the design variables are constrained by upper and lower bounds. For static aeroelastic analysis, ASTROS uses a linear panel method to determine the aerodynamic loads, and the finite element method to determine the structural response. Standard surface and beam splining techniques are applied to transfer the aerodynamic loads from the aerodynamic grid points to the structural grid points. The program's static aeroelastic analysis discipline is employed to generate control and stability derivatives, which are used to generate control surface effectiveness values, as well as to solve the roll equation of motion for control surface trim deflections.

Optimization

The constrained optimization problem is formally stated as follows:

Find the set of n design variables, $\underline{X}$, which minimizes or maximizes

$$F(\underline{X}) = F(x_1, x_2, \ldots, x_n) \tag{20}$$

subject to the inequality constraints,

$$g_i(\underline{X}) = g_i(x_1, x_2, \ldots, x_n) \leq \bar{g}_i, \; i=1,2,\ldots,k \tag{21}$$

the equality constraints,

$$g_i(\underline{X}) = g_i(x_1, x_2, \ldots, x_n) = \bar{g}_i, \; i=k+1,k+2,\ldots,k+p \tag{22}$$

and the upper and lower bounds on the design variables

$$\underline{X}^L \leq \underline{X} \leq \underline{X}^U \tag{23}$$

The finite element physical parameters of thickness and area are the design variables. The objective function, $F(\underline{X})$, is the weight of the designed elements. In this paper, the constraints are the element stresses due to static loads, the flutter velocity, and the trimmed control surface deflections.

Steady Aerodynamics

The Unified Subsonic And Supersonic Aerodynamic Analysis (USSAERO) algorithm is utilized by ASTROS[6] for the computation of aerodynamic loads on the aircraft structure. For a lifting surface, this approach uses a superposition of vortex singularities applied to a discrete number of aerodynamic panels to calculate the pressure distribution about the surface. The algorithm is capable of accounting for wing thickness and camber effects through the boundary conditions. The basic equation is:

$$[A]\{\gamma\} = \{\omega\} \tag{24}$$

where the singularity values, $\{\gamma\}$, are obtained knowing the velocities due to a prescribed boundary condition, $\{\omega\}$, and the normal velocity influence coefficients, $[A]$. Once the singularities have been determined, velocity components are computed and the pressure coefficients at each of the panels are calculated. The pressure coefficients are converted to forces which in turn yield the rigid aerodynamic loads.

The aerodynamic influence coefficient matrix, $[AIC]$, is generated to calculate the incremental loads due to structural deformations. This matrix calculation is:

$$[AIC] = -4S[U][A]^{-1} \tag{25}$$

where S is the aerodynamic surface area, and the matrix $[U]$ is the velocities on the wing panel due to singularities on the wing. The aerodynamic influence coefficient matrix is important for the formulation of the equilibrium equation.

Static Aeroelastic Analysis

The static aeroelastic features in ASTROS provide the capability to analyze and optimize linear structures in the presence of steady aerodynamic loading. The equation of equilibrium is:

$$[M]\{\ddot{x}\} + ([K] - [A_f])\{x\} = [A_r]\{\delta\} \tag{26}$$

where $[M]$ is the mass matrix, $[K]$ is the structural stiffness matrix, $[A_f]$ is the aerodynamic stiffness matrix due to structural displacements, $[A_r]$ is the aerodynamic stiffness matrix due to control surface deflections, $\{x\}$ is the nodal displacement vector, and $\{\delta\}$ is the control surface deflection vector. The aerodynamic stiffness matrices, $[A_f]$ and $[A_r]$, are generated from the aerodynamic influence coefficient matrix, $[AIC]$.

Since roll performance is the focus of this study, antisymmetric analysis is employed. Stability and control derivatives, or sensitivities of the rolling moment coefficient, C_M, with respect to the roll rate, C_{M_p}, and control surface deflections, C_{M_δ}, respectively, are calculated from the aerodynamic stiffness matrices.

A convenient way of quantifying the ability of a particular control surface to generate rolling moments is through the control surface effectiveness parameter, ε. This value is defined as the ratio of a flexible control surface stability derivative to the flexible roll damping stability derivative. Thus there are n control surface effectiveness values given by:

$$\varepsilon_i = -\frac{C_{M_{\delta_i}}}{C_{M_p}}, \; i=1,\ldots,n \tag{27}$$

By this definition, control surface reversal occurs when the control surface effectiveness changes signs. In general for increasing dynamic pressure, the effectiveness of a trailing edge control surface will change from positive to negative indicating roll reversal. In the examples studied during this effort, effectiveness values were determined as a function of dynamic pressure, thereby indicating the usefulness of each control surface over a range of flight conditions.

Another analysis technique utilized in these studies was the determination of control surface deflections required to achieve a desired roll rate. The static trim equation for roll:

$$qSb\left[\sum_{i=1}^{n} C_{M_{\delta_i}}\delta_i + C_{M_p}\frac{pb}{2V_0}\right] = I_{roll}\dot{p} \tag{28}$$

where q is the dynamic pressure, b is the wing span, δ is the control surface deflection, p is the roll rate, V_0 is the free stream velocity, I_{roll} is the rolling moment of inertia, and $\dot{p}$ is the roll acceleration. This equation has a unique solution for only one unknown variable, which is determined by the user. This variable is either a control surface deflection, the roll rate, or the roll acceleration.

The current problems explored are simplified by the assumption of constant roll rate. In terms of control surface efficiencies, the trim equation is given by:

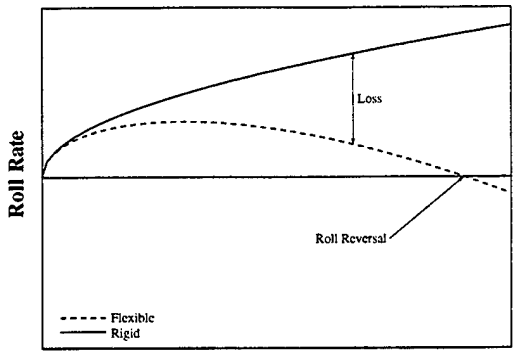

Figure 67: Comparison of Flexible and Rigid Roll Rates for Trim, Given Aileron Deflection

$$\sum_{i=1}^{n} \varepsilon_i \delta_i = \frac{pb}{2V_0} \tag{29}$$

This equation for trim is further explored by considering a typical wing with only one control surface, an aileron, available for trim. By specifying a control surface deflection, and solving for roll rate over a range of dynamic pressures, the loss of ability of an aileron on a flexible wing to produce a required roll rate can be seen in figure 67. Roll reversal behavior is seen where the roll rate goes from positive to negative for a defined control surface deflection.

Another method to examine this deficiency of an aileron on a flexible wing can be explored by specifying a required roll rate and solving for the deflection necessary for trim. The asymptotic behavior of the aileron deflection is illustrated in figure 68. The aileron deflection approaches infinity as roll reversal dynamic pressure is approached.

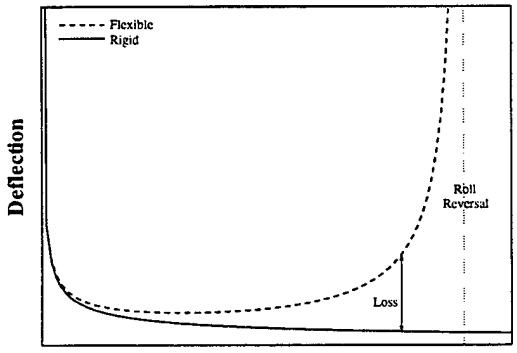

Figure 68: Comparison of Flexible and Rigid Aileron Deflections for Trim, Given Constant Roll Rate

Blended Control Surface Trim

For a single control surface, the solution for trim in equation (10) is trivial. For multiple control surfaces, however, there exists an infinite number of solutions for the single equation. The Adaptive Multi-Dimensional Integrated Controls (AMICS) enhanced trim module, developed under Air Force contract with Northrop Grumman, provides the capability to determine a unique solution. The AMICS module takes the sum total of inertial, elastic, and aerodynamic forces and moments acting on the aircraft and defines trim to be achieved when this sum is zero. The Newton-Raphson method is used to solve the equations. This method is an iterative scheme based on a minimum control energy criteria in which the effectiveness of each control surface is taken into account. The derivatives of the rolling moment with respect to generalized roll controller values for each control surface provides the search directions. In effect this procedure minimizes the overall control surface actuator command signals, enabling a roll maneuver to be performed using the minimum amount of control surface deflections.

Example: Generic Fighter Aircraft Wing

To demonstrate the general advantages of using AAW technology to achieve desired roll performance in the design of aircraft, a built-up finite element model of a generic fighter aircraft wing is optimized for minimum weight under stress constraints from a symmetric pull-up load, antisymmetric control surface deflection constraints for a given roll rate requirement, and a flutter velocity constraint.

Structural and Aerodynamic Model

A built-up finite element model of a generic fighter aircraft wing[13] is used to demonstrate the general advantages of using AAW technology to achieve desired roll performance. The finite element model of the wing box structure is shown in figure 69. The wing box is fully enclosed with upper and lower skins, eight ribs, and three spars. The upper and lower skins (64 elements) are modeled by quadrilateral and triangular elements with membrane stiffness. The spar webs (23 elements) and rib webs (32 elements) are modeled by quadrilateral shear elements, and the spar caps (46 elements) and vertical posts (40 elements) are modeled by rods. The structure is assumed to have material properties of aluminum, with $E=10.5\times10^6$ psi, $G=4.04\times10^6$ psi, and $\nu=0.3$.

The generic fighter aircraft wing also has non-structural masses which represent the fuselage, fuel, actuators, and other non load bearing components. The fuselage is represented by a 10,000 lb. mass at the center of the wing root. The wing has 420 lbs. of non-structural mass distributed on the ribs near the wing root and along the fore and aft spars.

The structure and aerodynamic planform are shown in figure 70. The wing aerodynamic planform is swept back 26^o at the quarter chord, with a 90 in. root chord, 48 in. tip chord, and a 108 in. semi span. The leading edge control surfaces have 18% chord width and each cover 50% of the span. The trailing edge control surfaces have 25% chord width with the inboard control surface extending to 60% of the span and the remaining 40% covered by the outboard control surface. The four control surfaces are referred to as leading edge inboard (LEI), leading edge outboard (LEO), trailing edge inboard (TEI) and trailing edge outboard (TEO) surfaces. The wing box is

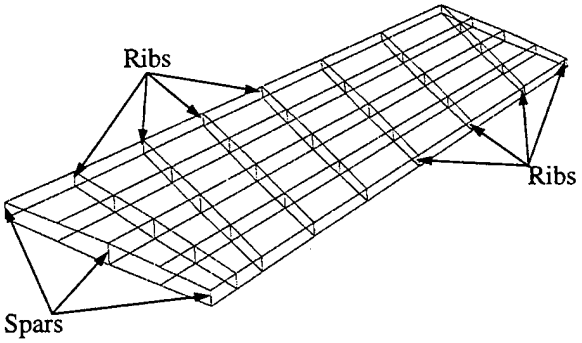

Figure 69: Finite Element Model of the Generic Fighter Aircraft Wing

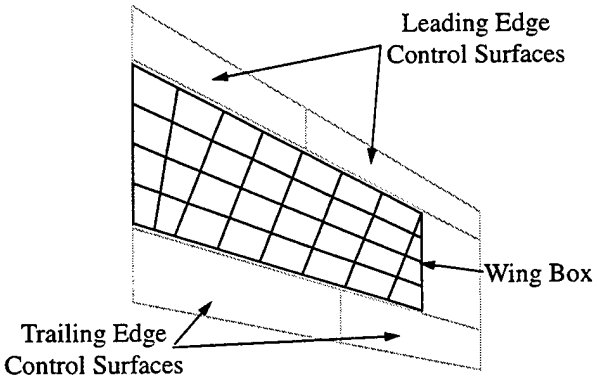

Figure 70: Diagram of Generic Fighter Wing Structural and Aerodynamic Model

positioned within the aerodynamic planform such that the structure does not overlay any of the control surfaces.

Analysis and Optimization Parameters

The aerodynamics of the analysis and optimization of the generic fighter aircraft wing are represented at subsonic (Mach 0.9) and supersonic (Mach 1.2) conditions. The symmetric airloads of the pull-up maneuver are scaled by a loading factor (9g, 6g, etc.) of the total finite element model weight, at an assumed dynamic pressure of 15 psi. The roll rate for the antisymmetric roll maneuver is assumed to be 90 deg./sec. Flight conditions of sea level are assumed for the doublet lattice unsteady aerodynamics used in the P-K flutter solution.

There are a total of 87 design variables for optimization: the top and bottom skin elements are linked to represent 32 variables, each spar web element is independent for 23 variables, the four

rib web elements of each rib is linked to represent 8 variables, the top and bottom spar cap elements are linked for 23 variables, and all the vertical post elements are linked to represent 1 variable. The design variables representing skin, spar web, and rib web thicknesses are constrained between 0.02 in. and 1.0 in. The spar caps and vertical posts are constrained between 0.2 in. and 10.0 in.

Von-Mises stress constraints were applied to the symmetric pull-up loads with the stress limits assumed for aluminum to be: 6.7×10^4 psi tensile, 5.7×10^4 psi compressive, and 3.9×10^4 psi shear. The control surfaces were limited to 5^o deflections for the roll maneuver requirement. The flutter velocity was constrained at a minimum of 16,500 in/sec, which is approximately the corresponding air speed for 15 psi dynamic pressure at sea level air density.

The constraints associated with the optimization of the generic fighter wing were categorized to effect a methodical review of the potential weight savings associated with active aeroelastic wing technology. Category I studies are constrained only for the stress associated with the symmetric pull-up load. Category II studies are constrained for stress and aileron deflection. And Category III studies are constrained for stress, aileron deflection, and flutter velocity.

Analysis of the Nominal Configuration

The nominal configuration assumes skin, spar web, and rib web thicknesses of 0.1 in., and spar cap and vertical post areas of 1.0 in^2. With these design variable values, the wing structural weight is 164 lb. The nominal configuration is used as a basis of comparison for the optimization studies in each category.

The nominal configuration was analyzed for stresses due to a 9g pull-up maneuver, trailing edge outboard control surface reversal dynamic pressure, and flutter velocity. The nominal configuration failed the allowable stress limits (at Mach 0.9 and 1.2) for tension and compression in the skins, spar webs, and spar caps at the root of the wing. All four control surfaces' effectiveness are illustrated for Mach 0.9 in figure 71 and for Mach 1.2 in figure 72. From these figures the TEO reversal dynamic pressure is shown for Mach 0.9 to be 26.1 psi and for Mach 1.2 to be 22.0 psi. The flutter velocities were determined to be 22,058 in/sec at Mach 0.9, and 30,873 in/sec at Mach 1.2.

Some general remarks can be made about the control surface effectiveness values in both subsonic and supersonic regimes from figures 71 and 72. As dynamic pressure increases, the leading edge control surfaces' effectiveness increases whereas the trailing edge control surfaces' effectiveness decreases. The leading edge outboard control surface is the most effective control surface at high dynamic pressures. The trailing edge control surfaces' effectiveness eventually changes from positive to negative, which indicates roll reversal.

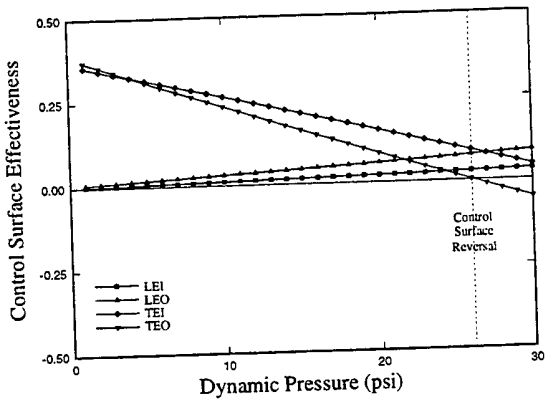

Figure 71: Control Surface Effectiveness, Initial Design
Variable Configuration, Mach 0.9

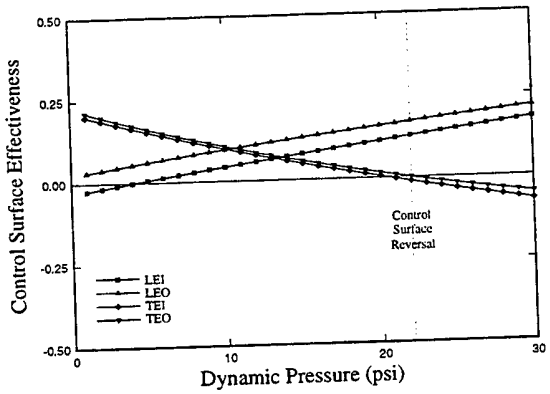

Figure 72: Control Surface Effectiveness, Initial Design
Variable Configuration, Mach 1.2

Deflections of the aircraft control surfaces for roll performance are illustrated for Mach 0.9 in figure 73 and for Mach 1.2 in figure 74. Both figures show the control surface deflections required

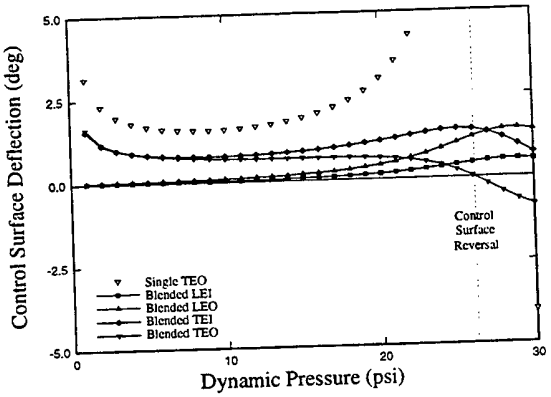

Figure 73: Trim for 90 deg/sec Roll Rate, Initial Design
Variable Configuration, Mach 0.9

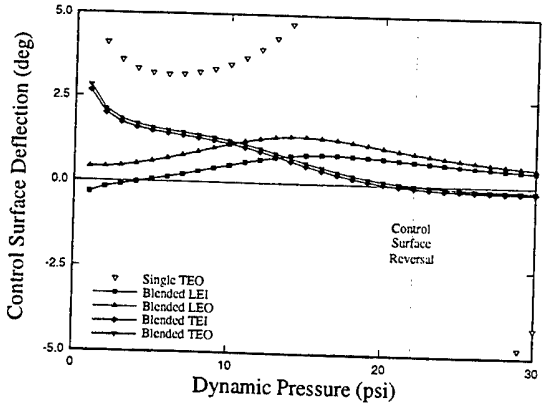

Figure 74: Trim for 90 deg/sec Roll Rate, Initial Design Variable Configuration, Mach 1.2

for 90 deg/sec roll rate utilizing a single TEO surface and multiple control surfaces. In both figures, the single trailing edge outboard surface deflection asymptotically approaches infinity as the dynamic pressure nears the reversal point. For multiple control surface trim, the blended trailing edge outboard control surface deflection is zero at the reversal point and roll trim is effected by the remaining control surfaces. Figures 73 and 74 also show that across the dynamic pressure range the control surface with the greatest effectiveness is utilized with the corresponding largest deflection. The magnitudes of the deflections of the blended control surfaces are less than that of the single surface, and the multiple surfaces are able to maintain roll performance throughout the entire dynamic pressure envelope.

Category I Studies

The generic fighter aircraft wing with the initial element sizes from the nominal configuration was optimized for minimum weight with stress constraints for the aerodynamic loading due to a symmetric pull-up maneuver. The wing was optimized under 9g, 6g, 3g, and 1g loading at Mach 0.9 and 1.2, at 15 psi dynamic pressure. The optimized design variables of the resulting configurations had several notable trends, with the exception of the 1g load case in which almost all of the elements were reduced to minimum values. In each load case, the areas of the vertical posts and the leading edge spar caps went to minimum gage, 0.2 in^2 area. The middle and trailing edge spar caps went to minimum area at the wing tip, increasing in size along the spar, with the largest areas at the root. The skin at the wing tip trailing edge and the aft spar web towards the wing tip decreased thickness to minimum gage, 0.02 in. The largest skin and spar web thicknesses remained at the leading edge near the wing tip and at the middle and aft portions of the wing root. The rib webs remained relatively consistent in thickness. The resulting configurations show that the middle spar carries much of the bending load and the skins carry most of the twisting load.

The four resulting configurations were then analyzed for roll reversal dynamic pressure and flutter velocity. The comparison of static and dynamic aeroelastic quantities and wing final weight is displayed in Table 14.

For the configuration resulting from the optimization with a 9g pull-up maneuver load, all four

control surfaces' effectiveness are illustrated for Mach 0.9 in figure 75 and for Mach 1.2. in figure

Table 14: Comparison of Category I Optimization Results

Load Case	q_{rev} (psi)		V_f (in/sec)		Weight (lb)
	Mach 0.9	Mach 1.2	Mach 0.9	Mach 1.2	
9g	13.9	11.7	17,249	20,180	139.7
6g	10.8	9.1	15,073	17,481	96.1
3g	7.6	6.4	12,626	14,970	55.0
1g	5.3	4.5	10,614	13,534	33.4

76. The figures show similar trends as those in figures 71 and 72 for the nominal configuration.

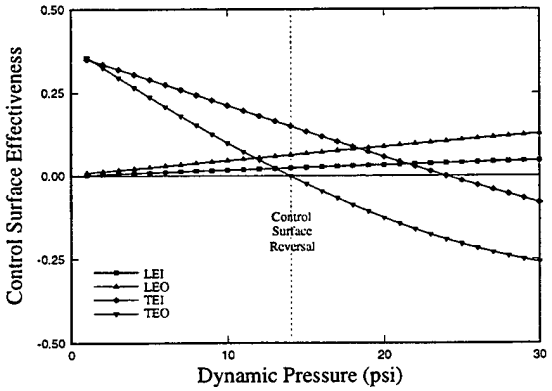

Figure 75: Control Surface Effectiveness, Category I Optimized (9g load) Configuration, Mach 0.9

The most apparent differences are that the leading edge surfaces have slightly higher effectiveness at high dynamic pressures than the initial configuration, and the trailing edge surfaces'

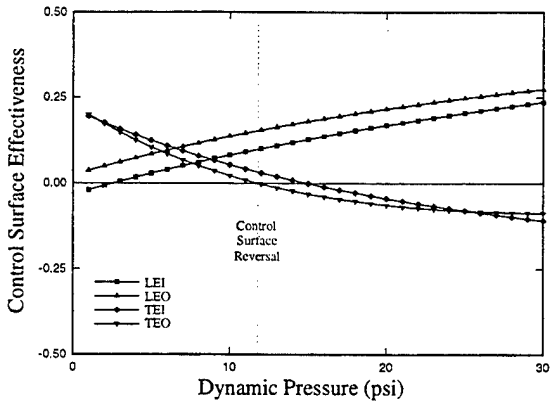

Figure 76: Control Surface Effectiveness, Category I Optimized (9g load) Configuration, Mach 1.2

effectiveness changes from positive to negative at a much lower dynamic pressure. These trends indicate that the wing resulting from the Category I optimization exhibits greater chordwise flexibility than the nominal configuration.

Deflections of the aircraft control surfaces which meet the roll requirement are illustrated for Mach 0.9 in figure 77, and for Mach 1.2 in figure 78. The control surface deflection trends are similar to those of the nominal configuration shown in figures 73 and 74. For both the subsonic and supersonic regimes, the magnitudes of control surface deflections at low dynamic pressures are slightly larger for the Category I configuration than the nominal configuration. For higher dynamic pressures the control surface deflections tend to be smaller for the Category I configuration. These differences are a result of the increase in chordwise flexibility of the optimized wing compared to the nominal design.

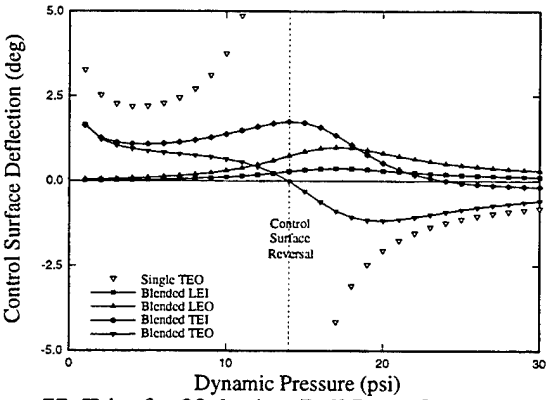

Figure 77: Trim for 90 deg/sec Roll Rate, Category I Optimized (9g load) Configuration, Mach 0.9

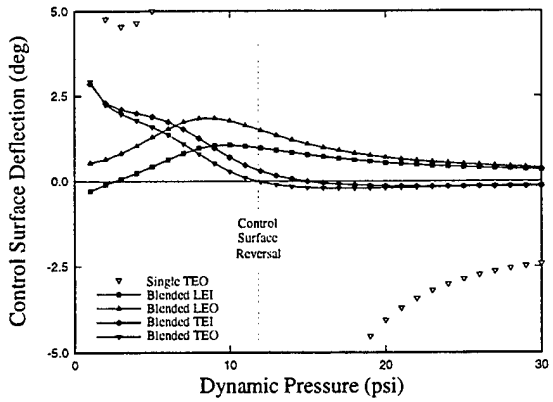

Figure 78: Trim for 90 deg/sec Roll Rate, Category I Optimized (9g load) Configuration, Mach 1.2

Category II Studies

The generic fighter aircraft wing with the initial element sizes from the Category I (9g load) configuration was optimized for minimum weight with control surface deflection constraints for roll performance requirement as well as the stress constraints for the 9g aerodynamic load. The deflection constraint for the single trailing edge outboard control surface is 5 degrees at 15 psi which approximates the performance of the initial configuration as shown in figure 74. To adequately explore the limits of constraints for multiple control surfaces, only the leading edge and trailing edge outboard control surfaces were used to meet the roll requirement, and were constrained to 5 degree magnitude deflections in the region of 10 to 20 psi dynamic pressure.

The optimized configuration for the single trailing edge outboard control surface constraint weighs 152.1 lbs. The final design variables show an increase in the thicknesses of the skins, spar webs, and rib webs, and a decrease in the areas of the spar caps. These final design values suggest that the chordwise stiffness was increased from the initial design and the skins also carry more of the bending load.

The resulting configuration was then analyzed for static and dynamic aeroelastic quantities. The wing reversal dynamic pressure was found for Mach 0.9 to be 27.6 psi and for Mach 1.2 to be 22.6 psi. The flutter velocities were determined to be 23,714 in/sec at Mach 0.9 and 29,262 in/sec at Mach 1.2. These static and dynamic aeroelastic results are very similar to those of the nominal configuration. These analyses indicate that the increase in chordwise stiffness of the wing was due to the single control surface deflection constraint.

Deflections of the aircraft control surfaces which meet the roll requirement are illustrated for Mach 1.2 in figure 79. The figure shows that roll performance can be achieved with multiple

surfaces using smaller deflections throughout the dynamic pressure envelope.

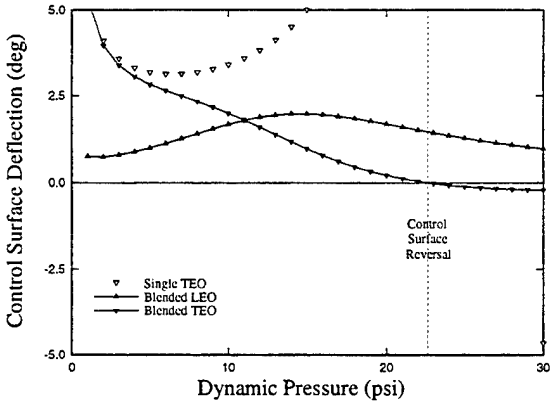

Figure 79: Trim for 90 deg/sec Roll Rate, Category II Optimized (Single Surface) Configuration, Mach 1.2

The optimized configuration for the multiple control surfaces' constraint did not change from the initial Category I (9g load) configuration. The wing weight remained 139.7 lbs. The wing reversal dynamic pressure and flutter velocities are reported in Table 14.

Deflections of the aircraft control surfaces are illustrated for Mach 0.9 in Figure 80. At low dynamic pressures, the combined magnitude of blended leading and trailing edge outboard surface deflections appear larger than the single trailing edge outboard deflections. The leading edge outboard surface is utilized to its maximum limit, 5^{o}, at 14 psi in order to effect roll trim throughout the dynamic pressure envelope.

A comparison of the results for the optimization with single and multiple control surface deflection constraints shows an 8.5% difference in weight, which is a potential structural weight savings of 12.4 lbs. The generic fighter aircraft wing can be more flexible and weigh less utilizing multiple control surfaces rather than only the single surface to achieve required roll performance.

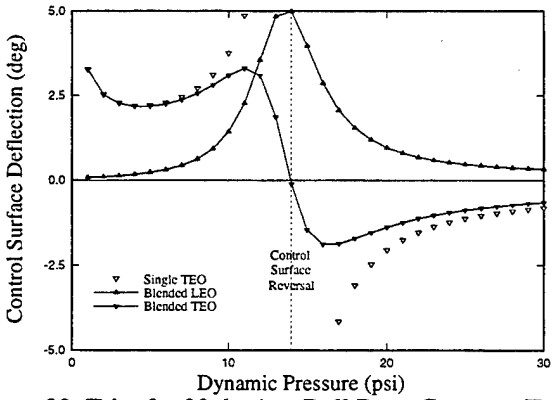

Figure 80: Trim for 90 deg/sec Roll Rate, Category II Optimized (Multiple Surfaces) Configuration, Mach 0.9

The generic fighter aircraft wing still maintains all of the strength requirements.

Category III Studies

In order to further explore the utility of AAW technology, the generic fighter aircraft wing with initial element sizes form Category I (6g load) was optimized for minimum weight with a flutter constraint, control surface deflection constraints (the same as Category II), and the stress constraints for the 6g aerodynamic load. The flutter constraint is set at 16,500 in/sec. The flutter velocity of this initial configuration is 15,073 in/sec, which indicates that the flutter constraint will be active, at least initially, during the optimization.

The optimized configuration with the single trailing edge outboard control surface constraint weighs 120.8 lbs. The final design variables show an increase in the thicknesses of the skin, spar webs, and rib webs, particularly along the mid and aft portions of the wing tip. There is a decrease in the area of the mid spar caps, whereas there is an increase in the area of the aft spar caps in the final design.

The resulting configuration was then analyzed for static and dynamic aeroelastic quantities. The wing reversal dynamic pressure was found for Mach 0.9 to be 27.2 psi and for Mach 1.2 to be 22.4 psi. The flutter velocities were determined to be 23,472 in/sec at Mach 0.9 and 30,364 in/sec at Mach 1.2. These static and dynamic aeroelastic results are similar to those of the nominal configuration. The single control surface deflection constraint was active in the design optimization resulting in a wing with greater chordwise stiffness. The flutter constraint was not active in the final design.

Deflections of the aircraft control surfaces are illustrated for Mach 1.2 in figure 81. The trends are similar to those exhibited by the Category II configuration as shown in figure 79. The configurations from Category II and III optimization with single surface constraints have similar chordwise stiffness.

The optimized configuration with the blended leading and trailing edge outboard control surfaces' constraints weighs 97.5 lbs. The design variables only changed slightly with several decreasing in value, and others increasing in value. No significant trends were apparent from the final values, but the flutter constraint was active in the final design.

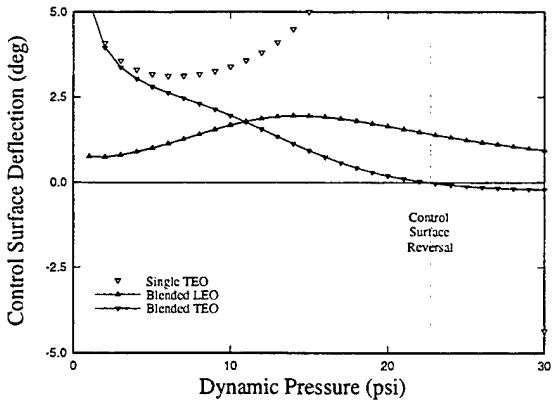

Figure 81: Trim for 90 deg/sec Roll Rate, Category III Optimized (Single Surface) Configuration, Mach 1.2

The resulting configuration was then analyzed for static and dynamic aeroelastic quantities. The wing reversal dynamic pressure was found for Mach 0.9 to be 12.7 psi and for Mach 1.2 to be 10.5 psi. The flutter velocities were determined to be 16,500 in/sec at Mach 0.9 and 19,788 in/sec at Mach 1.2. These static and dynamic aeroelastic results are slightly higher than the Category I configuration, as reported in Table 14.

Deflections of the aircraft control surfaces are illustrated for Mach 0.9 in Figure 82 The trends are similar to the to those exhibited by the Category II configuration as shown in figure 80. At low dynamic pressures, the combined magnitude of blended leading and trailing edge outboard control surfaces appear larger than the single trailing edge outboard deflections. The leading edge outboard control surface is utilized to its maximum limit, 5^{o}, at 12 psi in order to effect roll trim throughout the dynamic pressure envelope.

A comparison of the results for the optimization with single and multiple control surface deflection constraints shows a 21.3% difference in weight, which is a potential structural weight savings of 23.3 lbs. The generic fighter aircraft wing's chordwise flexibility was determined by the flutter constraint for the multiple surface optimization rather than the control surface deflection constraints, as with the single surface optimization.

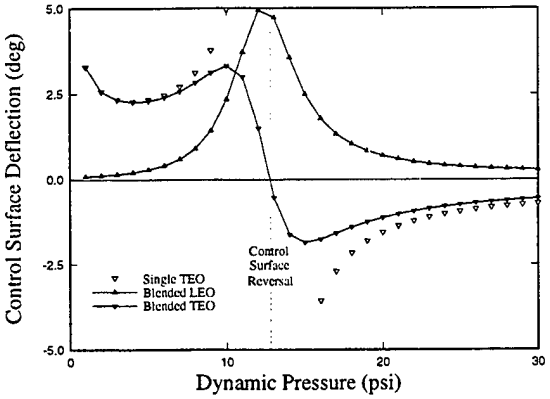

Figure 82: Trim for 90 deg/sec Roll Rate, Category III Optimized (Multiple Surfaces) Configuration, Mach 0.9

.Comparisons of Final Configurations

Table 15 compares the final configurations of each Category optimization by showing the constraints which are met (marked with a ✓) and the weight. The stress constraint is met in all but the nominal configuration. The single surface constraint ($\delta \leq 5^{o}$ at 15 psi) is only met by the nominal, and the Category II and III configurations optimized for this constraint. The multiple surface trim constraint ($\delta \leq 5^{o}$ for 10-20 psi) is met in all the optimized configurations. The flutter constraint ($V_f \geq 16{,}500$ in/sec) is met by almost all of the configurations. Because roll trim could be effected with either a single surface or multiple surfaces, it is apparent that AAW technology produces lighter weight structures which meet all of the critical constraints.

Table 15: Comparison of Constraints for Nominal and Final Wing Configurations

Configuration	Constraints Met in Final Analysis				Weight (lbs)
(Constraints in the Design)	Stress	Roll Trim		Flutter	
		Single δ	Multiple δ's		
Nominal		✔	✔	✔	164.0
Category I (9g)	✔		✔	✔	139.7
Category I (6g)	✔		✔		96.1
Category II (9g, sng. surf).	✔	✔	✔	✔	152.1
Category II (9g, mlt. surfs.)	✔		✔	✔	139.7
Category III (6g, sng surf., flutter)	✔	✔	✔	✔	120.8
Category III (6g, mlt surfs., flutter)	✔		✔	✔	97.5

SECTION IX

CONCLUSIONS AND RECOMMENDATIONS

The F/A-18 aircraft was selected as a demonstration for the development of preliminary design methods incorporating Active Aeroelastic Wing technology. The F/A-18 has been selected as the appropriate aircraft for an in-flight demonstration of Active Aeroelastic Wing technology so it is natural to develop design methods with the aircraft. Active Aeroelastic Wing technology represents a departure from the traditional design philosophy of avoiding flexibility and its detrimental effects through increased wing stiffness to the proposed philosophy of using flexibility with multiple control surfaces with no increase of stiffness to achieve specified roll performance.

An investigation of Active Aeroelastic Wing technology was initially conducted on the so called "beam-rod" model which is used by the aircraft industry for conducting flutter studies on production aircraft. The beam-rod model was incorporated herein for a consideration of a demonstration of acceptable roll performance through AAW technology for the F/A-18 aircraft. The beam-rod model was verified by comparing the natural mode shapes and frequencies to the results obtained by McDonnell-Douglas during a ground vibration test and are described in Section IV of this report. Further verification of the beam-rod model and selected aerodynamic representation of the F/A-18 is described in Section V flutter studies. The beam-rod model was further developed for Active Aeroelastic Wing technology through a study of control surface blending for the roll performance enhancement of the F/A-18 with a reduction of wing stiffening as described in Section VI. It is demonstrated that the roll performance of the F/A-18 could have been enhanced had AAW concepts been incorporated in the design stage of the aircraft is development.

At this point of the investigation, the use of the beam-rod model to provide preliminary design methods incorporating Active Aeroelastic Wing technology was somewhat limited. While the beam-rod allows one to accurately predict flutter speeds, the accurate prediction of aileron reversal is questionable especially if the wing under consideration is a composite wing such as the F/A-18. Further, the beam-rod model does not lend itself to design sensitivities with structural variations. It was determined that a finite-element representation of the built-up wing of the F/A-18 was necessary for the accurate prediction of aeroelastic deformation. After some unsuccessful initial attempts McDonnell-Douglas was contracted to provide an accurate finite-element model and the natural modes and frequencies are shown in Section VII.

Prior to obtaining the final finite-element representation of the built-up F/A-18 from McDonnell-Douglas a generic built-up fighter wing was considered to demonstrate preliminary design methods incorporating active aeroelastic wing technology. Optimization studies of a generic fighter aircraft wing were conducted utilizing multiple blended control surfaces to effect roll trim in Section VIII. The results of Section VIII demonstrate that Active Aeroelastic Wing technology is a viable design methodology when compared to the traditional design methodology of increasing stiffness to avoid problems associated with aeroelastic deformation. The incorporation of AAW technology in the preliminary design stage produces substantial structural weight savings and improvement of performance in the design of the wing.

It is recommended that the finite-element model of the F/A-18 developed by McDonnell-Douglas be verified as a model capable of accurately predicting aeroelastic deformations. This verified model of the F/A-18 wing should be used as numerical design tool for comparison of aeroelastic deformation obtained during the in-flight demonstration of AAW technology of the F/A-18. This finite-element should yield an accurate prediction of aeroelastic stability and performance parameters over the entire Mach number and dynamic pressure regimes.

Finally, it is recommended that a study be conducted using "smart materials" to deform flexible wings in the best manner to enhance the roll performance of an aileron over the entire operational dynamic pressure range. Further in the future it may be demonstrated that it is possible to roll a high performance aircraft without the use of external aerodynamic control surfaces with smart materials. This would represent a return to the Wright Brothers original concept of providing roll control by "warping" or twisting the wing properly.

REFERENCES

1. Miller, G. D., "Active Flexible Wing (AFW) Technology," Air Force Wright Aeronautical Laboratories TR-87-3096, February 1988.

2. Pendleton E., Lee, M., and Wasserman, L., "Application of AFW Technology to the Agile Falcon," Journal of Aircraft, Vol 29, No 3, May-June 1992.

3. Perry, B., Cole, S., and Miller, G., "A Summary of an AFW Program," Journal of Aircraft, Vol 32, No 1, January-February 1995.

4. Pendleton, E., Griffin, K., Kehoe, M., and Perry, B., "A Flight Research Program for Active Aeroelastic Wing Technology," AIAA Paper 96-1574-CP, 37th AIAA Structures, Structural Dynamics and Materials Conference, Salt Lake City UT, April 1996.

5. Miller, G. D., "An Active Flexible Wing Multi-Disciplinary Design Optimization Method," AIAA Paper No 94-4412-CP, 5th AIAA Symposium on Multidisciplinary Analysis and Optimization, Panama City FL, September 1994.

6. Johnson, E., and Venkayya, V., "Automated Structural Optimization System (ASTROS)," Vol I, Theoretical Manual, Air Force Wright Aeronautical Laboratories TR-88-3028, December 1988.

7. Rodden, W. P., Editor, "MSC/NASTRAN Handbook for Aeroelastic Analysis," The MacNeal-Schwendler Corporation, Los Angeles CA, 1987.

8. Yurkovich, R. N., "Flutter of Wings with Leading Edge Control Surfaces," 27th AIAA Structures, Structural Dynamics and Materials Conference, San Antonio TX, May 1986.

9. Grimes, P. J., "F/A-18 Airframe Compliance and Ground Vibration Data Report," McDonnell Aircraft Company, MDC A5773 Addendum B, January 1982.

10. Ansman, J. D., "Adaptive Multi-Dimensional Integrated Control (AMICS) - ASTROS Add-on Documentation," Interim Report for Wright Laboratories Contract F33615-93-C-3615, November 1995.

11. Andersen, G., Forster, E., Kolonay, R., and Eastep, F., "A Study of Control Surface Blending for Active Aeroelastic Wing Technology," AIAA Paper 96-1443, AIAA 37th Structures, Structural Dynamics and Materials Conference, Salt Lake City UT, April 1996.

12. Reichenbach, E., "F/A-18 Wing Finite Element Model for AAW Program," McDonnell-Douglas Memorandum AST-EYR-96-003, 20 May 1996.

13. Forster, E., Kolonay, R., Venkayya, V., and Eastep, F., "Optimization of a Generic Fighter Wing Incorporating Active Aeroelastic Wing Technology," AIAA Paper 96-4010, AIAA 6th Symposium on MDO, Bellevue WA, September 1996.